Investigation of ZnO nanorods as chemical and biological sensors

Ying Tu

Supervisors: Dr. Steffi Krause

Dr. Joe Briscoe

Submitted in a partial fulfilment of requirements of the Degree of Doctor of Philosophy

School of Engineering and Materials Science

Queen Mary University of London

September 2018

Declaration

I, Ying Tu, confirm that the research included within this thesis is my own work or that where it has been carried out in collaboration with, or supported by others, that this is duly acknowledged below and my contribution indicated. Previously published material is also acknowledged below.

I attest that I have exercised reasonable care to ensure that the work is original, and does not to the best of my knowledge break any UK law, infringe any third party's copyright or other Intellectual Property Right, or contain any confidential material.

I accept that the College has the right to use plagiarism detection software to check the electronic version of the thesis.

I confirm that this thesis has not been previously submitted for the award of a degree by this or any other university.

Signature: Ying Tu

Date: 06/09/2018

Abstract

Zinc oxide (ZnO) is a metal-oxide semiconductor with a direct wide band gap and high exciton binding energy at room temperature. It has been applied to many applications such as solar cells, light emitting diodes, nano-generators and chemical sensors. In this thesis, a solution phase synthesis method has been used to produce ZnO nanorods on conductive substrates at low cost. By controlling the growth conditions, ZnO nanorods with an aspect ratio of 51 in a single step was achieved. The morphology, crystallisation, optical properties, band structures and carrier lifetime were analysed.

Chemical sensors such as gas sensors play a very important role in our life and in industry. ZnO nanorods have been investigated as a sensing material to detect harmful gases such as NO_2 and NH_3. However, such a traditional sensing platform only works at high operating temperatures, which limits its application to portable devices or wireless devices. In order to decrease the working temperature, a Schottky diode was assembled by evaporating a gold layer on the top of the ZnO nanorods. Gas sensing results showed that this diode had good responses to NH_3 gas at room temperature. It also displayed high selectivity to NH_3 over acetone, CO_2, CO and ethanol. Long-term tests demonstrated good stability over 7-weeks.

ZnO nanorods are also a suitable sensing material for light-addressable potentiometric sensors (LAPS) that are designed to detect pH, redox ions and characterise cells and tissue. In contrast to the traditional electrolyte-insulator-semiconductor (EIS) structures, ZnO nanorods without an insulator were applied in LAPS and showed a spatial resolution of 3 μm. LAPS based on ZnO nanorods were used as a disposable

biosensor for the detection of α-chymotrypsin. The effect of the ZnO morphology on the spatial resolution was also investigated.

Publications and Presentations

Journal papers

- **Ying Tu**, Norlaily, Ahmad**,** Joe Briscoe, De-wen Zhang and Steffi Krause, Light-Addressable Potentiometric Sensors using ZnO Nanorods as the Sensor substrate for Bioanalytical Applications, *Anal. Chem.*, **2018**, 90, 8708-8715.
- **Ying Tu**, Shuqun Chen, Xuan Li, Jelena Gorbaciova, William P. Gillin, Steffi Krause and Joe Briscoe, Control of oxygen vacancies in ZnO nanorods by annealing and their influence on ZnO/PEDOT:PSS diode behaviour, *J. Mater. Chem. C*, **2018**, 6, 1815-1821.
- **Ying Tu**, Joe Briscoe, Steve Dunn and Steffi Krause, ZnO/Au Schottky diode working as an ammonia gas sensor at room temperature, in preparation.

Conference proceedings

- **Ying Tu**, Jianwei Li, De-Wen Zhang, Joe Briscoe and Steffi Krause, The effect of semiconductor morphology on the spatial resolution of ZnO based light-addressable potentiometric sensors, *proceedings*, **2018**, 2, 917.

Oral Presentations

- The effect of semiconductor morphology on the spatial resolution of ZnO based light-addressable potentiometric sensors. *Eurosensor 2018*, Graz, September 2018.
- Investigation of chemical sensors based on ZnO nanorods, Russell Binions memorial symposium, London, April 2018.
- ZnO nanorod synthesis and their application in chemical and biological sensors,

MRI-QMUL Spring symposium, London, May 2017.

Poster Presentations

- ZnO nanorod synthesis and their application in chemical and biological sensors, *Materials Research Society Fall Meeting and Exhibit*, Boston, November 2017.
- A ZnO-nanorod/PEDOT:PSS p-n heterojunction diode gas sensor working at room temperature without illumination or vibration, *MMA Air Quality Monitoring-Evolving Issues and New Technologies*, London, December 2016.

Acknowledgements

I would like to thank all those who have helped me during my PhD.

I worked with five great supervisors in the last four years. Jeremy Kilburn, Steve Dunn, and Russell Binions were my previous supervisors who gave me a firm start and developed my laboratory skills. My current mentors Steffi Krause and Joe Briscoe who helped me to fulfil this thesis and taught me how to be a good researcher. I would have quit my PhD if Steffi had not accepted me. I feel truly lucky and forever grateful to be her student. De-Wen Zhang who has provided me many great suggestions to develop this thesis. He was my last great hope when I met him in the first meeting after I joined Krause's group. My sincere thanks to my previous and current group members Xuan Li, Pelin Yilmaz, Yaqiong Wang, Hui Luo, Anirban Das, Martin John Gibbs, Norlaily Ahmad, Bo Zhou, Muchun Zhong, especially Jianwei Li, who helped to produce CVD ZnO, for their companionship and discussions, to Jun Ma, Chris Mole Ben Milson and Armando Lacerda for their technical support.

I would like to give sincere gratitude to my family, especially to my parents and sister. They could always find a proper way to encourage me and support me. They helped me to build confidence to continue my study when I was frustrated and depressed by supervisors' leaving. They told me I can achieve more than others in the most difficult situation. I also thank Yifei Pei, who accompanied me and shared my sorrow and joy.

Finally, I thank the China Scholarship Council and Queen Mary University of London for the financial support.

Table of contents

List of abbreviation

AACVD	Aerosol assisted chemical vapour deposition
CBM	Conduction band minimum
CL	Cathode luminescence
CPE	Constant phase element
CuSCN	Copper(I) thiocyanate
CVD	Chemical vapour deposition
CVD-ZnO	ZnO film produced by CVD method
d	Thickness of semiconductor layer
DCP	Drop-coating deposition
DTS	Deep-level transient spectroscopies
EIS	Electrolyte-insulator-semiconductor
EPR	Electron paramagnetic resonance
fcc	Face-centred-cubic
FTO	Fluorine-doped tin oxide
FWHM	Full width at half-maximum
HMT	Hexamethylenetramine
ICCD	International centre for diffraction data
IDEs	Interdigitated electrodes
ITO	Indium-doped tin oxide
I-V	Current-voltage
JCPDS	International Centre for Diffraction Data
L	Diffusion length of the minority carriers
LAPS	Light addressable potentiometric sensors
LSV	Linear sweep voltammetry
MOS	Metal oxide semiconductor
PANI	Polyaniline
PAS	Positron annihilation spectroscopies
PBS	Phosphate-buffered saline
PEDOT:PSS	Poly(3,4-ethylenedioxythiophene) polystyrene sulfonate
PIDs	Photo-ionisation detectors

PL	Photoluminescence
PLD	Pulsed-laser deposition
PMMA	Poly(methyl methacrylate)
PSS	Polystyrene sulfonate
PTFE	Polytetrafluoroethylene
QCM	Quartz crystal microbalance
SAED	Selected area electron diffraction
SEM	Scanning electron microscope
SOS	Silicon-on-sapphire
SPD	Spin coating deposition
SPIM	Scanning photo-induced impedance microscopy
SPR	Surface plasmon resonance
SPS	Solution-phase synthesis
TCO	Transparent conducting oxide
TEM	Transmission electron microscopy
UV	Ultraviolet
UV-Vis	Ultraviolet-visible
VBM	Valance band maximum

List of tables

List of figures

1 Introduction

1.1 Background and motivation

Technologies are created or upgraded for purposes to make human life safer, healthier and more comfortable. Sensing technology is important for a variety of human activities in personal safety and homeland security such as air quality monitoring, harmful gas detection, as well as disease diagnosis. The earliest chemical sensor demonstrations may be likened to nineteenth and early twentieth century miners who were certainly grateful for their "hand held" air quality monitor, a canary. Once the canary stopped singing and fell off their perch, the miners would immediately evacuate the mine as this was an indication of a leakage of poisonous gases such as methane or carbon monoxide, either of which could cause a fatal condition for miners. Although when looking back to that age, people could not exactly measure what type of the gas was and how much it was in mine, chemical sensors, the canary, did a great favour to protect miners' lives.

Nowadays, the chemical sensors are highly developed and can be defined as a transducer with a chemically responsive layer, which converts forms of energy such as electrical, optical or mechanical into a measurable signal. A chemically responsive layer is the key element of a chemical sensor which is what makes chemical sensors unique from physical sensors. The chemically responsive layer is well-designed to preferentially interact with target chemicals of interest. The interactions cause a change in the transducer's property, which produces a change in the sensor signal to be recorded.

ZnO is a semiconductor that can be used as a chemically responsive layer to interact with chemicals including volatile organic compounds [1], reducing or oxidising gases [2], [3], as well as some ionic species [4], [5]. In the traditional gas sensing technology driven by metal oxide semiconductors as responsive layers such as ZnO, the device needs to be heated to a certain temperature [6]. This limits the chemical sensors to work as a portable "canary" due to the large power consumption. Hence, to decrease the operating temperature and minimize the size of devices is essential.

Light-addressable potentiometric sensors (LAPS) are an electrochemical imaging technique based on photocurrent measurements at electrolyte-insulator-semiconductor field-effect capacitors [7]–[9]. LAPS are an emerging method to image living cells or investigate metabolic and signalling events in living cells. ZnO with a direct band gap of about 3.3 eV [10], [11], is a promising responsive layer for LAPS to provide information such as surface potential, ion concentrations and electrical impedance, which will be investigated in this thesis.

1.2 Zinc oxide (ZnO)

1.2.1 Background and properties

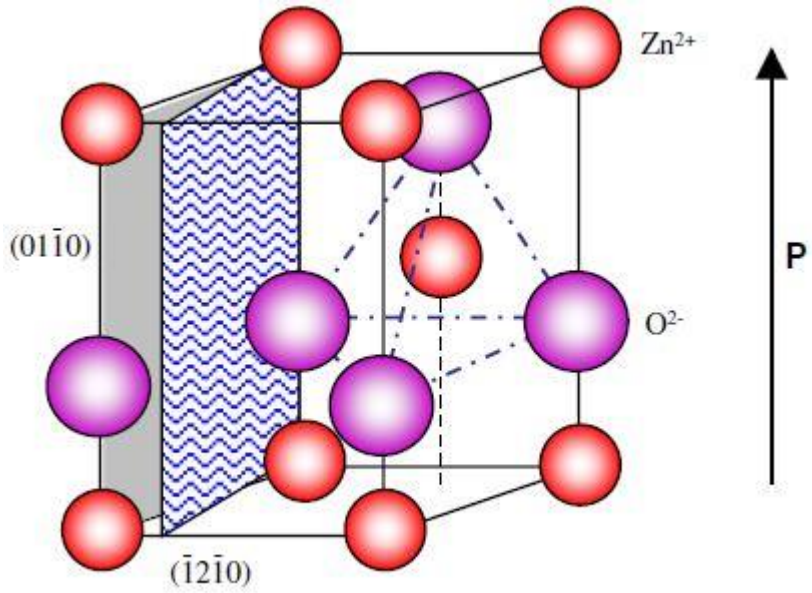

Figure 1.1 The wurtzite structure model of ZnO. The tetrahedral coordination of Zn-O is shown, adapted from reference [12]**.**

ZnO is a metal-oxide semiconductor with a direct wide band gap and high exciton binding energy at room temperature. It commonly adopts a wurtzite structure of a hexagonal crystal system with lattice parameters a = 0.3296 and c = 0.5207 nm [12]. ZnO is an intrinsic n-type semiconductor due to native defects. As shown in Figure 1.1, along the *c*-axis of the structure, ZnO can be simply treated as a number of alternating planes stacked with a tetrahedral coordination of four oxygen atoms to one zinc atom; the bonding between atoms is considered as ionic. The asymmetric structure caused by the tetrahedral coordination in ZnO makes it suitable for piezoelectric applications. The oppositely charged Zn^{2+} and O^{2-} on different planes also results in a dipole moment and spontaneous polarization in ZnO along the *c*-axis.

Due to the n-type semiconducting behaviour, radiation hardness, photoconductivity, piezoelectric properties and chemical stability, ZnO is considered as a promising material to be applied in piezoelectric energy harvesting system [13]–[17], photodetectors [18]–[22], light-emitting diodes [23]–[28], and photovoltaics [29]–[35]. The relatively abundance of zinc, ease of synthesis methods, and inexpensive processes make ZnO a promising semiconductor to be commercialised.

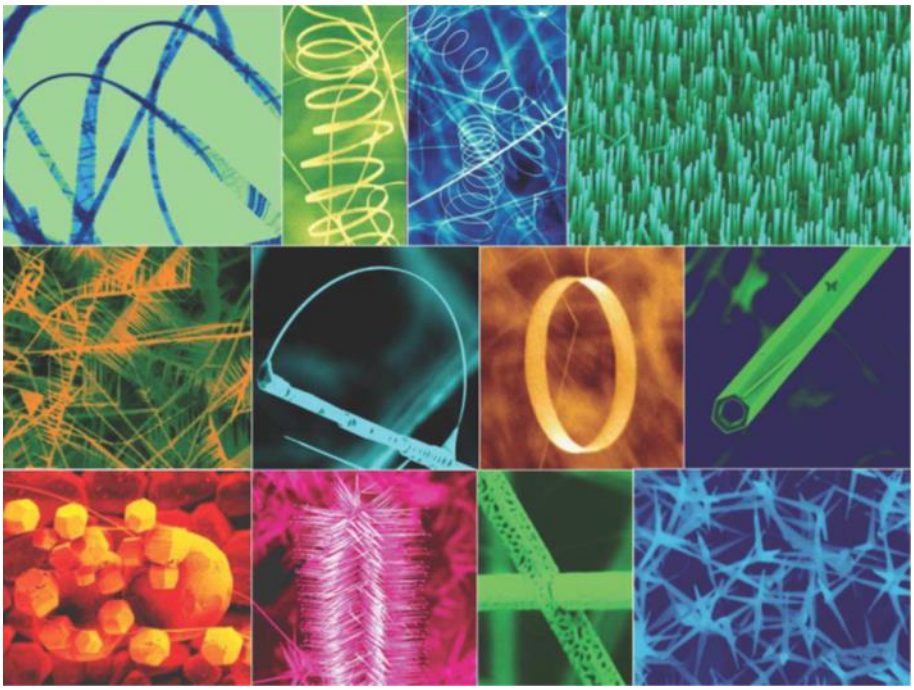

Figure 1.2 A summary of various ZnO nanostructures including nanohelixes, nanobows, nanopropellers, nanowires, nanotubes and nanocages under controlled synthesis conditions, adapted from reference [11]**.**

Nanostructured ZnO can be achieved via various processing methods. There is a great demand for ZnO with small dimensions due to its great advantages: 1) large surface-to-volume ratio, e.g. a dye-sensitised solar cell can improve its efficiency by an increased quantity of dye molecules [36]–[38]; 2) large number of active sites, e.g. a gas sensor can improve sensitivity as well as response time because of the increased number of interactions that occur on the surface [39]–[43]; 3) high specific surface

area, e.g. a nanogenerator can improve dipole moments due to the increased number of polar faces in ZnO [14]. Many examples of nanostructures have been studied and fabricated as devices: nanoparticles [44]–[47], nanorods [48], [49], nanowires [50]–[56], nanobelts [57]–[59], nanoplates [60]–[62], and nanotubes [63]–[65] being the most common (Figure 1.2). The versatile ZnO in novel morphology designs would lead to unconventional properties. An urchin-like ZnO has been found to be an improved sensor for harmful gas detection [66].

1.2.2 ZnO nanorod growth methods

The advantages of producing nanostructured ZnO in various applications were described in the previous section. Materials show some extraordinary properties when decreasing the size to nanometre level. Thus, with increasing demands coming from device design, a lot of effort has been devoted to the size control engineering on semiconductors to achieve either large surface-to-volume ratio or high surface area. Growth techniques that use some extreme conditions such as high temperature, vacuum or pressure could make ZnO highly crystalized with few defects in the lattice. However, such harsh environments limit commercialisation due to the poor scalability and complicated substrate pre-treatment. Many methods have been used to synthesize ZnO with desired nanostructures; they can be mainly classified as vapour-phase deposition and solution-phase synthesis. The next section summarizes the most common methods and focuses on the techniques that are most relevant to this thesis.

1.2.2.1 Vapour-phase deposition (VPD)

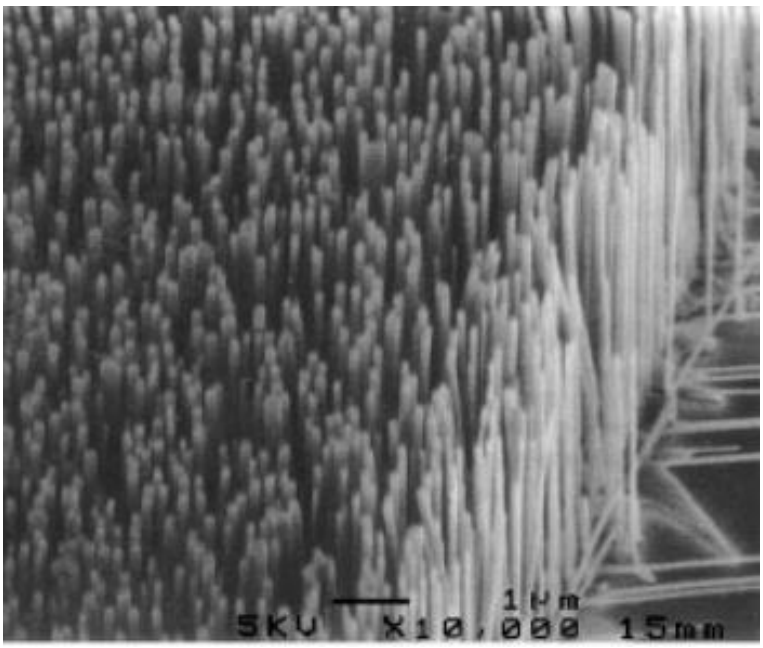

Figure 1.3 An array of ZnO nanowires grown on α-plane sapphire substrate by VLS-CVD method, adapted from reference [67]**.**

One of the most common methods for ZnO nanorod or wire growth is chemical vapour deposition (CVD) [68]–[70]. In principle, a thermal evaporation technique is a simple process in which chemical vapours are firstly generated by heating the solid materials at elevated temperatures. Generally, classified by the vapour-liquid-solid (VLS) or vapour-solid (VS) mechanisms, the resultant vapours phase condenses to form desired products under certain conditions such as a lower temperature, pressure or a special atmosphere [10]. A metal catalyst is pre-coated on the substrate for the growth of 1D nanostructures such as nanorods by VLS approach, Au in the case of ZnO growth [67], [71]–[73]. The gases choose the liquid Au droplet or a thin Au film as a preferential site for absorption and nucleation site for crystallization when supersaturated. During the growth, the catalyst droplet determines the growth directions as well as the size of the nanorods. Once the environment cools down below the eutectic temperature of the catalyst, the growth terminates as the reaction is no longer viable. As a result, size or

type of the catalyst droplet is one of the defining parameters that governs the formation of nanostructures with desired dimensions. Figure 1.3 shows a scanning electron microscope (SEM) image of uniform ZnO nanorods grown using Au catalyst on the α-plane of a sapphire substrate.

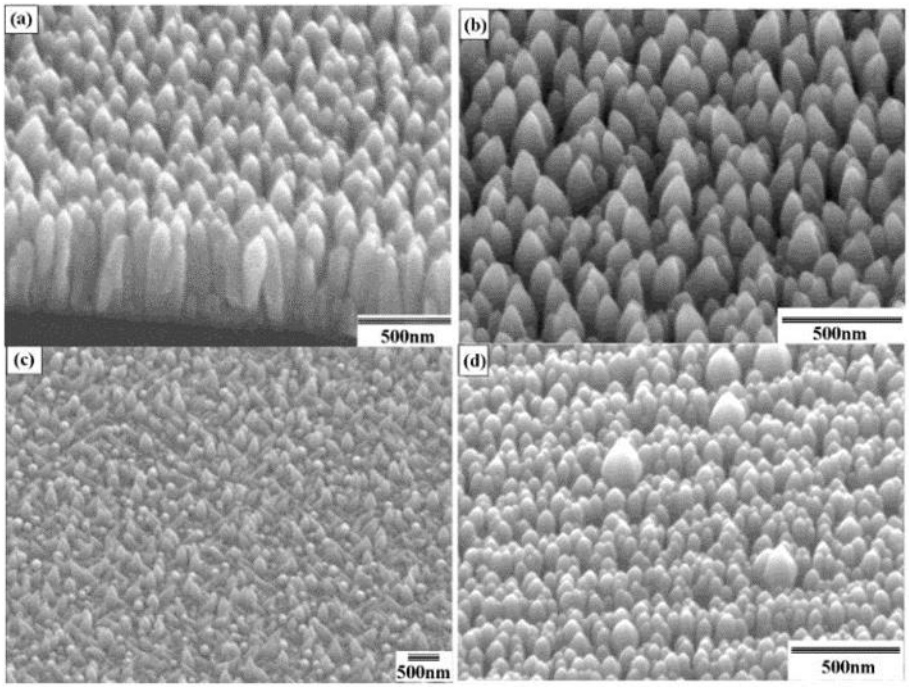

Figure 1.4 SEM images of ZnO nanorods grown on (a) fused silica, (b) Si (100), (c) sapphire (001), (d) sapphire (110), adapted from reference [70]**.**

Apart from the VLS process, a VS mechanism can also be used to produce nanorods on a substrate. Instead of using catalyst droplets to direct the ZnO growth by VLS, a VS process uses a substrate coated with a ZnO thin film prior to the heating programme [74]. Many methods for ZnO thin film deposition are available depending on the substrate such as pulsed-laser deposition (PLD) [75], [76], spin coating deposition (SPD) [77], drop-coating deposition (DCP) [78]. During the growth, the gaseous chemicals directly react to nucleate on the seeded ZnO, producing nanorods along the facets with lowest formation energy. Similar to the catalyst droplet, the ZnO seed layer plays a vital role in controlling the morphology. This technique has

advantages over VLS in device applications because no metal residues remain on the substrate. The gaseous zinc is often produced by carbothermic reduction of Zn^{2+} precursors [79]–[82]. It is then transported to the substrate where it reacts to form ZnO nanostructures. The oxygen source comes from a gas flow of either argon, dry air or nitrogen containing trace oxygen passing over the substrate [80]–[87]. An example [70] of ZnO nanorods grown by VS process on various substrates is shown in Figure 1.4. The substrate affects the morphology of ZnO produced by VS process in CVD methods.

1.2.2.2 Solution-phase synthesis (SPS)

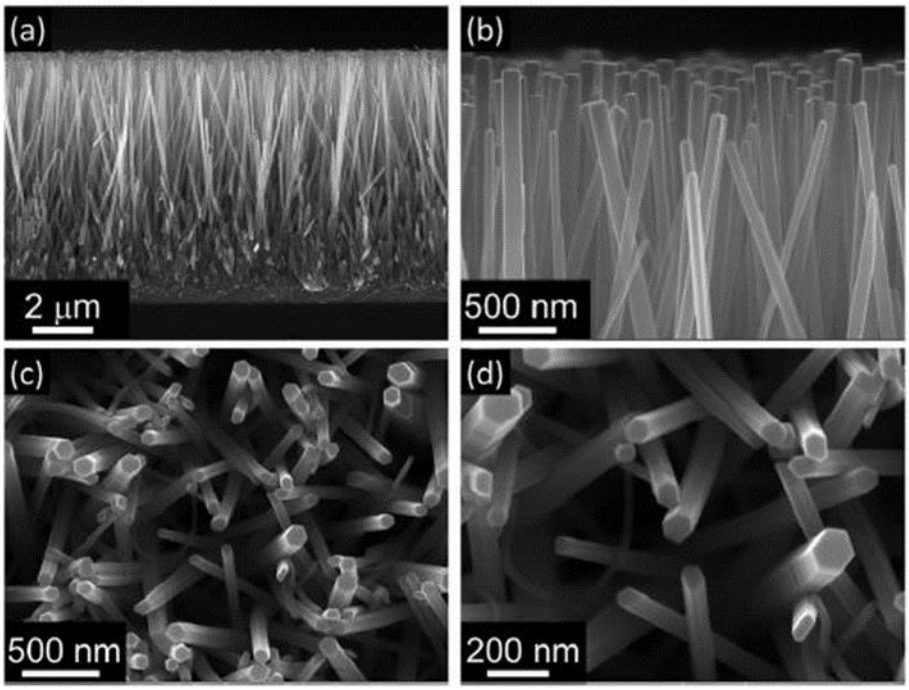

Figure 1.5 Cross-section (a and b) and top-view (c and d) SEM images of ZnO nanorods using SPS method. The nanorods were 8.6 μm in length and 79 nm in diameter (aspect ratio 108), adapted from reference [38]**.**

First, it is necessary to mention that the term, *hydrothermal growth*, is not appropriate for the contents introduced here. In *hydrothermal growth*, generally the aqueous precursors in a sealed vessel where reactions are treated both with pressure and

temperature above the solvent boiling point [88]–[90], whereas in the solution-phase synthesis, heat but no pressure is applied, the temperature is below the solvent boiling point, thus a sealed vessel is not necessary [18], [31], [38], [78]. In contrast to vapour deposition, SPS does not need high temperatures to vaporize the solid chemicals, instead the precursors react in a solution at relatively low temperature.

$$(CH_2)_6N_4 + 6H_2O \rightarrow 6HCHO + 4NH_3 \qquad \textbf{\textit{Equation 1.1}}$$

$$NH_3 + H_2O \leftrightarrows NH_4^+ + OH^- \qquad \textbf{\textit{Equation 1.2}}$$

$$Zn(OH)_4^{2-} \leftrightarrows ZnO + H_2O + 2OH^- \qquad \textbf{\textit{Equation 1.3}}$$

$$Zn(NH_3)_4^{2+} \leftrightarrows ZnO + H_2O + 4NH_3 \qquad \textbf{\textit{Equation 1.4}}$$

SPS of ZnO growth was first reported by Vergés in 1990 using zinc nitrate, zinc chloride and hexamethylenetramine (HMT) as precursors to obtain ZnO microcrystals [91]. The process was improved by Vayssieres [92] to achieve ZnO nanorods on different substrates including transparent conducting oxide (TCO) glass and Si. A seed layer is required to pre-deposit on the substrate prior to ZnO nanorod growth [18], [32], [38], [44], [66], [93], [94]. As described in the VS process, the seed layer for SPS has the same functionality to determine the size, density and orientation of the nanorods. Drop coating, spin coating, pulsed-laser deposition are the most common methods for the seed layer deposition [75]–[77]. During the growth by decomposition of zinc precursors using a ligand, two main steps occur: i) decomposition of a ligand; HMT is the most common case for ZnO synthesis; HMT decomposes into formaldehyde and ammonia which acts as a pH buffer (Equation 1.1 and Equation 1.2). ii) ZnO nanorods grow by reaction between hydroxyl ions with free Zn^{2+} (Equation 1.3) or alternatively a Zn-amine complex (Equation 1.4) on the base of a crystallised ZnO seed layer. Figure 1.5 is an example of ZnO nanorods synthesized by SPS [38]. In order to obtain long nanorods, the seeded substrate is placed face down into an

aqueous solution consisting of equimolar zinc nitrate and HMT [18], [31], [32], [38], [95]. The temperature for the growth is below the boiling point of water, generally between 60 and 90 °C. The growth period is between 0.5 and 24 h. In some cases, the method to achieve longer nanorods is replacing the precursor solution [15], [18], [32], [96], [97].

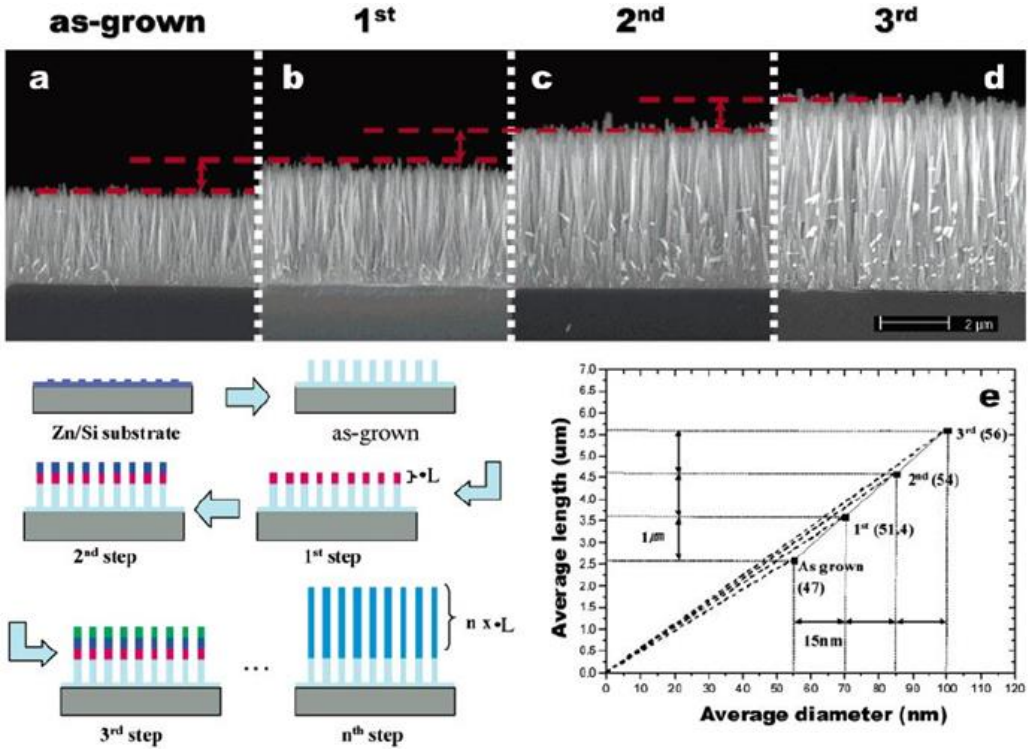

Figure 1.6 SEM images of multistep grown ZnO nanorods on Zn/Si substrate (a) as-grown, after (b) first step growth, (c) second step growth, and (d) third step growth. (e) average diameter vs length plot, adapted from reference [97]**.**

Some reports have demonstrated precursor concentrations, pH, temperature as well as duration have a strong influence on ZnO properties including morphology and dimension [97]–[100]. In this section, only precursor and duration are being considered. Tak *et al.* produced ZnO nanorods at pH 10.4 by SPS method on Si substrates (Figure 1.6) [97]. In this study, the single step growth temperature and duration were 90 °C and 6 h, and the pH was adjusted by adding NH_4OH. By applying multi-step growth, a ZnO nanorod array of 5.6 μm in length was obtained in three

steps. The precursor concentration in the initial step was 20 mM and decreased to 10 mM in the following steps.

Of the growth techniques reviewed above, both VPD and SPS have their own advantages. With VPD, ZnO has a high degree of crystallization with few defects while SPS can make ZnO with easily controlled morphology under moderate conditions with the potential to be industrialized. Both methods are well established and have been successfully applied in device applications such as solar cells [33], [50], [82], and gas sensors [1], [40], [101]. Methods are selected depending on the demands in structure and morphology.

1.2.3 ZnO native defects and impurities

ZnO produced using solution phase synthesis techniques without impurities or native defects remains a significant challenge. In the synthesis environment, impurities are difficult to exclude, and native defects are unavoidable due to their formation energies [10], [11]. The formation energies of native defects shown in Figure 1.7 are calculated in either oxygen-rich or zinc-rich conditions as a function of the Fermi-level position; the defects that are favoured under zinc-rich conditions all act as donors (p-type), while those that are favoured under oxygen-rich conditions all act as acceptors (n-type). The low formation energies of native defects such as oxygen vacancies and zinc vacancies in ZnO are ascribed to the incorporation of zinc and oxygen atoms. The native defects or impurities in ZnO are treated as potential factors contributing to the n- or p- type conductivity; on the other hand, they also play a role as recombination sites for induced charge carriers in some applications such as solar cells and photodetectors. Thus, there is a challenge to understand how each type of defect or impurity affects the physical, optical and electronic properties in ZnO. The most commonly reported native defects in ZnO are oxygen vacancies, oxygen interstitials,

zinc vacancies and zinc interstitials, in which the impurities are hydrogen and nitrogen [102]–[106]. Most calculations agree that oxygen vacancies and zinc vacancies are the lowest energy defects [102], [106]–[108]. Here we only focus on reviewing the most mentioned ZnO native defects - oxygen vacancies and zinc vacancies.

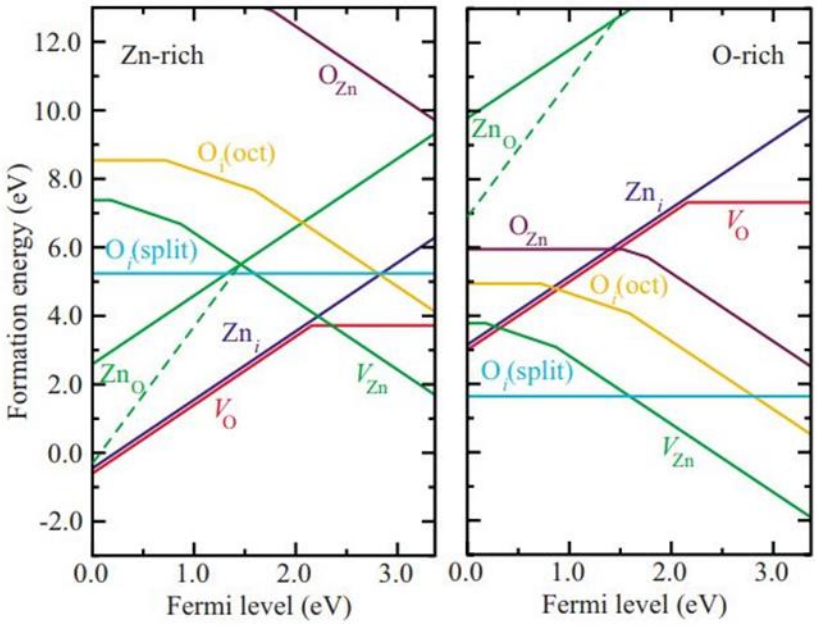

Figure 1.7 Formation energies of defects in ZnO calculated by Van de Walle et al. as a function of Fermi-level position. The zero on the Fermi-level scale corresponds to the valence band maximum. Only segments corresponding to the lowest energy states are shown, the slope of these segments indicates the charge state. Kinks in the curves indicate transitions between different charge states, adapted from reference [102]**.**

1.2.3.1 Oxygen vacancies

There has been a debate for decades about whether oxygen vacancies contribute to the n-type conductivity in ZnO [106]–[110]. For many years it was regarded that oxygen vacancies were the source of the intrinsic n-type characteristics of ZnO [109], [110]. Experimental techniques such as electron paramagnetic resonance (EPR) [111]–[113], deep-level transient spectroscopies (DTS) [114]–[116], cathode luminescence (CL)

[117]–[119] and positron annihilation spectroscopies (PAS) [105], [120], [121] were used to identify the defects in semiconductors. Alternatively, theoretical prediction such as first-principle calculations [122]–[124] using density-functional theory in local-density approximation [125]–[127] was also commonly used. Oxygen vacancies in Figure 1.7 have the lowest formation energy among defects that behave as donors. However, the density-functional calculations indicate that oxygen vacancies are very deep rather than shallow donors and, therefore, cannot be a source of n-type conductivity [102]. From Figure 1.7, the transition levels ε (2+/0) of ZnO is located at approximately 1 eV below the conduction band minimum (CBM), where the oxygen vacancies are stable in the neutral charge state in n-type ZnO, which means they are not the source of n-type conductivity of ZnO. Due to the 'negative U' shape, the transition levels ε (2+/+) and ε (+/0) are located in the conduction band. However, the oxygen vacancies can act as a relevant source of compensation in p-type ZnO with the assumption that oxygen vacancies are neutral charge states when the Fermi level is near CBM.

1.2.3.2 Zinc vacancies

Zinc vacancies are regarded as acceptors in ZnO [102], [107], [108]. As shown in Figure 1.7, the formation energy of zinc vacancies decreases with increasing Fermi level, which means it can more easily form in n-type samples. The zinc vacancies in ZnO derive from broken bonds of the four oxygen nearest neighbours, resulting in partially occupied states lying close to the valance band maximum (VBM). In p-type ZnO, zinc vacancies have high formation energies and therefore should exist in very low concentration, while in n-type ZnO, they have lower formation energies with related higher concentration, which act as compensating centres.

1.3 Metal oxide semiconductor (MOS) gas sensors

1.3.1 Principle of MOS gas sensors

There is a continually increasing need for detection and monitoring of a wide range of gases from diverse sources including toxic vapours, volatile organic compounds (VOC) and biological species for the protection of both human health and the natural environment. Gas sensing technologies are based on devices made up with sensing materials that interact with gas molecules to produce signals with magnitudes that are proportional to the concentration of target gases [128]. The essential properties for ideal gas sensors are sensitivity, selectivity, and responsivity. Durability, reliability, working temperature, power consumption are also considered in some cases [6]. There are various technologies currently available for gas detection such as electrochemical gas sensors, non-dispersive infrared gas sensors, photo-ionisation detectors (PIDs), metal oxide semiconductor gas sensors [129]–[135]. This section will focus on reviewing MOS gas sensors with tailored nanostructures.

MOS gas sensors have attracted increasing attention due to their high sensitivity, good selectivity as well as fast response. MOS gas sensors typically comprise a wide band gap polycrystalline metal oxide material, in which In_2O_3 [3], [136]–[143], SnO_2 [144]–[155], WO_3 [156]–[164], TiO_2 [165]–[172] and ZnO [40]–[42], [61], [77], [173]–[176] are the most commonly used. Due to the advantage of high surface area, MOS gas sensors exhibit a reversible change in electrical conductivity when exposed to trace gases. The electrical properties of semiconductors have been widely investigated and utilised in gas sensing devices to monitor pollutants in the environment.

Generally, the conductivity of a semiconductor increases with increasing temperature due to thermal excitation. In intrinsic semiconductors, conduction takes place by

thermal excitation of electrons from valance band to conduction band to generate equal numbers of free holes and electrons. As described in section 1.2.3, it is difficult to make intrinsic semiconductors without native defects or impurities. The extrinsic semiconductors, for example n-type, have impurities of one more valence electron than the host element in the crystal lattice, which results in an increase of electron concentration in the bulk materials and the valence electrons are bound weakly to their donors. Theoretically, this donor state is easily thermally excited to be free electrons because it lies close to the CBM, therefore the majority carriers in n-type semiconductors are negative electrons. Conversely, if the impurities or native defects result in one less valance electron than the host, the acceptor states lie close above the VBM, the acceptor states become filled by electrons from the valance band upon thermal excitation. The holes left in the valance band become free carriers which results in p-type conductivity. The band theory is important to MOS gas sensor since the performance varies in different types of semiconductors. A schematic of semiconductor energy bands is shown in Figure 1.8.

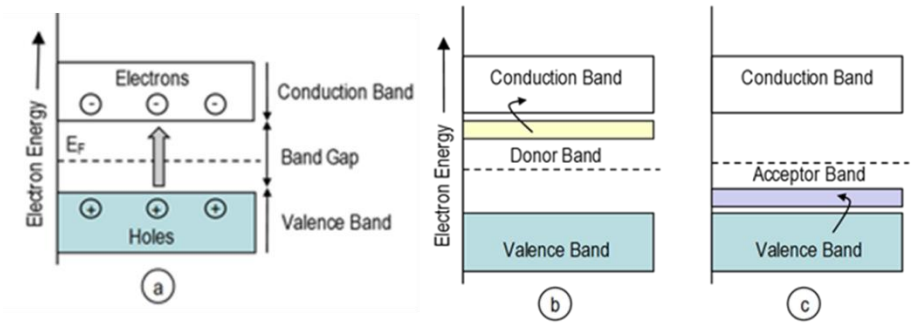

Figure 1.8 Schematic of semiconductor energy bands showing (a) the band structure for intrinsic, (b) n-type and (c) p-type semiconductor, adapted from reference [177]**.**

From the brief introduction of the band model above, it can be deduced that the charge carrier concentration is affected by changing the stoichiometry of a material on the

surface, since conduction is provided by the electrons or holes due to the defects or impurities on the surface. Thus, the capability to change the carrier concentration in semiconductors is the basis for their use in MOS gas sensing devices. The number of defects in the crystal lattice, the temperature and the energy levels of donors or acceptors have the potential to influence the concentration of charge carriers in a gaseous environment, therefore are factors to the performance of MOS gas sensors [2], [41], [178]–[184]. The gas-semiconductor interactions that generally take place on the surface of the material are quite complex involving chemical adsorption, reaction and desorption of gas species on the oxide surface.

Adsorption of gas species on the surface is the simplest form to modify the conductivity of the sensing materials by creating donor or acceptor surface states. The number of the surface states in a semiconductor depends on the partial pressure of the ambient gas. Therefore, the main contributors to the gas response of a semiconductor are the type, quantity, reactivity and mobility of the adsorbed oxygen in the ambient environment. Oxygen can be ionised to form different oxygen species (O_2^-, O^-, O^{2-}) by immobilising electrons from the bulk oxides at the gas-solid interface [172], [185]. For n-type bulk semiconductors, such as ZnO, SnO_2 and TiO_2, the oxygen in air withdraws electrons from ionised donors in the conduction band resulting in a depleted space charge layer near the surface [43], [154], [165]. The adsorption of oxygen on the surface reaches equilibrium and the increase in the width of the space charge layer is inhibited due to the saturation of oxygen ionisation at a certain oxygen partial pressure in ambient environment. Therefore, the resistance of the semiconductor approaches a stable value, which is treated as the baseline in air. The speed of the saturation process of oxygen ionization depends on the ambient temperature. When the target gases are introduced into the testing system, for example reducing gas

molecules, such as NH_3 or CO, the ionized oxygen species are active to react with the introduced gas molecules and reduced to release the trapped electrons. The released electrons go back to the conduction band resulting in increased charger carrier concentration as well as conductivity, therefore, the resistance decreases. Alternatively, if the target gases are oxidizing gas molecules, such as NO_2, the number of the free charge carriers in n-type semiconductors decreases and the width of the space charge layer increases since more electrons in the conduction band are withdrawn by the more electronegative oxidising gases than oxygen. This results in a further increase of the resistance. A schematic of the described mechanism is shown in Figure 1.9.

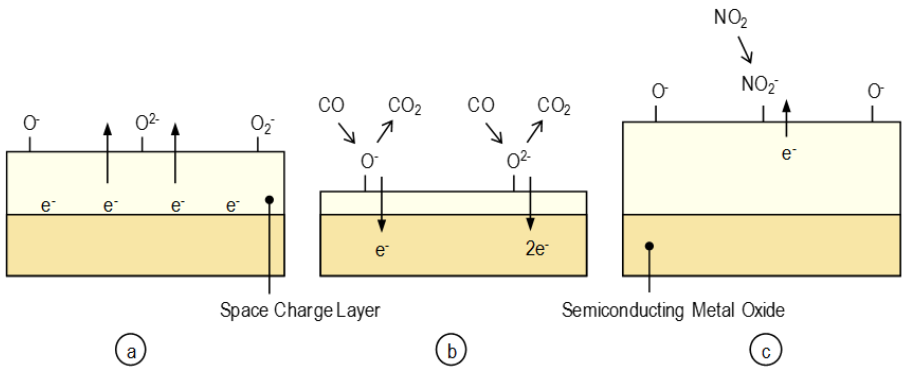

Figure 1.9 Schematic showing surface processes on an n-type semiconducting oxide sensing element (a) in air, (b) in reducing CO, (c) in oxidising NO_2, adapted from reference [186]**.**

In p-type semiconductors, such as NiO [187], [188], adsorbed oxygen creates acceptor states at the surface that can remove the electrons from the valence band resulting in 'positive hole' concentration at the interface. Hence, the introduction of a reducing gas results in decreased surface coverage of oxygen ions as well as a decrease of the charge carrier concentration and the resistance increases. Alternatively, if the analytes are oxidizing gases, the concentration of the charge carriers in p-type semiconductors increases and the resistance decreases. Figure 1.10 shows the resistance change via

time by exposing gas sensing materials to different gas environments. The characteristics shown below can be used to identify the performance of a gas sensor.

- ***Sensitivity*** – capability of a material to respond to a test gas by resistance change. A high sensitivity value is desired as the sensor can detect concentrations more accurately.
- ***Selectivity*** – capacity to discriminate test gas in the presence of interfering gases. A good sensing material should demonstrate selective response to the target gas in a mixed gas environment.
- ***Stability*** – ability to maintain its electrical properties especially sensitivity and selectivity to the target gas over long periods.
- ***Response and recovery times*** – response and recovery times are used to indicate how quickly the sensor responds to the target gas and returns to the baseline. Short response time is defined as the time required for the material resistance to change to a fixed percentage (normally 90%) of its baseline value. A short recovery time is required for continuous operation. The response time is usually shorter than the recovery time. A schematic of a typical gas sensor response curve is shown in Figure 1.10.
- ***Repeatability*** – ability to produce similar responses in successive tests under the same conditions.
- ***Reproducibility*** – ability to obtain similar responses from different sensor batches and on different gas sensing instruments.

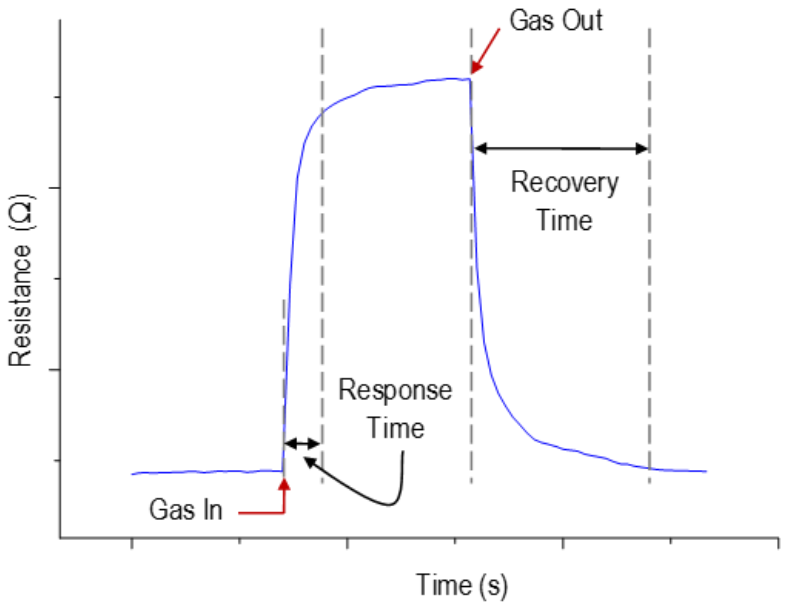

Figure 1.10 Schematic of typical gas response curve showing resistance against time.

1.3.2 Room temperature MOS gas sensor

Conventional MOS gas sensors usually have high working temperatures in a range of 150 - 400 °C [6], [178], [179], [183], [187], [188]. For high-temperature operation, the stability and life of devices decrease due to a thermally induced growth of metal oxide grains as well as the degradation of the surface activity. Furthermore, there is a risk of ignition when detecting flammable or explosive gases at high temperature, which limits their wide applications. Moreover, high power consumption is required by the high operating temperature, which also is a limitation to the next generation of battery-powered wireless sensors.

Currently, to develop high performance and reliable gas sensors working at room temperature is a major objective in the sensor research area. Some new sensor

technologies have been developed for the aim to decrease the operating temperature down to room temperature, for example optical sensors [189]–[191]. In this section, only resistive gas sensor based on metal oxide semiconductors will be reviewed.

1.3.2.1 Pure MOS

MOS with their structural merits, well-tailored size and prominent properties resulting from their nanoscale dimensions can be very good candidates for room temperature sensing layers. ZnO and Ga_2O_3 have been reported as metal oxide that are sensitive to nitrous oxide in the 1960s [192]; in the past decades the fundamental understanding and practical applications have been widely studied with great progress. Due to the development of nano-scale synthesis techniques, 1D semiconductor nanostructures such as nanowires/rods, nanofibers, and nanotubes can demonstrate appealing room temperature sensing performance [173], [174], [193], [194]. An array of polycrystalline SnO_2 nanowires has been reported to show high sensitivity and reversibility toward ethanol, CO and H_2 [151], [195], [196]. The highly sensitive performance was ascribed to the intrinsically small grain size and high surface to volume ratios of the SnO_2 nanowires. Furthermore, the porous networks of interconnected SnO_2 nanowires in the sensor film also contributed to the sensor performance by enabling the gas species to access all the surface of SnO_2 nanoparticles.

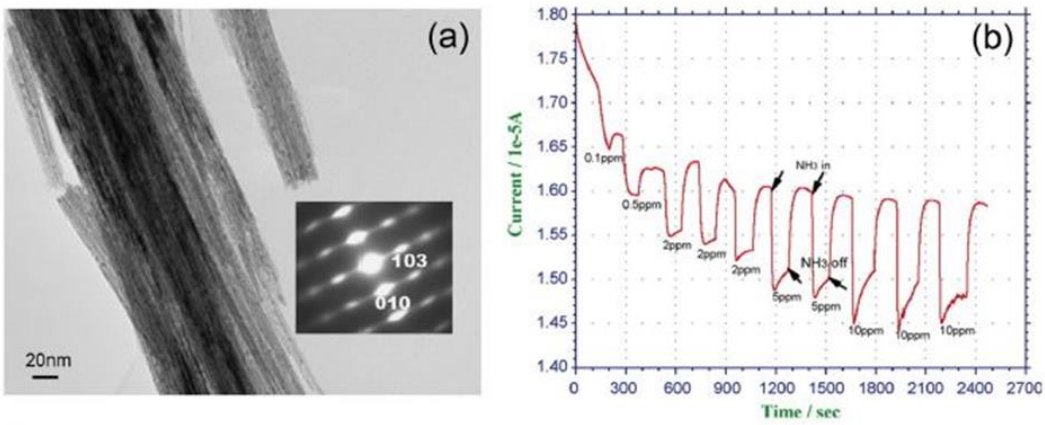

Figure 1.11 (a) TEM of ultrathin $W_{18}O_{49}$ nanowire bundle, inset is the ED patterns, (b) ammonia sensing performance of $W_{18}O_{49}$ nanowires at room temperature, adapted from reference [197]**.**

Non-stoichiometric tungsten oxide such as $W_{18}O_{49}$ (Figure 1.11) has been investigated by Zhao et al. to work as ammonia gas sensing materials at low temperatures [197]. The ultrathin $W_{18}O_{49}$ nanowire with 5 nm in diameter formed as bundles was demonstrated to have good sensitivity at sub-ppm level, compared to WO_3 nanowires which exhibited sensing performance to ammonia only at high temperatures [198]. By analysing the defects in $W_{18}O_{49}$, the high sensitivity to ammonia gas at room temperature was attributed to a large amount of oxygen vacancies. The high specific surface area and the ultrathin diameter due to the 1D nanostructure also contributed to the performance. In_2O_3 is another MOS which has been often reported as a gas sensor; by producing it with a specific method, it can act as a room temperature sensing material [176], [199]–[201]. Du et al. [202] have shown that polycrystalline In_2O_3 nanotubes made by layer-by-layer assembly on carbon nanotube templates in combination with subsequent calcination are capable to detect ammonia gas with good performance in sensitivity and reproducibility (Figure 1.12). By applying four kinds of In_2O_3 structures: regular tubes, broken tubes, nanoparticles and nanowires, it was found that the broken tubes had better responses to ammonia gas at room temperature

than the other three structures. They also explained that the high specific area and large number of active sites in the porous In_2O_3 broken nanotubes played a vital role in the sensing materials. Herein, by reviewing three kinds of MOS room temperature sensing materials, it is demonstrated that the strategy of producing nanostructured MOS in well-tailored size has the potential to decrease the operating temperature in gas sensing technology.

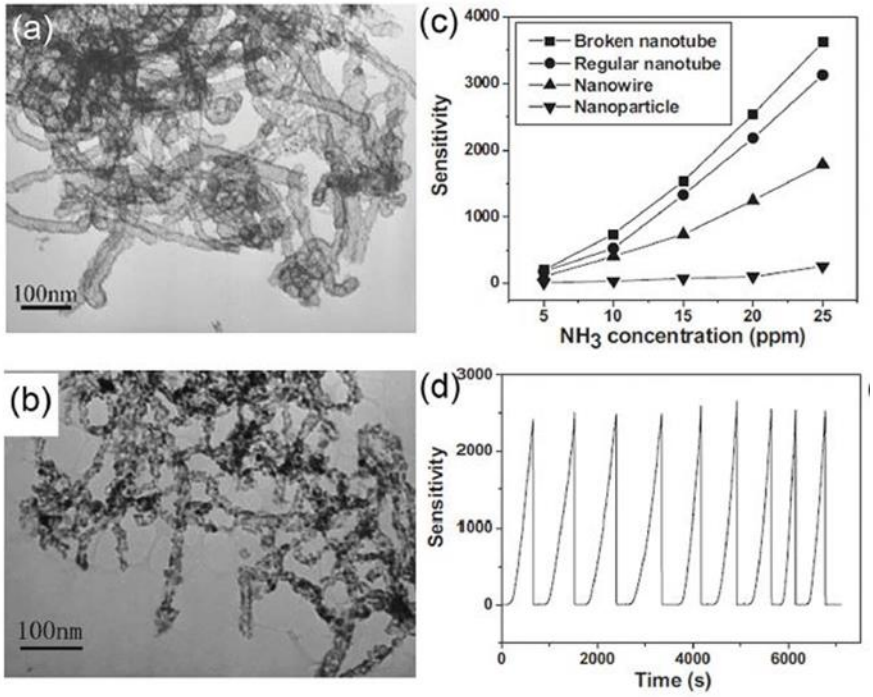

Figure 1.12 TEM images of In_2O_3 (a) regular nanotubes, (b) broken nanotubes, (c) Sensor sensitivity of various In_2O_3 nanostructures against ammonia concentrations (5 - 25 ppm) at room temperature, (d) repeatability of broken nanotubes against time for 20 ppm ammonia detection, adapted from reference [202]**.**

1.3.2.2 Heterojunctions

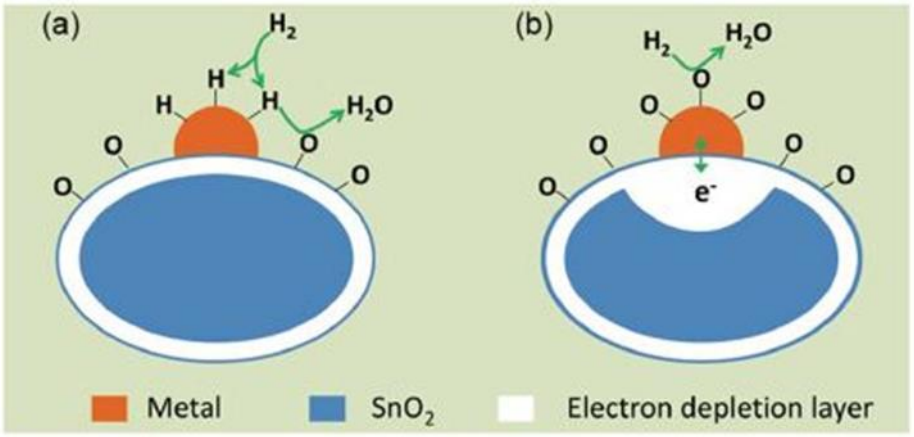

Figure 1.13 Schematic illustration of (a) chemical sensitisation and (b) electronic sensitisation on SnO_2 surface, adapted from reference [193]**.**

Apart from the pure MOS, heterojunctions between MOS and noble metals could be another option to decrease the operating temperature for a gas sensor. A typical method to produce the heterojunctions is the surface modification of the MOS with various noble metals such as Au [198], [203], [204], Ag [194], [205], [206], Pt [198], [207]–[209], and Pd [210]–[212]. It is appealing that room temperature gas sensing performance can be realized by surface functionalization or hybridization of semiconductors with metal dopants. The enhancement by noble metals in gas sensing can be classified as "chemical sensitisation" or "electronic sensitisation", depending on changes in the work function of MOS when in contact with metals. The "chemical sensitisation" takes place as a spill-over effect; the noble metal increases the reaction rate of oxidation processes occurring at the interface rather than changing the resistance of the MOS as shown in Figure 1.13a. "Electronic sensitisation" in Figure 1.13b produces a direct electronic interaction at the interface between the noble metal and MOS. A depletion layer near the interface is produced by the stable metal oxides (e.g. AgO and PdO) in air. The electronic sensitisation will decrease when the oxide

formed of metal promotors is reduced to metal by reducing gases. By either effect from chemical or electronic sensitisation, the semiconductors can achieve an effective room temperature gas sensing performance.

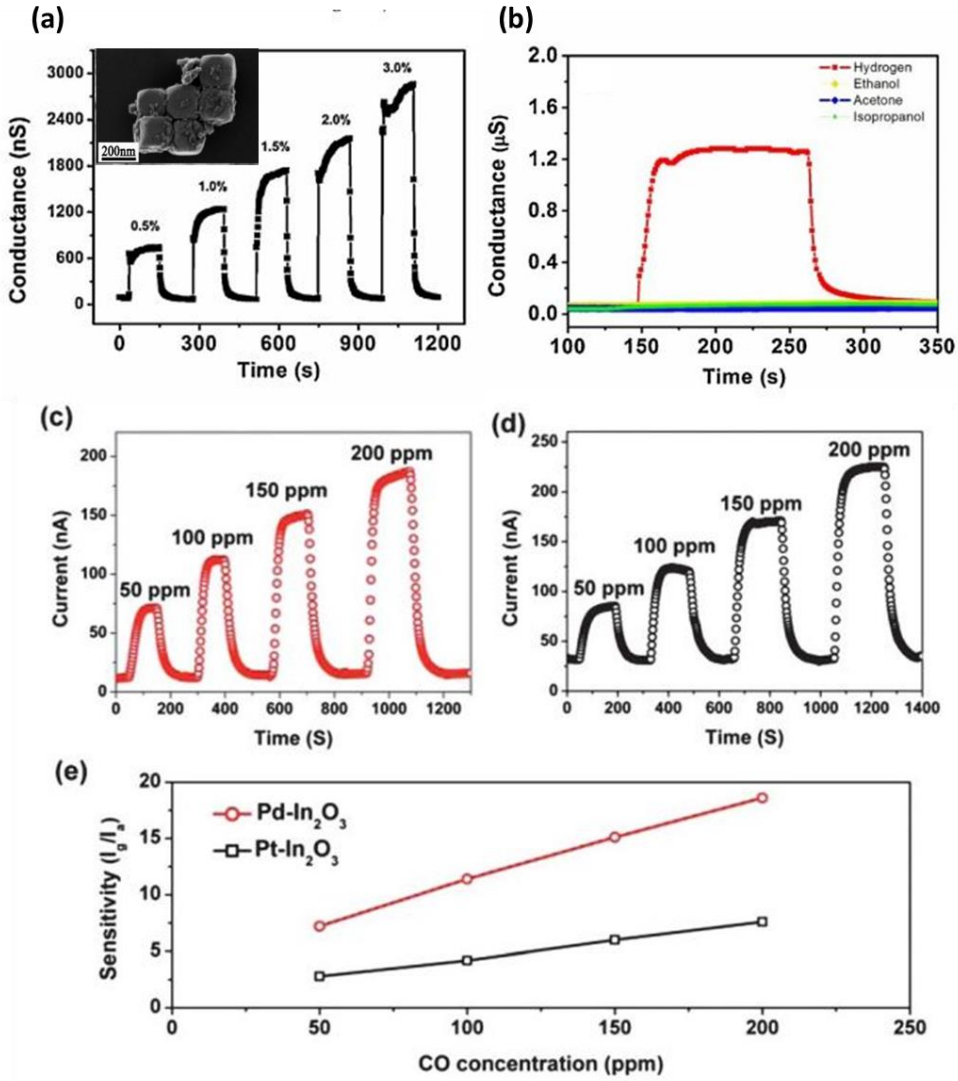

Figure 1.14 (a) Sensor response curve of Pt-decorated In_2O_3 nanocubes to various H_2 concentrations, inset is the SEM image of the In_2O_3 and (b) different gases with the same concentration of 1.5 vol%[213]***. Response curves of Pd-decorated (c) and Pt-decorated (d) In_2O_3 nanoflower to different CO concentrations, (e) corresponding sensitivity of (c) and (d) to CO, adapted from reference*** [214]**.**

Metal decorated In_2O_3 nanostructures such as nanocubes and "nanoflowers" have been demonstrated to be able to detect H_2 or CO of low concentration with high sensitivity

and selectivity at room temperature [213], [214]. The sensor based on Pt/In_2O_3 nanocubes displays a good response to different H_2 concentrations (Figure 1.14a) as well as good selectivity to H_2 (Figure 1.14b). Both Pd/ In_2O_3 (Figure 1.14c) and Pt/ In_2O_3 (Figure 1.14d) "nanoflowers" display high sensitivities to different CO concentrations at room temperature. However, Pd had better sensitisation effect than Pt in In_2O_3 showing in Figure 1.14e. In both cases the pristine In_2O_3 did not have response to gases at low temperatures, which reveals the crucial effects of metal particles in the room temperature gas sensing performance. Both the "chemical sensitisation" and "electronic sensitisation" were suggested to contribute to the behaviour.

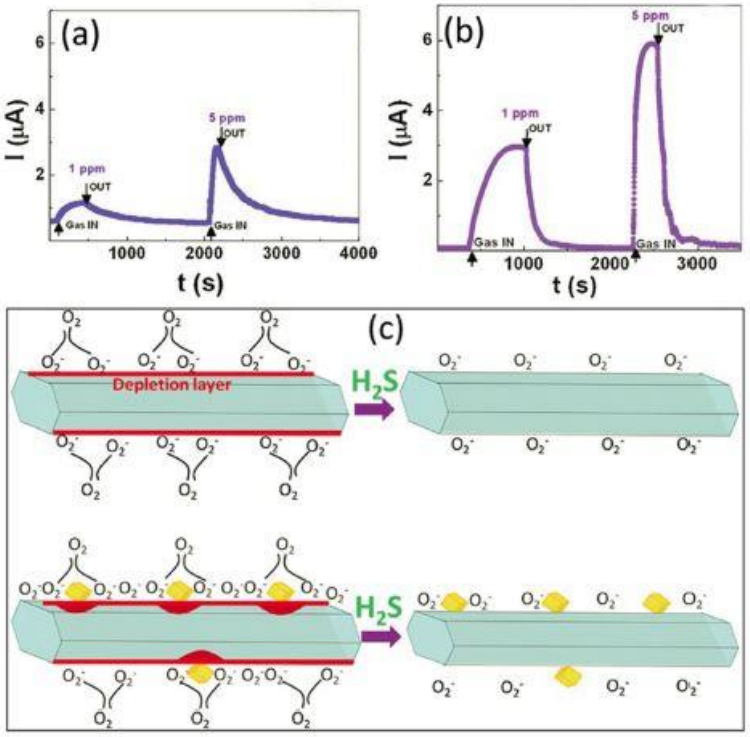

Figure 1.15 Response curves of (a) pure and (b) Au modified ZnO nanowires (Au at% = 1.2) towards 1 and 5 ppm H_2S at room temperature, (c) schematic of sensing mechanism to H_2S, adapted from reference [215]**.**

Ramgir et al. have reported a room temperature gas sensor based on ZnO nanorods modified with Au nanoparticles [215]. It displayed enhancements of not only the

sensitivity to H_2S, but also the response time. The Au/ZnO sensors exhibited a response (I_{gas}/I_{air}) of 38 and 79.4 toward 1 and 5 ppm of H_2S shown in Figure 1.15b, which are much higher than that of the pure ZnO under the same conditions (2 and 5 in Figure 1.15a, respectively). The recovery time of Au/ZnO to 5 ppm H_2S was 170 s, while it was 860 s for the pure ZnO. The great enhancement by Au modification in Au/ZnO was determined by two main factors, the schematic of the mechanism is shown in Figure 1.15c. One is the catalytic effect (chemical sensitisation) which facilitated the reaction rate between oxygen ion species and H_2S. The other one is the electronic sensitisation due to the formation of "nano-Schottky" type junction barriers at the ZnO-Au interface, which results in a higher work function of 5.39 eV as compared to that of pure ZnO nanowires (5.09 eV). The randomly distributed "nano-Schottky" junctions over ZnO nanowires lead to a higher room-temperature resistance than pure ZnO. This work also proves that the Au modification on ZnO nanowires can help to decrease the operating temperature in gas sensing.

1.4 Light addressable potentiometric sensors (LAPS)

Imaging technology is crucial to many disciplines and is generally classified as optical imaging, electronic imaging or a combination of both. A light addressable potentiometric sensor is a semiconductor-based chemical device with applications in the field of chemistry, materials science, biology and medicine. With LAPS, chemical images can be generated that visualize the concentration distribution above the sensor substrate. This light addressability can be used to detect chemical or biological analytes, such as pH, ions, redox pairs, organs, tissues, and enzymatic reactions by recording photocurrents generated locally in the semiconductor with a focused, intensity-modulated light source [8] [9].

1.4.1 Principle of LAPS

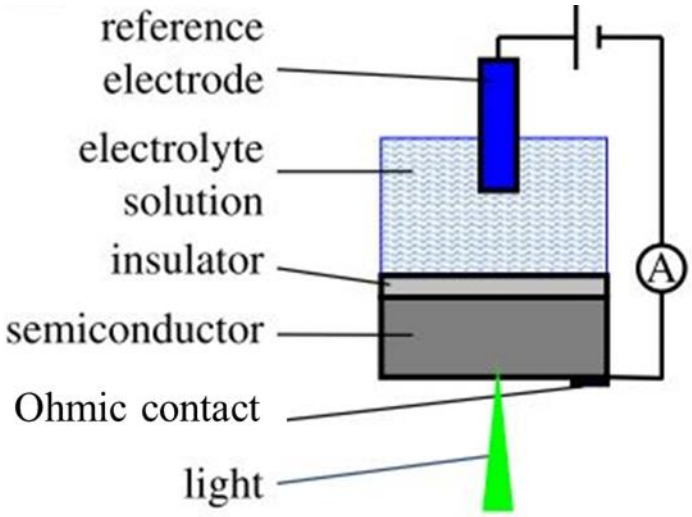

Figure 1.16 Basic set-up for LAPS measurements, adapted from reference [9]**.**

First proposed by Hafeman [216] in 1988, LAPS belong to the family of field-effect sensors that use an electrolyte-insulator-semiconductor (EIS) structure, in which the sensing surface of the insulator is in contact with the solution to be analysed [7], [8],

[8], [217]–[224]. A basic LAPS measurement setup is schematically shown in Figure 1.16.

The chemical imaging sensor system consists of a modulated light source, optics to deliver a light beam on the sensor plate, an electrochemical setup with a 3D scanning mechanism, measuring electronics. The modulated light source usually is a diode laser with periodic pulses in a frequency range from 1 to 100 kHz, the wavelength of it is selected according to the band gap of the semiconductor layer. Illuminating the back or the front side of the substrate are both possible in LAPS measurements. Frontside illumination has advantages over backside illumination in terms of directly generating photocarriers in the space charge layer. However, the uniform light delivery may be disturbed by the specimen placed on the sensing surface due to scattering and absorption. Some biological specimen such as living cells, organs might lose activity by the focused light, therefore, a backside illumination is more common to see.

By applying a constant voltage between reference electrode and the semiconductor, a space charge layer, either a depletion layer or an accumulation layer, with capacitance C_{SC} is formed at the semiconductor-insulator interface. Pairs of electrons and holes are generated by the absorption of photons in the semiconductor layer when the light illuminates the backside of the substrate. Given the electric field formed inside the depletion layer, the electron/hole pairs are separated, although some of them recombine while crossing the defects or pinholes in the semiconductor layer. When the light is turned off, a transient current in the opposite direction is formed by recombination of the excess holes and electrons in the depletion layer. Since electron/hole pairs are only generated in the illuminated area, LAPS are light-addressable. By recording shifts of voltage from curve A to B at a constant

photocurrent in the photocurrent-voltage (*I-V*) curve (Figure 1.17a), LAPS can determine the concentration distribution of analytes that cause a change in the surface potential of the insulator or the sensing layer. Scanning photo-induced impedance microscopy (SPIM), first proposed by Krause et al. [225]–[227], is another imaging technique that records shifts of the maximum photocurrent from curve B to C in the *I-V* curve, where the maximum photocurrent is related to the local impedance of the illuminated area. Therefore, changes of the voltage (LAPS) or the maximum photocurrent (SPIM) in the *I-V* curve is an indication to determine any analytes of interests above the sensing layer (Figure 1.17a). Figure 1.17b shows an example of *I-V* curves of a LAPS with n-type Si for different pH values. The surface potential responds to pH according to the Nernst equation, resulting in a shift of the *I-V* curve along the voltage axis.

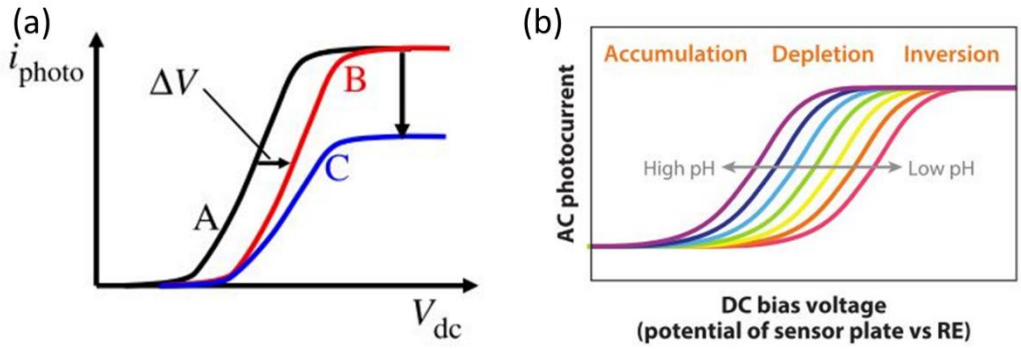

Figure 1.17 (a) I-V curves of LAPS and SPIM measurements. LAPS measure the shift of the potential from curve A to curve B, while SPIM measures the shift of maximum photocurrent from curve B to curve C; the maximum photocurrent is directly related to the local impedance of the illumination area of the sensor layer, adapted from reference [9]***. (b) a schematic of the pH response of LAPS with an n-type semiconductor, adapted from reference*** [8]**.**

Different semiconductor materials have been investigated in the EIS structure for LAPS including Si [228], GaN [218], NbO_x [229], and TiO_2 [230]. The EIS structure was regarded as the only structure for LAPS measurements until ITO was discovered

as a LAPS substrate without insulator [227]. A lateral resolution of about 2.3 µm was achieved by scanning the edge of a high impedance poly(methyl methacrylate) (PMMA) dot using indium tin oxide (ITO)-coated glass as the substrate with a 405 nm diode laser in LAPS measurements (Figure 1.18). The absence of an insulator layer in a LAPS platform has a number of advantages: (i) The sensitivity of the sensor surface for samples with charge and impedance is increased; (ii) The device is not only sensitive to potential and impedance changes but can also record redox processes; (iii) There is no limitation to the modification of the semiconductor surface by functionalization and (iv) the device assembly process is greatly simplified and low cost.

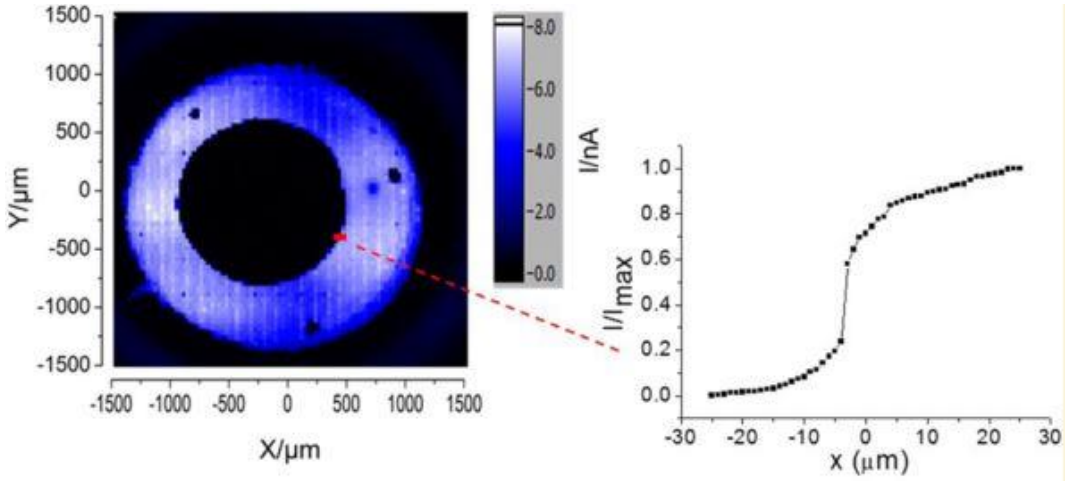

Figure 1.18 LAPS image of a PMMA dot on ITO surface without an insulator and x-axis photocurrent scan across the edge of the PMMA dot as indicated, adapted from reference [227]**.**

Photocurrent, measurement speed, and spatial resolution are the most important features for LAPS measurements, in which spatial resolution determines the smallest structure that can be observed and represents the quality of a photocurrent image [7]–[9]. The spatial resolution in LAPS can be defined as the diffusion length within the short lifetime of minority carriers [231]. The resolution can be calculated by different

methods depending on experimental techniques. For example, sometimes the smallest pattern that can be observed is referred as the resolution. Alternatively, by line scanning across the edge of a high impedance pattern with a focused light beam, the resolution is the distance required for the photocurrent to decrease from the maximum to 1/e of the difference between the maximum and minimum photocurrent. Resolution in LAPS can also be represented as the full width at half-maximum (FWHM) in first derivatives of a photocurrent line scan across the edge of a high impedance pattern [227].

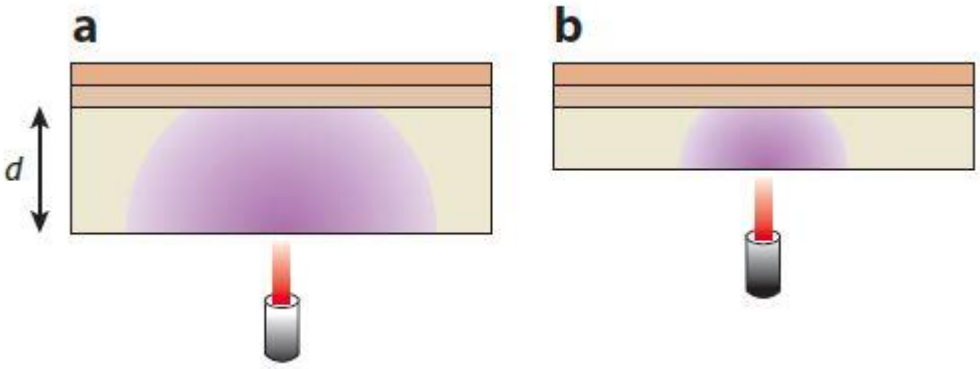

Figure 1.19 Schematic illustrations of (a) the diffusion of photocarriers from the illuminated point on the back side of a LAPS plate, (b) the effect of thinning the sensor plate, adapted from reference [8]**.**

In semiconductors, the carrier diffusion length and lifetime are two important properties. The diffusion length can be defined as the average length that a carrier is able to move between generation and recombination. The lifetime is the time that carrier can exist since it is generated. For heavily doped semiconductors, the majority carrier has short diffusion length and short lifetime due to the great recombination rates. The diffusion length (L) is related to the carrier lifetime (τ) and diffusion coefficient (D) according to the formula: $L = \sqrt{D\tau}$ [232][233].

It has been discovered that the spatial resolution is limited by two main factors (1) the quality of the light focus, which is the source to excite charge carriers in the semiconductor; (2) the lateral diffusion of minority charge carriers, i.e. holes in a n-type semiconductor and electrons in an p-type semiconductor, out of the illuminated area in the semiconductor substrates. For the most common case, when light illuminates a point on the back side of a substrate, the penetration depth of the light is much smaller than the thickness of the semiconductor layer. In the simplest mode, the spatial resolution is given by $\sqrt{L \times (L + 2d)}$, where L is the diffusion length of the minority carriers, d is the thickness of semiconductor layer [223]. When d is much smaller than L, the spatial resolution is given by L and the carrier diffusion is two-dimensional (Figure 1.19). Therefore, apart from using a high quality light source, one of the simplest strategies to improve the resolution for LAPS is either decreasing d or using a semiconductor layer, in which the minority diffusion length is small.

Nakao *et al.* reported that the spatial resolution of 300 μm was improved to 10μm by decreasing the thickness of silicon from 500 μm to 20 μm [234]. However, this method is limited to be widely applied in a silicon substrate as it is fragile and difficult to process. Ito solved this problem by replacing the fragile silicon with silicon-on-sapphire (SOS), in which the active layer was only 500 nm thick [235]. Krause *et al.* reported the best resolution for LAPS to date is 0.8 μm by using a silicon layer of 0.5 μm in thickness on SOS and a two-photon effect for photocurrent generation [225]. Therefore, thinning the semiconductor subtracts is effective as the theory predicts.

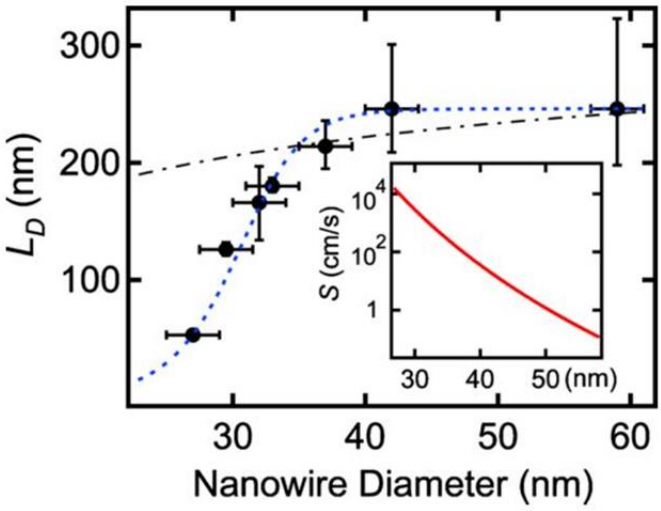

Figure 1.20 Measured diffusion length of minor carriers (L_D, solid circles) as a function of ZnO nanowire diameter. The dotted-dashed line represents the model with a constant S (=10^3 cm s^{-1}), adapted from reference [236]***; the dashed lines represents the model with a diameter-dependent S (solid line) shown in the inset plotted on a semilogarithmic scale.***

Given by $\sqrt{L \times (L + 2d)}$, to find a suitable semiconductor with a smaller diffusion length of minority carriers has also been useful to improve the resolution. The *L* in bulk silicon was 18 – 19 µm [237], the best values of lateral resolution reported for bulk silicon have been about 20 µm [234]. Amorphous silicon with a diffusion length of minority carriers of 120 nm was reported to have a resolution in a sub-micrometre range [238], [239]. The same material with different morphology has different *L*, and the small *L* shows better lateral resolution in LAPS. ZnO is an n-type semiconductor with small *L* and has not been used as substrate in LAPS measurements. In ZnO nanowires, a strong diameter dependence of the diffusion length could be observed for nanowire diameters below 40 nm; while the diffusion length approached a value of 250 nm when nanowire diameters were above 40 nm (Figure 1.20) [240]. Therefore, according to the theory, thin ZnO nanowires with small *L* would be a promising substrate for LAPS measurements.

1.4.2 Applications of LAPS

LAPS belong to the family of field-effect sensors. Many technologies that have been developed for ion-selective electrodes, ion-selective field-effect transistors, and EIS capacitive sensors are also adaptable to functionalization of a LAPS surface. In addition to the example of pH sensitivity in Figure 1.17, LAPS has been widely developed for the detection of ions including Li^+, Na^+ [241], K^+ [241]–[243] and alkaline metal ions such as Mg^{2+} [244], [245], Ca^{2+} [241], [242] and anions F^-, NO^{3-}, SO^{4-} [246]–[248].

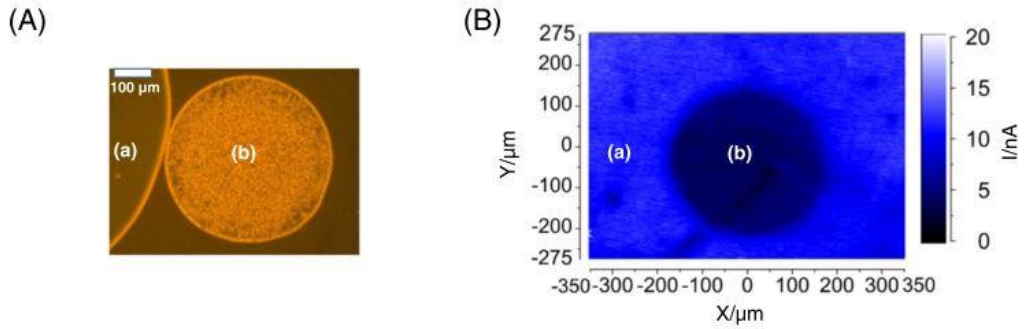

Figure 1.21 Yeast-agarose gel on a 1,8-nonadiyne modified silicon-on-sapphire (SOS) surface; (A) optical microscope image of (a) pure agarose gel and (b) yeast agarose gel, (B) LAPS photocurrent image with in same area as (A), adapted from reference [249]**.**

LAPS were initially designed for biochemical and biological sensing. Based on LAPS system, enzymes such as alcohol dehydrogenase [250], urease [251]–[255], penicillinase [255]–[261], glucose oxidase [255], and acetylcholinesterase [262], [263] have been immobilised on LAPS substrates. Some of them are based on the pH sensitivity of LAPS, which can detect the pH change during the enzyme reactions. For example, Seki et al. reported a pH-sensitive layer for the detection of urea, penicillin and glucose using enzymes which induce a pH change in the *I-V* characteristics of LAPS [255]. Alternatively, LAPS images can be used to directly observe the presence

of enzymes or living cells. Zhang et al. reported a clear LAPS photocurrent image of yeast Saccharomyces cerevisiae on a 1,8-nonadiyne modified SOS surface [249]. The contrast between the yeast and background (as shown in Figure 1.21) is ascribed to a decrease in the local photocurrent caused by the negative surface charges of the cells and an increase in the local impedance.

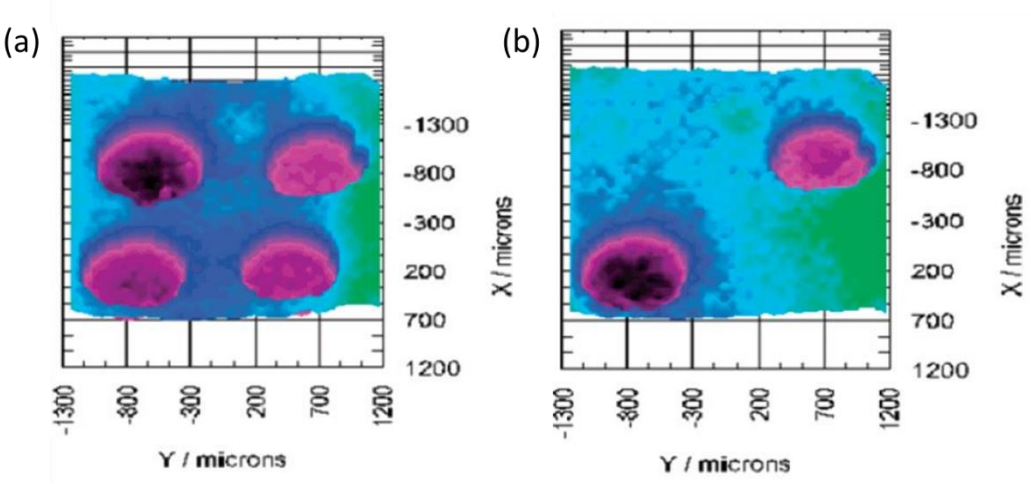

Figure 1.22 LAPS photocurrent images of an array of different polymer dots on n-i-p substrate (a) before and (b) 3 h after addition of α-chymotrypsin (1 μM) into pH 7.3 buffer solution. (Polymer dots on the bottom left and top right are cellulose acetate; on top left and bottom right are poly(ester amide), adapted from reference [219]**.**

SPIM with a Si:H n-i-p/insulator structures was reported to detect enzyme by visualizing the degradation of a film on the sensor chip [219]. An array consisting of two dots of poly(ester amide) and two dots of cellulose as shown in Figure 1.22 was deposited on the surface of SPIM chips; after addition of α-chymotrypsin, the poly(ester amide) dots are degraded gradually while cellulose dots are not affected.

Given the ability of detecting surface potential and measuring 2D photocurrent images, LAPS has great potential in monitoring cellular processes to improve our understanding of physiological events such as cell signalling, attachment and

development and to investigate the response of cells to surfaces and drugs at a microscopic level as this could aid the development of tissue regenerative materials and disease combating drug design.

2 ZnO nanorod synthesis and their application in PEDOT:PSS diodes

2.1 Introduction

ZnO, as described in section 1.2, is considered as a promising material to be assembled in functional structures such as p-n junctions [18], [174], [264]–[267]. ZnO obtained by solution-phase synthesis at low temperatures has many unintentional defects due to its low formation energy [10]. Thermal annealing is one of the most popular methods to remove impurities and structural defects from the crystal lattice [268]. However, depending on the annealing atmosphere, the defect level in the crystal varies after annealing [268].

The importance of understanding the defects originates from the desire to assemble devices with advantageous electrical, optical and magnetic properties. A p-n junction is a semiconductor structure, which allows current to flow only in one direction and is utilized as a fundamental element of most semiconductor devices including diodes, transistors, solar cells and integrated circuits. ZnO can become part of a p-n junction by incorporating it with both organic and inorganic p-type semiconductors [13], [18], [78], [95], [265]. The rectification ratio is represented as the ratio of the forward and reverse current at a specific voltage. The rectification ratio of ZnO nanorod-based diodes with inorganic p-type semiconductors, for example CuSCN, have values of 102-104, while it is less than 10 with organic p-type semiconductors [96], [266], [268]. The lower rectification ratio of ZnO diodes using organic p-type materials, such as PEDOT:PSS, has been ascribed to the large leakage current caused by recombination sites or trap states at the interface [268]. Methods to improve the rectification of these

diodes would widen their potential applications, taking advantage of the beneficial properties of the organic p-type semiconductors such as low cost, ease of synthesis/coating, flexibility etc. as well as improving the properties of devices that already use such structures [15], [265].

In this chapter, high aspect ratio ZnO nanorods are synthesized in a single step using an aqueous solution method by altering the synthesis time and precursor concentration. A p-n junction was assembled by spray-coating a poly(3,4-ethylenedioxythiophene) polystyrene sulfonate (PEDOT:PSS) film on the top of the ZnO nanorods. The rectifying behaviour of devices made with ZnO nanorods annealed in nitrogen and oxygen were investigated. The annealing atmosphere was found to affect oxygen vacancies and hence carrier concentration and rectifying behaviour of the p-n junction. This one-step synthesis of ZnO nanorods and control of the diode rectification via the ZnO annealing conditions therefore represents a simple method to produce nanorods with high aspect ratio and improve the performance of a p-n junction.

2.2 Experimental methods

2.2.1 Growth of ZnO nanorods

All the chemicals were purchased from Sigma-Aldrich and used without any further purification. ZnO nanorods were synthesized on FTO-coated glass (Solaronix SA Switzerland, 15 Ω/sq) and copper plates. The substrate was cleaned with acetone and then 2-propanol by ultra-sonication for 15 minutes. A seed layer of zinc acetate was coated on the substrate from a 0.005 M solution in ethanol. The solution was dropped on the substrate and dried with nitrogen, followed by annealing in air at 350 °C for 25 min. A thin crystallised ZnO seed layer was formed after annealing. The seeding

process was repeated three times. The substrate was suspended face-down in a jar with a solution consisting of equal concentrations of zinc nitrate and hexamethylenetetramine (HMT). Then the jar was placed in a pre-heated oven at 90 °C for a defined time. Afterward, the ZnO nanorods were annealed at 350 °C for 1 h under different atmospheres (nitrogen and oxygen). The gas flow rate was set to 1 L/min.

2.2.2 Device fabrication

The substrate was placed on a 100 °C hotplate, and 1 mL of PEDOT:PSS solution (1.3 wt % in water, conductive grade, Sigma-Aldrich) was deposited on top of the ZnO nanorods using an aerosol spray coating technique. Devices made with a ZnO/PEDOT:PSS p-n junction were completed by evaporating a 100 nm gold contact with an active area of 0.15 cm^2 (0.3 cm × 0.5 cm) on the PEDOT:PSS surface using a vacuum thermal evaporator (E306A, Edward). Regions around the active area were blocked to prevent short circuits using poly(methyl methacrylate) (PMMA, average M.W. 120000 g/mol), which was dissolved to form a 11 wt % solution in methoxybenzene (99%, Sigma-Aldrich).

2.2.3 Characterization and measurements

The surface and cross-section morphology of ZnO nanorods were examined using a scanning electron microscope (SEM, FEI Inspect F). The average and standard deviation of nanorod diameter and length were calculated by measuring 20 nanorods. The 20 nanorods were randomly selected using SEM images by using Image J. The aspect ratio of nanorod was calculated using the average length divided by the average diameter. The selected area electron diffraction (SAED) pattern was collected using a transmission electron microscopy (TEM, JEOL JEM 2010). Absorption spectra of ZnO were measured using a UV-Vis Spectrometer (Perkin Elmer, Lamda 950). X-ray

diffraction (XRD) patterns of ZnO on FTO coated glass were obtained with a Panalytical Xpert Pro diffractometer using Cu Kα radiation. High resolution X-ray photoelectron spectroscopy (XPS) was carried out using a Thermo Scientific K-Alpha^{+}. XPS data were analysed by CasaXPS^{TM} software with a calibrated C 1s peak of 284.6 eV. Mott-Schottky measurements were performed by a potentiostat (Gamry Potentiostat Interface 1000) with a three-electrode setup; a Ag/AgCl electrode and a glassy carbon rod electrode were used as reference and counter electrodes, respectively. 0.01 M Na_2SO_4 (pH 6.8) was used as the electrolyte. Voltage-current characteristics of the p-n junction were measured using a source meter (Keithley 2400) controlled by a custom-written LabVIEW program in the range of - 1.5 to + 1.5 V at room temperature. The average and standard deviation of rectification ratio in different annealing atmospheres was obtained from 3 devices.

2.3 ZnO nanorods growth

2.3.1 Effect of the substrate

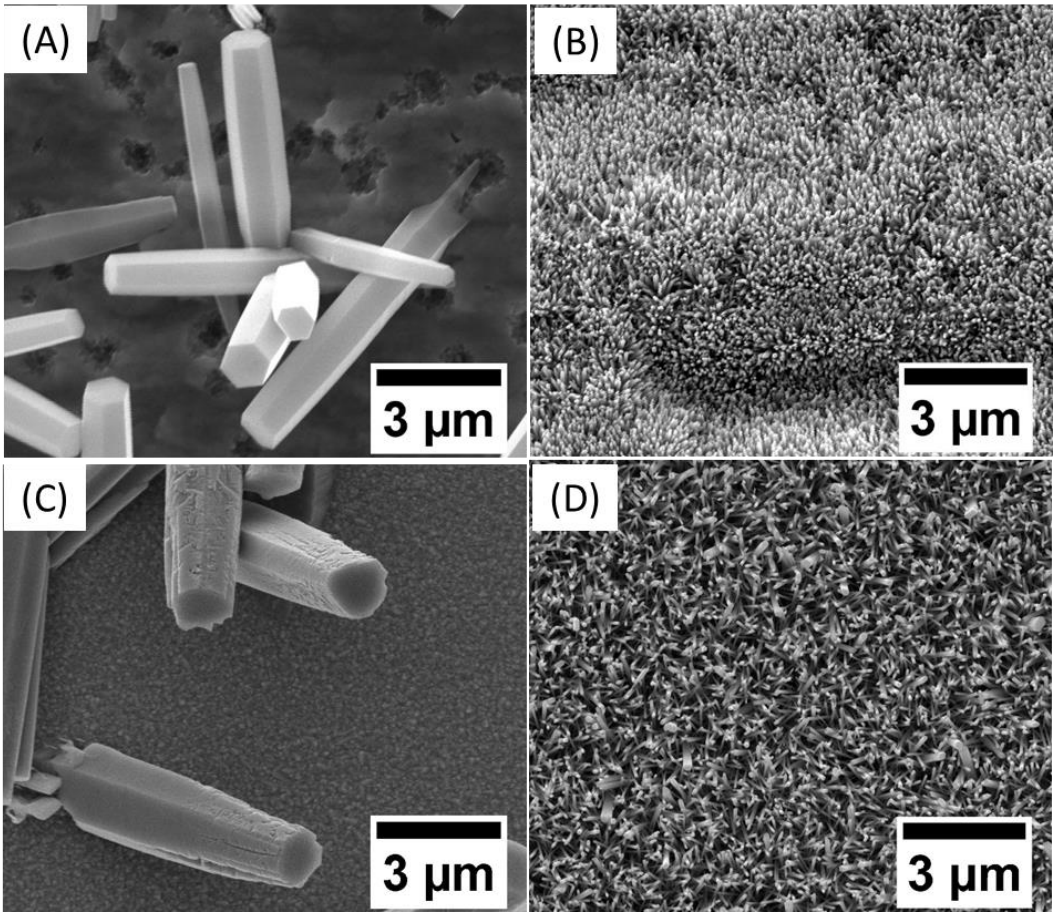

Figure 2.1 Morphologies of ZnO nanorods synthesized at pH 6 on different substrates with or without seed layer. (A) Cu plate without seed, (B) Cu plate with seed, (C) FTO coated glass without seed, (D) FTO coated glass with seed.

The effect of the substrate on ZnO growth was investigated by using different substrates with or without a seed layer. A seed layer of crystallised ZnO thin film was deposited on a copper or FTO coated glass by decomposing zinc acetate at 350 °C in air. ZnO nanorods were synthesized in a pH 6 solution for 24 h on those substrates. The SEM images in Figure 2.1(A) and (C) show that without a seed layer, ZnO grew as rods no matter what the substrate was, however, the disordered nanorods dispersed in random directions were hardly useful to a defined device construction. Moreover,

ZnO nanorods on bare substrates display large size both in diameter and length, resulting in a low aspect ratio. On the seeded substrates, a uniform and dense array of ZnO nanorods with preferred orientation could be observed showing in Figure 2.1(B) and (D). The crystallised seed layer greatly promoted the active growth, and this was ascribed to the nucleation activated facets of the ZnO seed layer supplied at the beginning of the growth. The crystallised ZnO seed layer on the substrate played a vital role because of the preferred (001) crystal face with low formation energy. Due to the flexible surface of the copper substrate, the ZnO nanorods in Figure 2.1(B) presents as a wave-shaped array from the top view. This structure would have disadvantages due to the uneven surface when a top layer has to be deposited. To obtain an array with uniform ZnO nanorods, an FTO coated glass substrate was selected.

2.3.2 Effect of pH

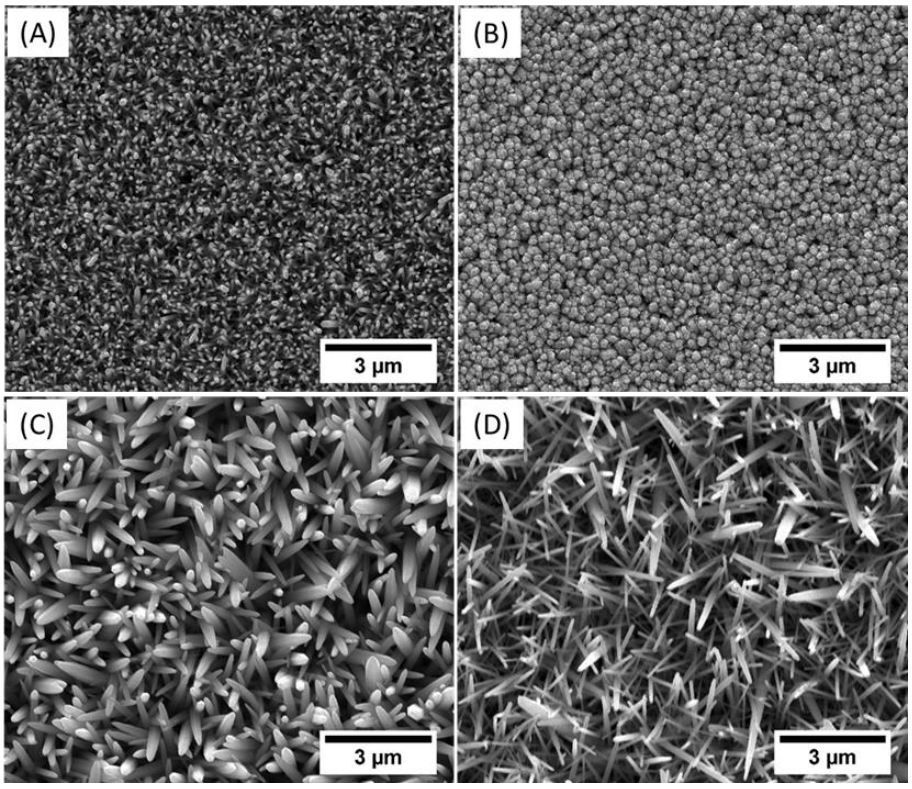

Figure 2.2 Top view SEM images of ZnO nanorods on FTO coated glass in different pH solutions. (A) pH 6, (B) pH 10, (C) pH 10.5, (D) pH 11.

According to the chemical reactions in section 1.2.2.2, an alkaline environment is essential to ZnO growth. HMT is not only a source of hydroxyl but also a pH buffer by slowly releasing OH^-. Theoretically, from Equation 1.3 the amount of reactant $Zn(OH)_2$ would increase with increasing pH in the solution. This is because the equilibrium would be disturbed when more OH^- is introduced and a new equilibrium establishes to produce more $Zn(OH)_2$. The original solution was measured to be pH 6. In order to achieve a high pH, a 0.2 M ammonia solution was dropped into the solution monitored by a pH meter. Solutions of pH 10, pH 10.5, and pH 11 were obtained. The top view SEM images of ZnO nanorods in Figure 2.2 illustrate that only in pH 6 solution, the nanorods displayed a hexagonal structure, while ZnO nanorod growth were inhibited at pH 10. At pH 10.5, the top of the rods was cone shaped rather than

hexagonal although ZnO displays as nanorods. At pH 11, ZnO were poorly orientated with small diameter, and did not present as nanorods in the cross sectional view (Figure 2.2(D)).

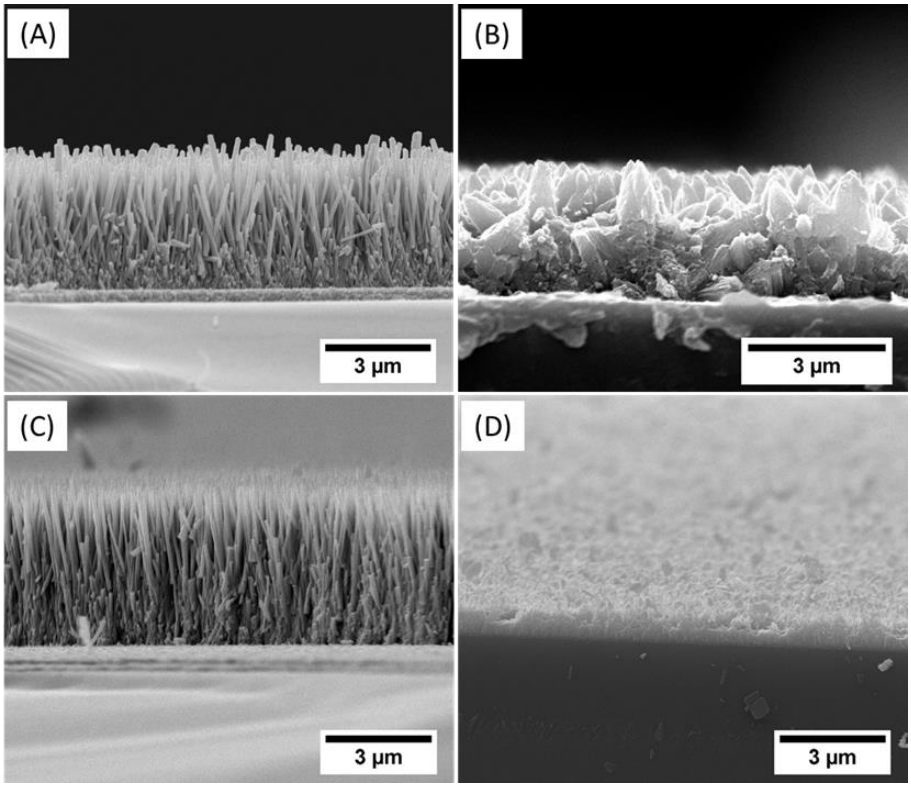

Figure 2.3 Cross-section SEM images of ZnO nanorods in different pH solutions. (A) pH 6, (B) pH 10, (C) pH 10.5, (D) pH 11.

The corresponding ZnO cross-sections as shown in Figure 2.3 also demonstrated that pH 6 was the most preferred growth condition in terms of ZnO nanorods growth even though it was predicted that higher pH would result in more ZnO reactant. It is believed that the Zn^{2+} precipitated quickly at high pH but contributed little to the crystal growth.

2.3.3 Effect of synthesis time and precursor concentration

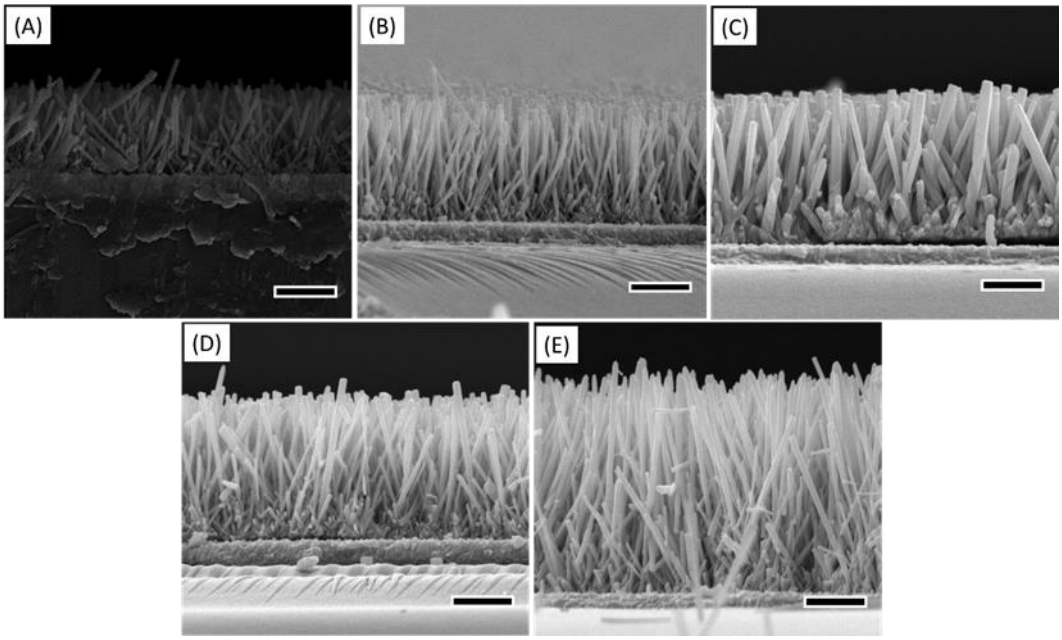

Figure 2.4 Cross-view SEM morphologies of ZnO nanorods synthesized with various durations and precursor concentrations. (A) 8 h, 10 mM, (B) 8 h, 25 mM, (C) 8 h 50 mM, (D) 16 h, 25 mM, (E) 24 h, 25 mM. The scale bar is 1 µm.

To achieve ZnO nanorods with high aspect ratio, one of the most commonly-used methods is to refresh the growth solution to extend the length of the rods, with assumption that the reaction ceases after around 2.5 h when homogeneous precipitation ceases [18], [78], [96], [269]. However, here we have studied a range of synthesis times and precursor concentrations to find the optimum conditions to achieve high-aspect-ratio ZnO nanorod using only a single growth step. Figure 2.4 shows cross-sectional morphologies of the ZnO nanorod arrays when the synthesis time and precursor concentration were altered. A uniform and dense array of ZnO nanorods was formed on seeded FTO-coated glass. The average diameter, length and aspect ratio are summarized in Table 2.1. The nanorods synthesized at 50 mM showed a lower aspect ratio compared to 10 mM and 25 mM. This can be explained by the growth of the non-polar face being less inhibited at high Zn^{2+} concentration, thus the ZnO nanorod diameter increased faster than at lower concentrations. The highest

aspect ratio was achieved at a concentration of 25 mM. Further investigating longer reaction times at this concentration showed that the length increased with the duration while the diameter showed no significant change, thus increasing the aspect ratio. The highest aspect ratio of 51 was achieved when using a 25 mM, pH 6 solution for 24 h.

Table 2.1 Diameter, length, and aspect ratio of ZnO nanorods synthesized by different concentration and duration.

Duration (h)	**Precursor concentration (mM)**	**Diameter (nm)**	**Length (μm)**	**Aspect ratio**
8	10	71.7 ± 2.7	1.6 ± 0.02	22
	25	74.0 ± 1.5	2.0 ± 0.01	27
	50	123.7 ± 2.6	2.5 ± 0.03	20
16	25	75.3 ± 2.0	2.5 ± 0.01	33
24	25	78.4 ± 2.7	4.0 ± 0.03	51

2.3.4 Characterization of the highest aspect ratio ZnO nanorods

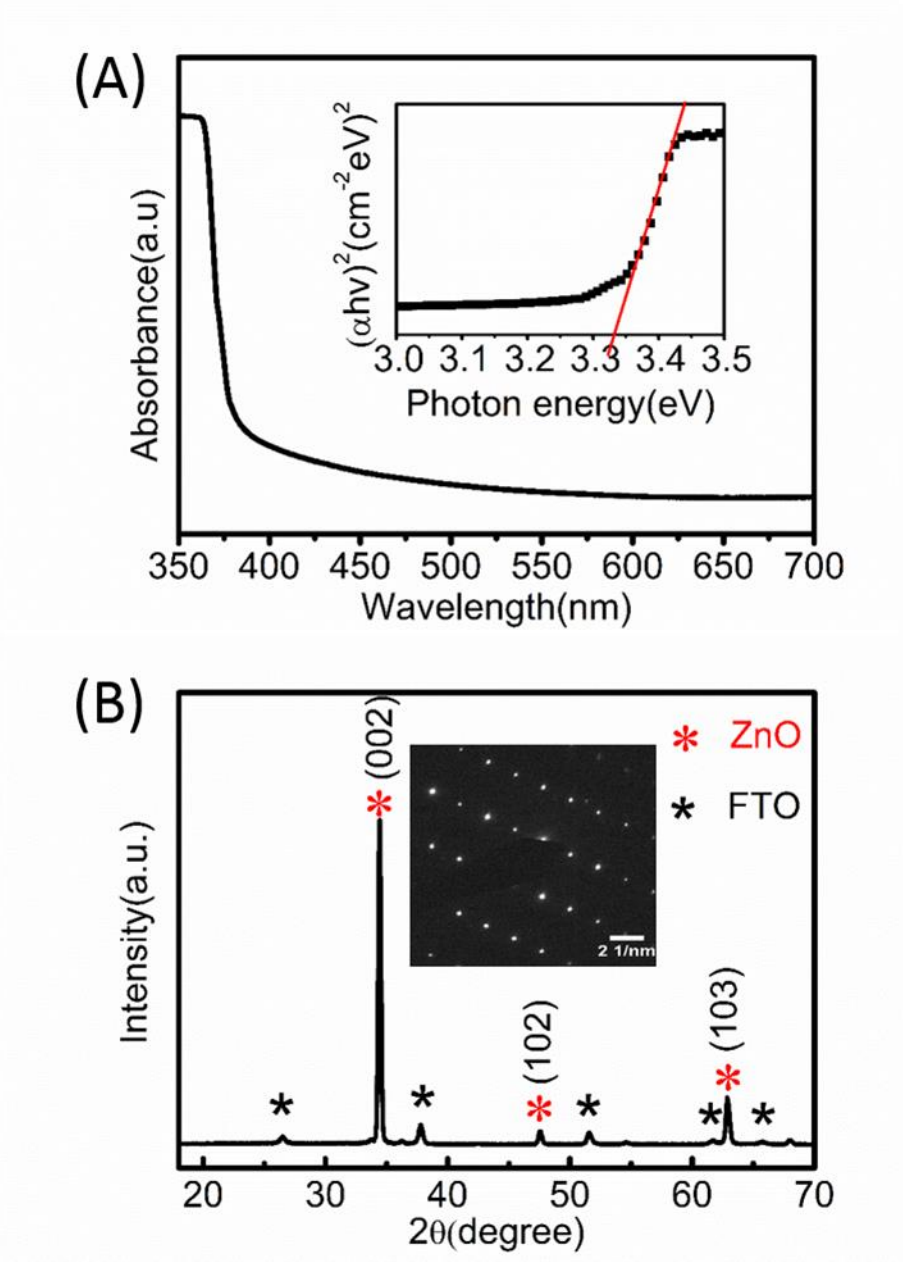

Figure 2.5 (A) UV-Vis absorption spectroscopy, inset Tauc-plot, and (B) XRD patterns, inset SAED diffraction patterns of ZnO nanorods.

The nanorods with the highest aspect ratio were analysed by UV-Vis absorption, X-ray diffraction and transmission electron microscopy. Figure 2.5(A) shows a typical ZnO absorption spectrum between 350-700 nm; light absorption significantly increased when the wavelength was less than 360 nm. A Tauc plot was used to determine the optical band gap of the semiconductor [270]:

$$\alpha h\nu = A(h\nu - E_g)^r$$ ***Equation 2.1***

where α is the absorption coefficient, h is the Planck's constant, ν is the light frequency, A is absorbance, E_g is the optical band gap and r is the nature of the transition. ZnO is a semiconductor with direct band gap, r is 0.5. Thus, for ZnO Equation 2.1 becomes

$$(\alpha h\nu)^2 = A(h\nu - E_g)$$ ***Equation 2.2***

The absorption coefficient (α) determines how far for a light can penetrate into a substrate before it is absorbed. The absorption coefficient depends on the material and on the wavelength of light which is being absorbed. In a material with a low coefficient, the light will be poorly absorbed. The extinction coefficient (k) of a material is defined as how easily it can be penetrated by light of a particular wavelength. The absorption coefficient is related to the extinction coefficient according to: $\alpha = {}^{4\pi k}/_{\lambda}$, where λ is the wavelength of a light [270].

The resulting plot is shown in the inset Figure 2.5(A), which had a distinctly linear regime that denoted the onset of absorption. Thus, extrapolating this linear region to the abscissa yielded the energy of the optical band gap of ZnO. As can be seen on the x-axis, a direct band gap of E_g = 3.34 eV was achieved. The value of E_g agrees well with previous work where the growth solution was refreshed to extend the nanorods [18]. A wurtzite crystal structure with preferred orientation in the c-axis was confirmed by the dominant (002) peak at 34.4° in the XRD pattern (JCPDS 36-1451) Figure 2.5(B)). The inset SAED pattern in Figure 2.5(B) also demonstrates that the nanorod array was highly crystalized.

2.3.5 Effect of annealing on oxygen vacancies in ZnO nanorods

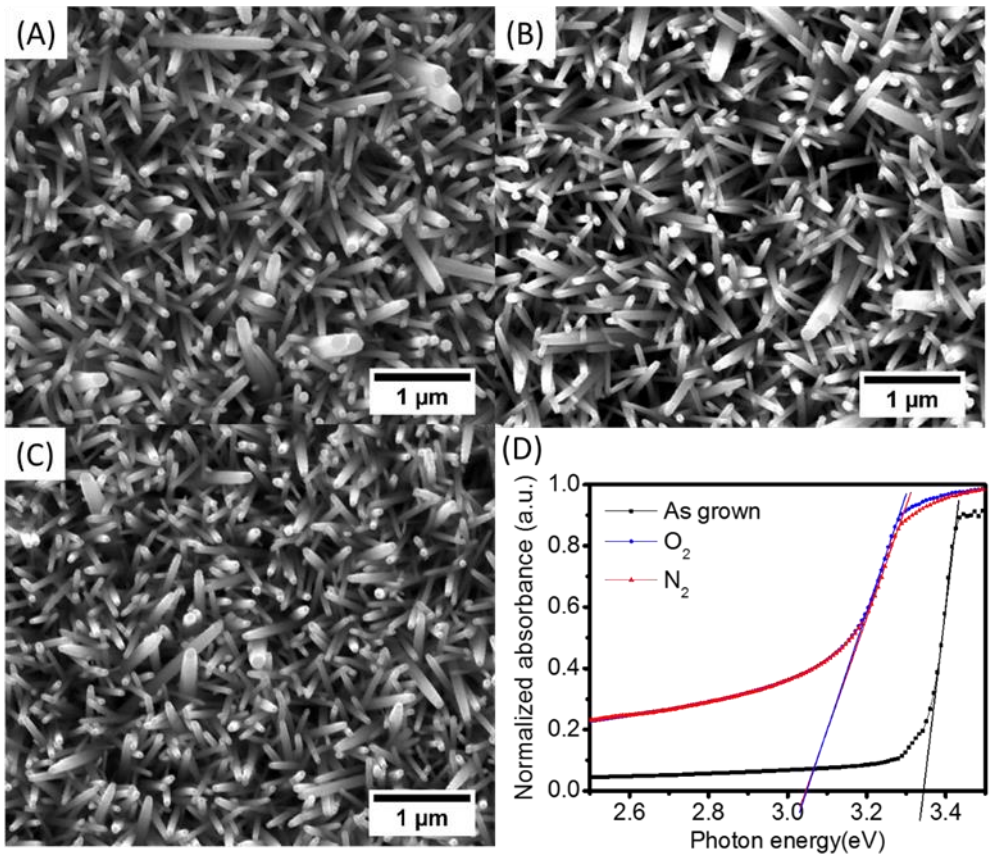

Figure 2.6 Top view (A)-(C) SEM morphologies of ZnO nanorods, (A) as-grown, (B) annealed in nitrogen, and (C) annealed in oxygen. (D) Tauc-plot of ZnO annealed in nitrogen, oxygen and as-grown.

ZnO nanorods synthesized by aqueous methods at low temperature (< 100 °C) contain defects both in the bulk structure and surface states [271], [272]. Thermal treatment is one of the most effective methods to remove these defects. Annealing of ZnO nanorods at 350 °C for 1 h in nitrogen and oxygen was investigated. Figure 2.6(A)-(C) display the morphology of ZnO after annealing. From the top view, there was no significant change on the surface, which differs from ZnO nanorods synthesized in a pH 11 growth solution [272]. However, as shown in the Tauc-plots of Figure 2.6(D), the band gap of ZnO nanorods annealed in N_2 and O_2 were the same, but both decreased by 0.29 eV compared to the as-grown nanorods.

2.4 ZnO/PEDOT:PSS diode structure

In order to compare the effect of the annealing conditions of these nanorods to the electrical properties, an organic semiconducting polymer, PEDOT:PSS, was spray coated on the surface of the ZnO nanorods.

2.4.1 Characterization of ZnO/PEDOT:PSS diode structure

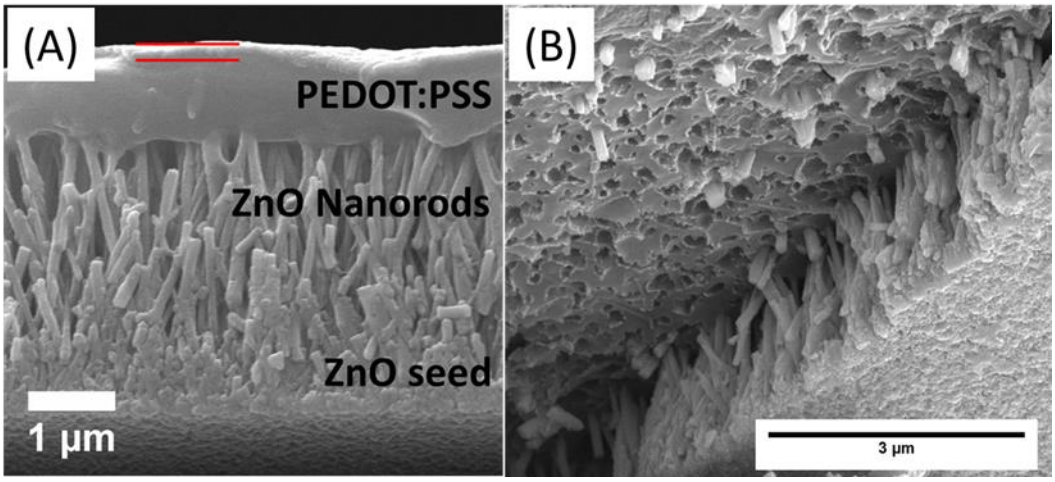

Figure 2.7 (A) Cross-section view of a device made of ZnO/PEDOT:PSS junction (gold layer indicated with red lines), (B) SEM image of ZnO/PEDOT:PSS interface with ZnO partially removed, the holes in the PEDOT:PSS layer originated from the tips of the ZnO nanorods which penetrated inside the layer.

Figure 2.7(A) depicts the cross-section of the ZnO/PEDOT:PSS structure, where the thickness of the p-type polymer layer was approximately 1 µm, and the gold contact 100 nm. As can be seen, the PEDOT:PSS layer penetrated partially into the nanorods to make good contact with tips of the n-type ZnO nanorods. It is known that polystyrene sulfonate (PSS) is an acid due to the sulfonate group and may therefore etch the ZnO nanorods. From Figure 2.7(A), the tips of ZnO nanorods were still well-defined; furthermore, observation of nanorods separated from PEDOT:PSS in Figure 2.7(B) demonstrates that there were rod-shaped holes in the PEDOT:PSS layer and

also the tips of the nanorods still embedded within the PEDOT:PSS film, which provided solid evidence that the PEODT:PSS did not etch ZnO.

The *I-V* characteristics of p-n junctions made of ZnO and PEDOT:PSS were measured at bias voltages between -1.5 and 1.5 V (Figure 2.8). The rectifying behaviour shown in the *I-V* curves confirmed that diodes were successfully produced. The device rectification ratios at ± 1.5 V of ZnO nanorods annealed in the different atmospheres are shown in Table 2.2. The rectification ratio of as-grown sample was 2.1 at ± 1.5 V, while it was improved to be 28.8 and 38 by thermal treatment on ZnO in oxygen and nitrogen. While these values are low compared to all-inorganic diodes made with ZnO nanorods discussed above, they are high compared to previous ZnO/PEDOT:PSS diodes [96], [273]. This therefore demonstrates the benefit of careful control of the ZnO composition through annealing.

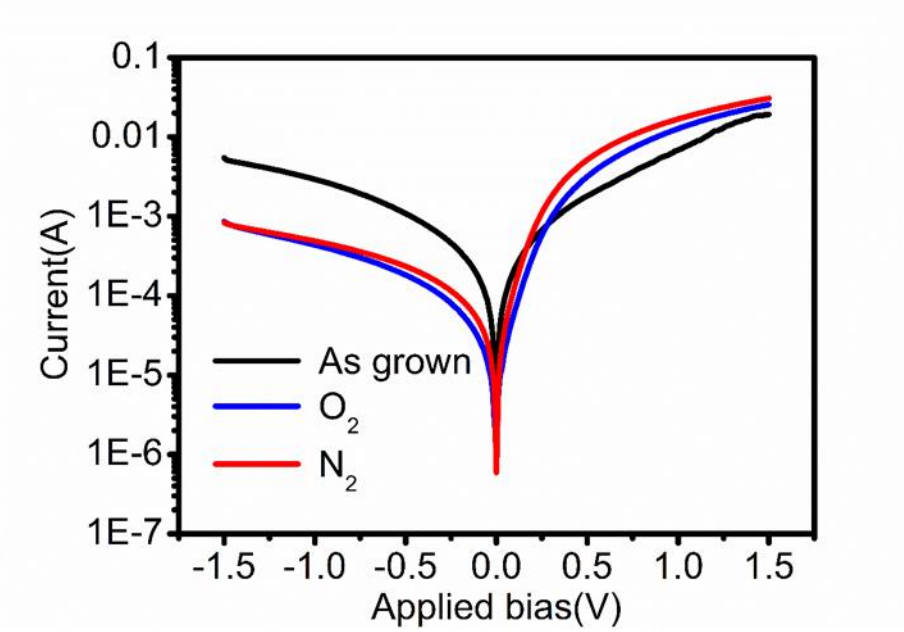

Figure 2.8 I-V characteristics of a device made with ZnO annealed in different atmospheres and without annealing.

2.4.2 Effect of annealing on ZnO/PEDOT:PSS diode structure

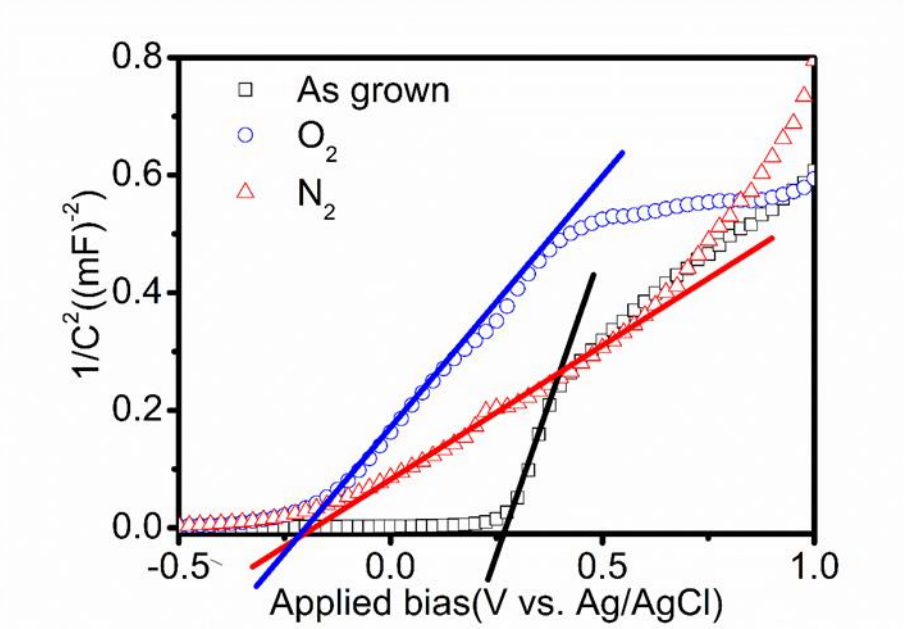

Figure 2.9 Mott-Schottky plots of ZnO annealed in different atmospheres and without annealing.

To understand the influence of the annealing atmosphere on the rectification ratio of devices made with ZnO nanorods, electrochemical impedance measurements were carried out to determine the capacitance of ZnO when in contact with an electrolyte. The Mott-Schottky equation was used to calculate the carrier concentration from these data: [274]

$$\frac{1}{C^2} = \frac{2}{e_0 e \varepsilon_0 N_d}\left[(V - V_{fb}) - \frac{kT}{e_0}\right] \qquad \textit{Equation 2.3}$$

where e_0 is the electron charge, ε the dielectric constant of ZnO, ε_0 the permittivity of vacuum, N_d the carrier concentration, V the applied potential, V_{fb} the flatband potential, and kT/e_0 is a temperature-dependent correction term. According to the Mott-Schottky equation, N_d is determined from the slope in the plot shown in Figure 2.9. The positive slopes confirmed that all ZnO nanorods obtained were n-type regardless of the annealing atmosphere. The carrier concentration was calculated and

is summarized in Table 2.2. The carrier concentration was highest in ZnO nanorods annealed in nitrogen, followed by oxygen and as-grown. It is of interest that the trend in the carrier concentration of ZnO after annealing correlated well with the device rectification ratio.

Table 2.2 Device rectification ratio, carrier concentration, and O 1s peak information of ZnO annealed in different atmospheres. Average and standard deviations of rectification ratio were taken from measurements of three devices for each condition.

	As-grown	**Oxygen**	**Nitrogen**
Rectification ratio at ± 1.5V	2.1 ± 0.7	28.8 ± 0.4	38.0 ± 0.4
Carrier concentration (10^{19} cm^{-3})	0.7	1.7	3.9
Oxide in lattice (at. %)	52.7	54.2	52.2
Oxygen vacancy (at. %)	27.2	26.6	35.8
Oxygen from -OH (at. %)	20.1	19.2	12.1

To investigate this relationship further, the O 1s peaks of three different samples were studied by high-resolution XPS (Figure 2.10). The O 1s peaks showed significant changes after annealing in nitrogen and oxygen; a shoulder appeared in the O 1s peak towards the higher energy direction. The O 1s peak was fitted using Gaussian fitting to three peaks, which were centred at 530.0 eV, 531.1 eV, and 532.1 eV. The peak at 530.0 eV corresponds to lattice oxygen anions (O^{2-}) in the wurtzite structure, the peak at 531.1 eV has been attributed to O_x^- (O_2^- and O^-) ions in the oxygen-deficient regions caused by oxygen vacancies, and the peak at 532.1 eV corresponds to –OH bond from adsorbed water at the surface [82]. The amount of oxygen species in different samples are listed in Table 2.2.

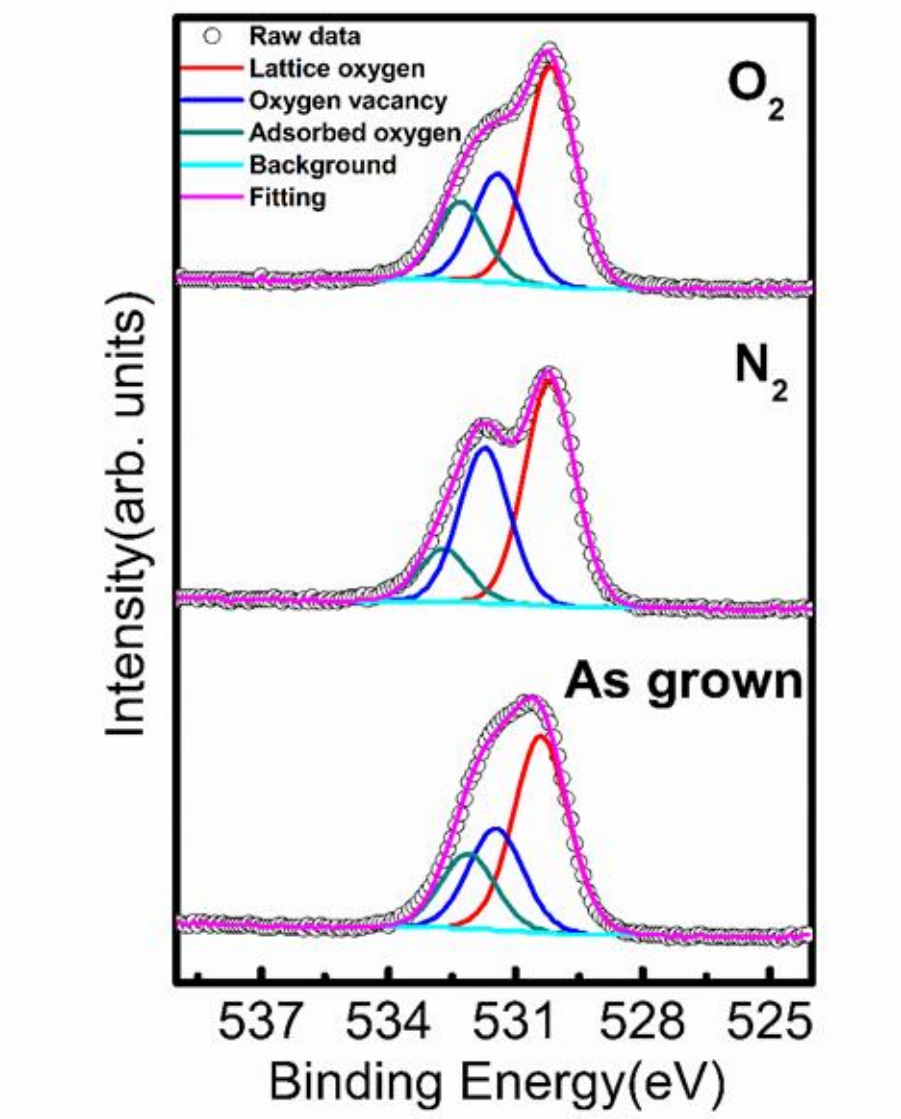

Figure 2.10 High-resolution O 1s XPS spectra of ZnO nanorods annealed in different atmospheres and without annealing. This provides strong evidence that the main source of n-type doping in these nanorods is oxygen vacancies, as previously identified for ZnO.

The oxygen vacancy content clearly decreased in ZnO with increased oxygen partial pressure in the annealing atmosphere, while the amount of adsorbed oxygen decreased during nitrogen annealing, as expected in a low oxygen partial pressure environment. The decrease in oxygen vacancies during annealing under high oxygen partial pressure can be explained by reactions between oxygen in the annealing gas and uncoordinated zinc at these sites on the surface, followed by diffusion of oxygen ions into the crystal

structure to oxygen deficient regions. The converse effect occurs during nitrogen annealing, where the low oxygen partial pressure leads to loss of oxygen at the surface, and a subsequent increase in the number of oxygen vacancies. The amount of carbon on the ZnO surface was also influenced by the annealing atmosphere, which was 49.8% in as grown ZnO, 40.0% in ZnO annealed in O_2, and 51.0% in ZnO annealed in N_2. When annealing in O_2 carbon-containing compounds on the surface will react with oxygen to be converted to CO_x and escape from the surface, resulting in a decrease of the amount of carbon.

To understand the photophysics of ZnO nanorods, steady state and time resolved photoluminescence spectroscopy was carried out on ZnO/PEDOT:PSS diodes using a 355 nm excitation wavelength. The normalized PL in Figure 2.11 shows a strong near band-edge emission at ~ 380 nm for all samples. The intensity of deep level emission in ZnO nanorods between 500-700 nm was observed to slightly decrease with high oxygen partial pressure during annealing. These PL results are in agreement with the XPS data, which can support that the annealing has an influence on impurities in ZnO.

The light emitted from ZnO was detected by a spectrometer, where a diffraction grafting separated the incoming light into different wavelength. The wavelength of 430 nm was selected from the PL spectra in Figure 2.11(A). The PL decay curves as shown in Figure 2.11 (B) were characterised by photo intensity vs. time. The decay curve obeys an exponential decay law:

$$I(t) = I_0 + A_1 e^{-t/\tau_1}$$

where I(t) is the intensity at a given time, I_0 is the background intensity, A_1 is the amplitude of the exponential, and τ_1 is the fluorescence life time.

PL lifetime for all main emissions seen in the as-grown nanorods were too short to measure using the 5 ns laser pulse, implying a lifetime of <5 ns. A measurable PL lifetime of annealed samples was found at 430 nm, giving 53.0 ns for nitrogen, and 51.9 ns for oxygen (Figure 2.11(B)). Therefore, the use of annealing in either nitrogen or oxygen has clearly reduced recombination rate, which is beneficial for many device applications. However, there is a negligible difference in the lifetime of samples annealed in nitrogen or oxygen at the timescale measured. This implies that oxygen-defect-induced carrier density is the main factor leading to the improved rectification of the diodes when annealed in nitrogen, as discussed above, not reduced recombination. However, ultra-fast spectroscopy could be studied in the future to identify whether there is a difference in recombination at faster timescales, particularly where optoelectronic application may be of interest.

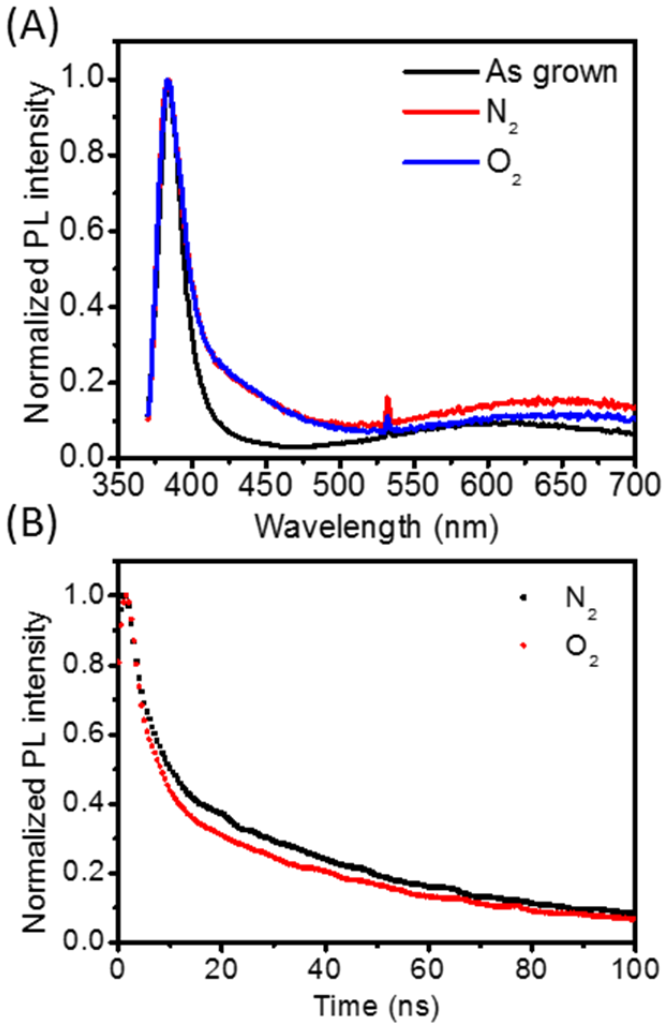

Figure 2.11 (A) Integrated photoluminescence spectra of ZnO/PEDOT:PSS annealed in different atmospheres and without annealing, (B) photoluminescence decay measured at an emission wavelength of 430 nm.

Comparing the Mott-Schottky, XPS, and PL results, there is a clear correlation between increased oxygen vacancies with low oxygen partial pressure annealing and high carrier concentration. Consequently, the different annealing atmospheres clearly have an effect on the carrier concentration of ZnO nanorods as well as the performance of the diode structures. Hence, the improved diode performance can be directly related to the increase in the oxygen-vacancy-related doping level in the ZnO crystal structure with decreased oxygen partial pressure during annealing.

2.5 Summary

ZnO nanorods were synthesized on seeded substrates using aqueous solution methods using a single step for 24 hours. Compared with the conventional method, which refreshes the growth solution to extend the nanorods, the as-achieved nanorods using a single step showed no significant difference in SEM morphology, UV-Vis absorption spectroscopy, XRD patterns, and SAED diffraction. The annealing atmosphere was related to the n-type carrier concentration and oxygen vacancy content using Mott-Schottky, PL, and XPS analysis. The carrier concentration of the ZnO nanorods and the rectification ratio in ZnO/PEDOT:PSS diodes increased with the decreasing oxygen partial pressure during annealing. These results clearly demonstrate that high aspect ratio ZnO nanorods can be produced in a single reaction step, and that by increasing the intrinsic oxygen vacancy-related defects through nitrogen annealing, high carrier concentration rods can be produced leading to improved diode performance. This indicates a promising route for a wide range of applications that can make use of such improved ZnO nanorod-based diode performance. While we have focussed on the optimisation of the ZnO nanorods to improve the rectification ratio of ZnO/PEDOT:PSS diodes in this work, further improvements of these devices would be achieved by control of the PEDOT:PSS properties, such as doping levels, which would be an interesting avenue for future work.

3 Assembly of a ZnO/Au Schottky diode and its application in ammonia gas sensors

3.1 Introduction

Metal oxide semiconductor based gas sensors have recently received a lot of attention, with the aim to detect hazardous volatile organic compounds for the protection of human health as well as environmental safety [128], [275]–[277]. A major issue of MOS gas sensors is the high operating temperature above 350 °C, which limits its application due to the high energy requirement and risk of ignition at high temperatures. Therefore, a lot of effort has been made to moderate the operating temperature, not only to meet the harsh demands but also to make portable and wireless gas sensor devices possible with low energy consumption. Recently, room temperature gas sensing based on metal oxide semiconductors has been achieved under either UV illumination [174], [278]–[280] or vibration [1], [176], [276], [281]. However, the responsivity, selectivity and stability of the devices still need to be improved. Conventional semiconductor gas sensors normally use interdigitated electrodes (IDE) as substrates which have drawbacks such as high cost and complex assembling processes. In this chapter, a room temperature gas sensor using a Schottky diode consisting of ZnO nanorods and a gold film on a conductive FTO substrate without illumination or vibration will be described.

In the last few years, efforts have been made towards developing high-performance gas sensors working at low temperatures (< 50 °C) with low cost [193]. Room temperature gas sensors have significant advantages such as low energy consumption

and possibility to be integrated with portable devices. For conventional metal oxide semiconductor gas sensors, the responsivity of the resistance is poor at room temperature. Two main factors might cause the poor behaviour: (1) the amount of oxygen adsorption species on the sensing layer is small; and (2) at temperature below 100 °C, oxygen molecules prefer to ionize to be O_2^- rather than O^- or O^{2-}, which largely restricts their activity when exposed to analytes [185]. At room temperature, reaction products such as water and other small intermediate organic compounds remain at the surface rather than desorb from the surface of semiconductors, therefore, the recovery time is much longer than at high working temperatures. The residue on the sensing surface also inhibits the re-adsorption of oxygen as well as slowing electron movement in the semiconductor's conduction band. UV illumination is an option to improve the sensitivity because photon-induced carriers may facilitate the reaction between the ionized oxygen and analytes. UV illumination with high intensity can heat up the device as well. Sunghoon Park and his colleagues presented an NO_2 gas sensor made of ZnO-SnO_2 composite, which has 2-3 fold enhancement in response due to UV illumination at room temperature [280]. However, the stability under intensive UV illumination was demonstrated to be poor. Other approaches have also been explored such as the use of vibration to decrease the working temperature using piezoelectric materials like ZnO. Under a constant vibrating frequency, the output voltage of a device has different values when responding to a target gas. Recently, Xue and co-workers reported that PANI/PTFE/PANI sandwich nanostructures is able to detect 210 ppm ethanol gas with a R_{air}/R_{gas} response of 66.8 at room temperature using a triboelectrification effect [281].

ZnO is one of the most studied materials for gas sensing devices due to its wide band gap, high carrier mobility as well as low cost and simple synthesis processes [282].

Nanostructured ZnO with specific size and dimensions has been demonstrated to gas sensing devices originating from the potential for a large surface-to-volume ratio, high specific surface area, large amount of surface active sites, as well as the recently recognized effect of certain crystal facets having particularly high surface reactivity [103]. Many examples of different kinds of nanostructures have been investigated and assembled into devices: nanoparticles [279], nanorods [174], nanowire [41], [283], nanoplates [284], as well as urchin-like structures [66] being the most common. In our work, ZnO nanorods were interfaced with gold, providing a well-defined Schottky diode.

Metal-semiconductor contacts have been investigated extensively due to their importance in direct current and microwave applications and as intricate parts of other devices. They have been used as photodetectors, solar cells and gate electrodes. When a metal makes contact with a semiconductor, a barrier is formed at the metal-semiconductor interface. The barrier is responsible for controlling the current conduction as well as its capacitance behaviour. Figure 3.1(a) shows the electronic energy relations of a high work-function metal and an n-type semiconductor which are not in contact. If the two are allowed to communicate with each other, for example by an external wire connection, charge will flow from the semiconductor to the metal and thermal equilibrium is established. This results in that the Fermi levels on both sides will line up. The work function is the energy difference between the vacuum level and the Fermi level. This quantity is denoted by $q\Phi_m$ for the metal and is equal to $q(\chi+\Phi_n)$ in the semiconductor, where $q\chi$ is the electron affinity measured from the conduction band maximum to the vacuum level, and $q\Phi_n$ is the energy difference between conduction band maximum and the Fermi level. When the gap distance between metal and semiconductor becomes small enough to be comparable to the interatomic

distances, the case is shown in Figure 3.1(b). It is clear that the limiting value of the barrier height is given by $q(\Phi_m - \chi)$. The barrier height is simply the difference between the metal work function and the electron affinity of the semiconductor.

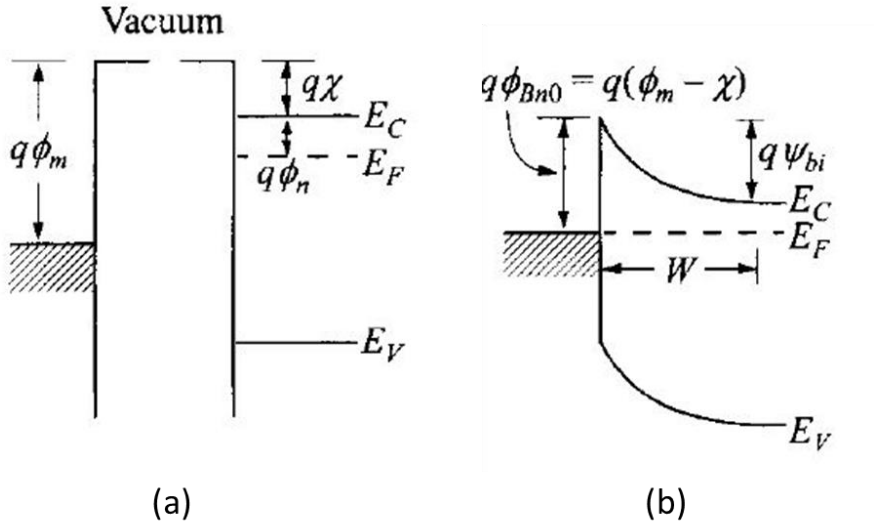

Figure 3.1Energy-band diagrams of metal-semiconductor contacts. Metal and semiconductor (a) in separated systems, and (b) the gap becomes zero. Adapted from Reference [285]

The energy-band diagrams for metals on n-type materials are shown under different biasing conditions in Figure 3.2. The thermal equilibrium case is shown in Figure 3.1(b). Under a forward bias, a potential step of V_F, the bands move when an electric field is applied. The electric field applied in the forward bias has the opposite direction as the built-in electric field, and the depletion region will decrease. The barrier on the semiconductor side, which the electrons have to overcome, is much smaller than under equilibrium conditions-the current from the semiconductor side is now bigger than the one from the metal. This results the current flows. Under a reserve bias, the applied electric field has the same direction as the built-in electric field and the depletion region will widen. The electrons will across a larger barrier height than under

equilibrium, which results in limited current flowing from the metal side to semiconductor side.

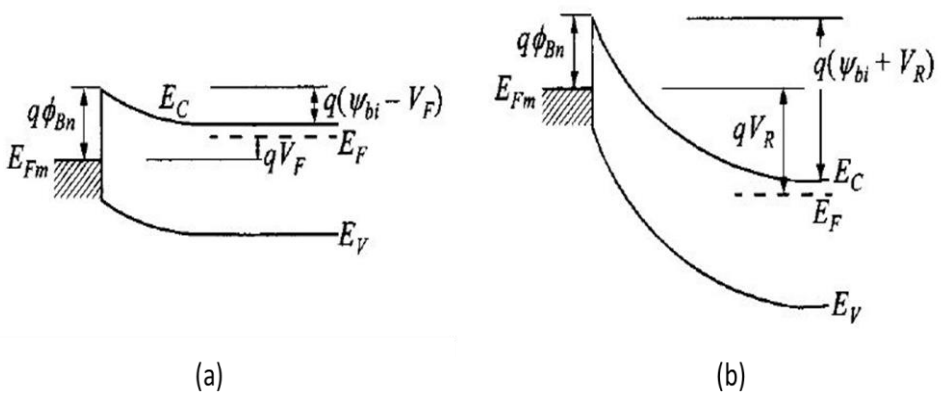

Figure 3.2 Energy-band diagrams of metal on n-type semiconductor under (a) forward bias, and (b) reverse bias. Adapted from Reference [285]

The thermionic-emission theory by Bethe is derived from the assumptions that:

(1) The barrier height $q\Phi_b$ is much larger than kT;

(2) Thermal equilibrium is established at the plane that determines emission;

(3) The existence of a net current flow does not affect this equilibrium so that one can superimpose two current fluxes-one from metal to semiconductor, the other from semiconductor to metal, each with a different quasi Fermi level.

With the assumption that the current is due to the thermionic-emission theory, the relation between the applied forward bias and the total current density can be expressed as [286]

$$\mathrm{I} = I_0 exp\left(\frac{qV}{nkT}\right)\left[1 - exp\left(\frac{-qV}{kT}\right)\right] \qquad \textbf{\textit{Equation 3.1}}$$

where n is the ideality factor, T is the temperature in Kelvin, q is the electron charge, k is the Boltzmann constant and I_0 is the reverse saturation current, at room temperature (293 K), kT/q = 0.025 V. For V > kT/q, Equation 3.1 can be written as

$$\mathrm{I} = I_0 exp\left(\frac{qV}{nkT}\right) \qquad \textbf{\textit{Equation 3.2}}$$

the reverse saturated current can be extracted by extrapolating the straight line of ln$I$ -V to intercept the axis at zero voltage

$$\ln I = lnI_0 + \frac{q}{nkT}V \qquad \textbf{\textit{Equation 3.3}}$$

The current in forward bias quickly becomes dominant I_0 and n can be determined by the linear fitting in the region of the ln I - V plot as shown in Figure 3.11 Semilogarithmic presentation of the I-V curves of a ZnO/Au Schottky diode at room temperature in air and 40 ppm ammonia gas (a) from -1 to +1 V, (b) for forward voltages, (c) energy band configuration of a ZnO/Au Schottky diode gas sensor with a forward voltage of 0.5 V in air and in ammonia(b). Assuming that the thermionic emission is the most predominant mechanism, I_0 can be expressed as

$$I_0 = AA^*T^2 exp\left(\frac{-q\Phi_b}{kT}\right) \qquad \textbf{\textit{Equation 3.4}}$$

where A is the effective diode area, A^* is the effective Richardson constant which is equal to 32 $Acm^{-2}K^{-2}$ for ZnO [287] and Φ_b is the zero-bias barrier height.

3.2 Experimental section

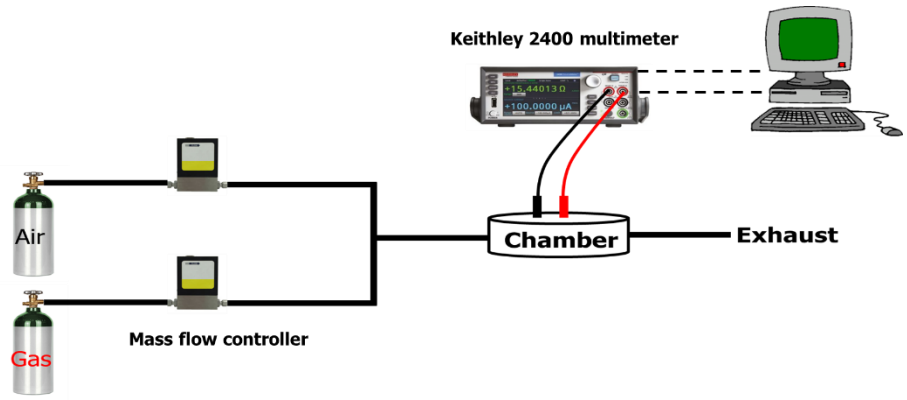

Figure 3.3 Schematic of custom-designed gas sensor test rig.

ZnO nanorods were produced on FTO-coated glass substrates using a solution method as described in Chapter 2. In this work, the ZnO nanorods were annealed in air at 350 °C for 2 h. The device was completed by evaporating a gold contact with a stripe patterned mask at approximately 100 nm on the surface. Regions around the active area were blocked using PMMA to prevent short circuits, which was spread from a 9 wt % solution in methoxybenzene and dried at 100 °C. The ZnO/Au diode gas sensor was placed in a custom designed chamber with a gas inlet and outlet. The chamber can be sealed with screws, it has two copper electrodes with two contacts that can connect to a multimeter. The device electrodes, FTO and gold, were copper taped and then silver painted on the copper plates to create ohmic contacts. All the contacts were protected by epoxy. For comparison, ZnO nanorods were produced on the interdigitated electrode (IDE) substrates using the same recipe as that on the FTO-coated glass.The resistance change was monitored at a constant 0.5 V using a multimeter (Keithley 2400) that was controlled by a custom written Labview software. The schematic of test system is shown in Figure 3.3. Gas was introduced into the

chamber by mass flow controllers, a flow rate 1 L/min was recorded by a gas flowmeter. All the gases were diluted with synthetic air and purchased from BOC.

3.3 Results and discussions

3.3.1 Characterization of a ZnO/Au Schottky diode

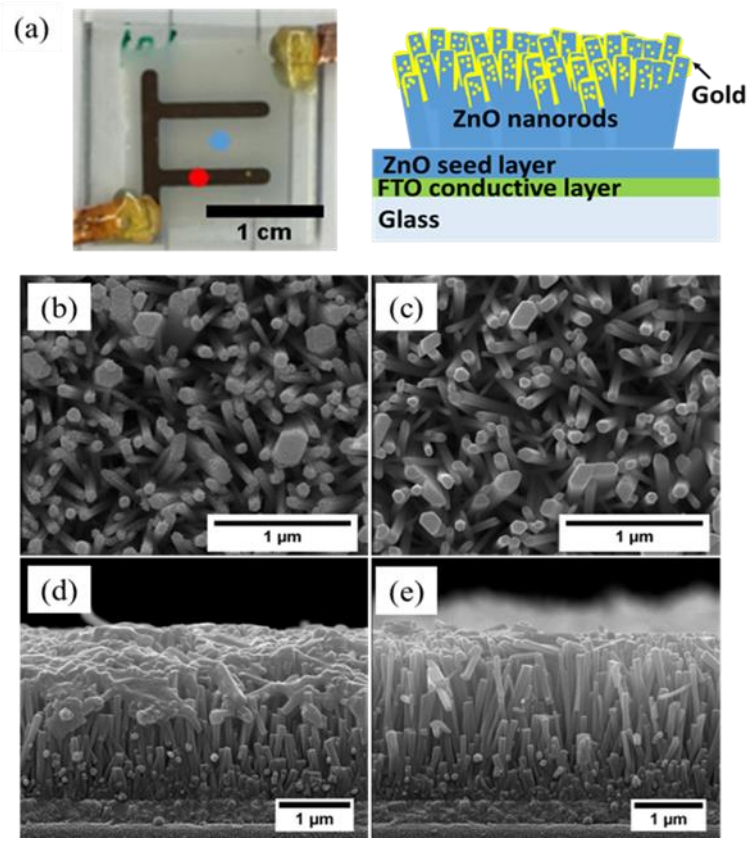

Figure 3.4 (a) Device photo and its schematic, the blue and red dot indicates the uncoated and coated area, top-view SEM images (b) coated area, (c) uncoated area; (d), (e) the corresponding cross-section of (b) and (c).

Figure 3.4(a) shows a ZnO/Au Schottky diode gas sensor device and a schematic of its side view. The gold electrode was patterned on the ZnO surface, which facilitates gas to access to ZnO nanorods. The SEM image of coated area in Figure 3.4(b) (indicated by the red dot in Figure 3.4(a)) illustrates a rough surface with some gold particles visible on the ZnO nanorods. The corresponding cross-sectional view in

Figure 3.4(d) shows a clear gold cover on the top of the ZnO nanorods, which was used as an electrode. No gold is observed on the bottom of the ZnO nanorods, which means the evaporated gold particles did not reach the FTO layer. However, there are some gold particles visible along the sides of the nanorods. The uncoated area is shown in Figure 3.4(c) and (e), the ZnO nanorods have smooth and clear surfaces, which is typical for ZnO made by solution phase synthesis and has been discussed in Chapter 2.

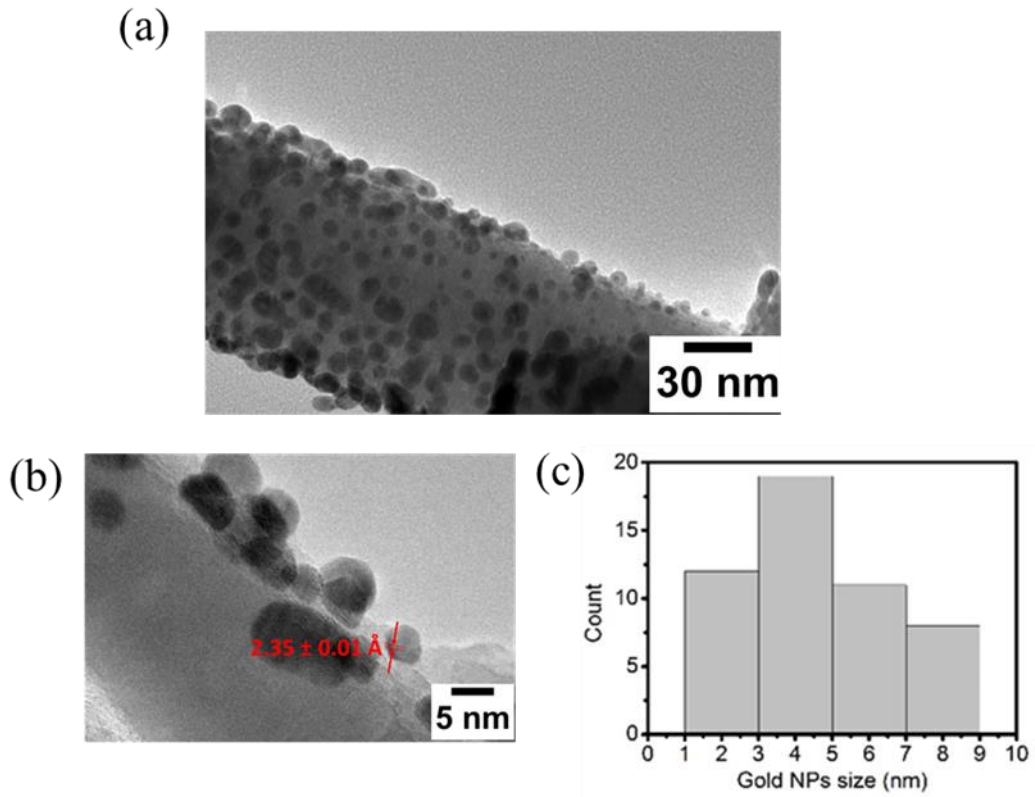

Figure 3.5 (a) TEM image of ZnO with gold particles, (b) large magnitude TEM image, (c) gold particle size distribution.

Metals have different functions when in contact with semiconductors depending on their nanostructure. To study what type of gold was deposited on the ZnO nanorod surface, TEM images were taken and are shown in Figure 3.5(a). The inset of Figure 3.5(a) shows a single nanorod with gold nanoparticles randomly distributed, the lattice

spacing was 2.35 ± 0.01Å, which agrees with the internal lattice spacing of the (111) plane of face-centred-cubic (fcc) gold (d = 2.355 Å, ICCD Card No. 04-0784). Figure 3.5(b) is the histogram of the gold particle size distribution; an average diameter of 5.7 nm was determined. According to the SEM and TEM images, there were two forms of gold which were particles on the middle of the nanorods and a film on the top of the nanorods. At the beginning of the deposition, the gold evaporation rate was small; thereby the small gold particles could penetrate to reach the middle of the nanorods. The evaporation rate automatically increased with time; when the rate was high, the gold particles accumulated to become a film on the top. Another reason might be that the gold could penetrate because the gaps between the nanorods were open at the beginning, later a film formed on the top and no more gold could penetrate into the spaces between the nanorods. Figure 3.6 shows the *I-V* curve of a ZnO/Au Schottky diode, the rectifying behaviour demonstrates that a diode was produced successfully. The rectification ratio at ± 1.5 V was 5500. The high rectification value shows that a Schottky barrier had been formed between ZnO and gold.

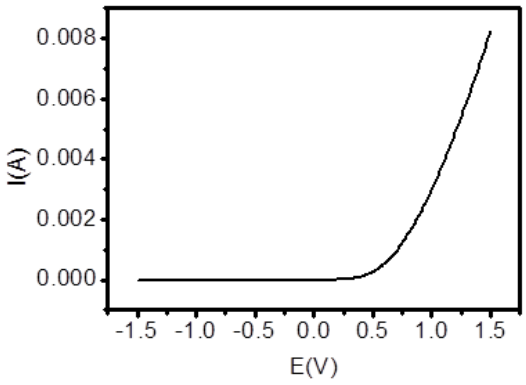

Figure 3.6 I-V curve of the ZnO/Au Schottky diode.

3.3.2 Gas sensing properties of a ZnO/Au Schottky diode

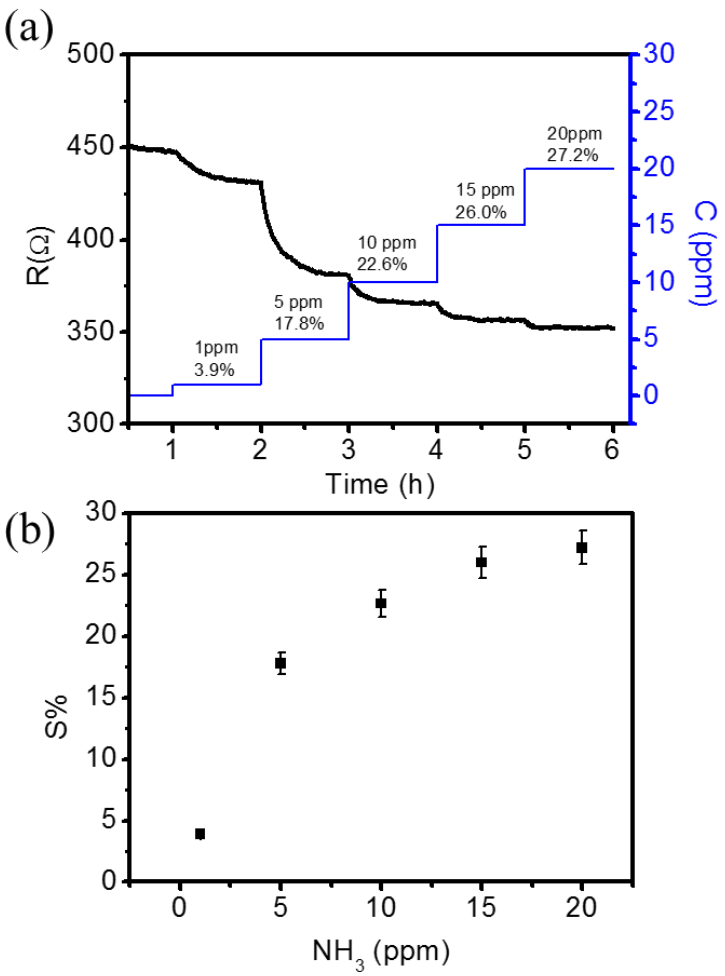

Figure 3.7 (a) Resistance change of a ZnO/Au Schottky diode versus time at different concentrations (C) of ammonia gas at room temperature, (b) the responsivity (S) versus ammonia concentration at room temperature.

The resistance of a ZnO/Au Schottky diode sensor at room temperature was recorded against time at 0.5 V (Figure 3.7(a)). Prior to introducing ammonia gas into the test chamber, a resistance of 450 Ω was measured in air, which was treated as the baseline of the device. When 1 ppm ammonia gas was introduced into the test chamber, the resistance of the ZnO/Au Schottky sensor decreased by 3.9% and saturated afterward. The resistance decreased further when ammonia concentration was increased. The mechanism of resistor gas sensor is described in Chapter 1. At temperatures below

100 °C, oxygen molecules were ionized to be O_2^- at the air-ZnO interface, the chemically active oxygen ions and the trace ammonia molecules reacted at the gas-solid interface. The redox reaction released the trapped electrons back to ZnO resulting in an increased electron concentration in the conduction band, therefore the resistance decreased. As the ammonia concentration increased, the resistance decreased further as more electrons were released by the reaction.

Figure 3.7(b) shows the responsivity *S* of ZnO/Au Schottky diode sensor versus the ammonia concentration at room temperature. The responsivity can be expressed as

$$S\% = \frac{R_{air} - R_{gas}}{R_{air}} \times 100\%$$

where R_{gas} is the value of the resistance measured in gas and R_{air} is the base line of resistance measured in air. The responsivity of the ZnO/Au Schottky diode gas sensor increased with an increasing concentration of ammonia at room temperature, which gave evidence that a Schottky diode structure can work at decreased operating temperatures. The responsivity in Figure 3.7(b) shows a non-linear relationship with gas concentration and approaches saturation at high concentration, which is likely due to the limited quantity and activity of oxygen ions on the ZnO nanorod surface at room temperature.

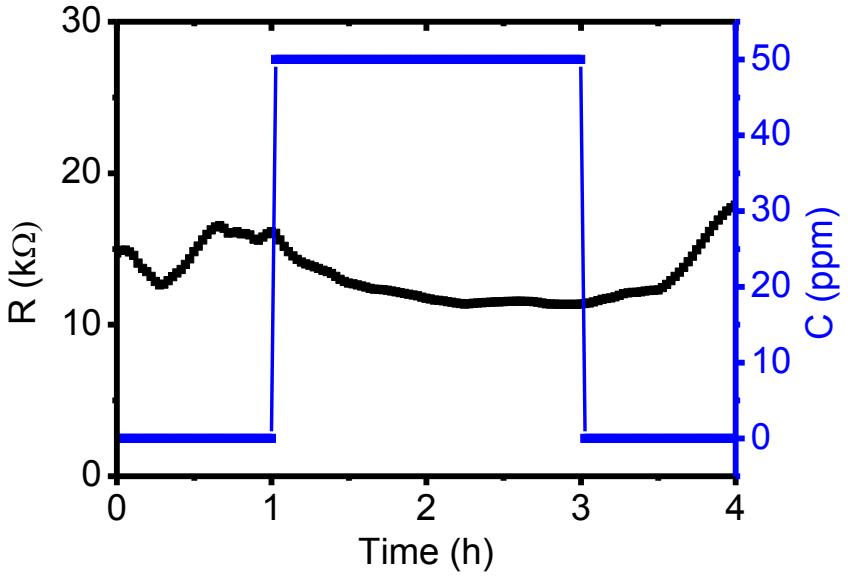

Figure 3.8 Ammonia response of ZnO nanorods on IDE substrates at room temperature.

A traditional metal oxide semiconductor based resistive gas sensor device has a chemically active semiconductor layer above the IDE substrate with heating circle in the back. It measures the resistance change across the grain boundary at high operating temperatures. To study the function of the Schottky structure in gas sensor, devices made of ZnO nanorods on IDE had been investigated. Figure 3.6 shows the resistance of ZnO nanorods at room temperature under the same applied bias of 0.5 V was much higher than that in the ZnO/Au Schottky diode. The resistance of ZnO nanorods on IDE substrate in the air was not stable and it did not have significant change after 50 ppm (the limit concentration of ammonia gas in our measurements) ammonia was inlet.

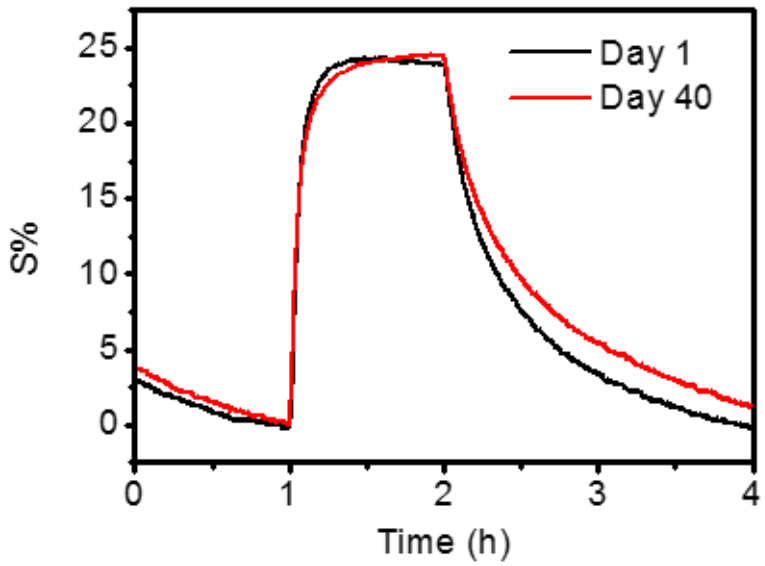

Figure 3.9 Stability of a ZnO/Au Schottky diode gas sensor response to 40 ppm ammonia gas at room temperature.

Stability of a device is another important property in practical applications to maintain its electrical properties, especially sensitivity, over long periods. Figure 3.9 shows the response of a device to 40 ppm ammonia gas before and after 40 days at room temperature. After 40 days, the responsivity remained almost the same, while the response time (time required from baseline to 90% of the resistance in NH_3) increased from 540 s to 792 s and the recovery time (time required from resistance in NH_3 to 10% of the baseline) increased from 4212 s to 5868 s, which might be due to surface contamination over a long time in air. The stability test of the ZnO/Au heterojunction in ammonia gas also demonstrated that the structure of the Schottky diode was stable over a long time.

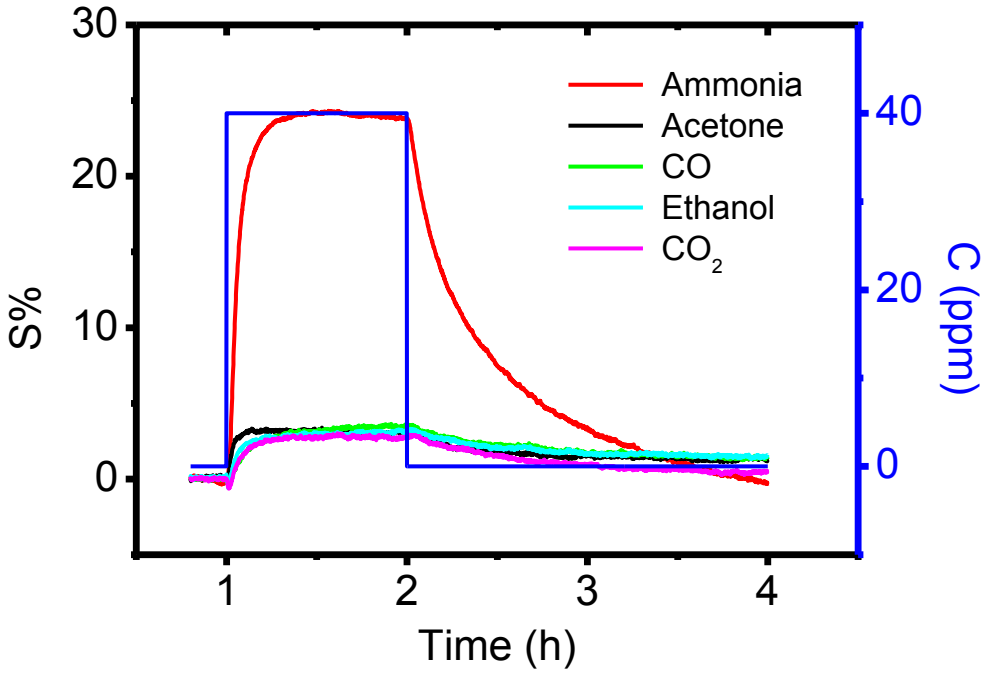

Figure 3.10 Responses of ZnO/Au Schottky diode sensor to different gases of 40 ppm concentration (C) at room temperature.

Selectivity is one of the most important properties in sensing devices. Figure 3.10 shows the responsivity of a ZnO/Au Schottky diode sensor to some of the most common gas analytes with a concentration of 40 ppm. The responsivity was more than 5 times greater in ammonia than in other gases. This is likely because ammonia was more active at room temperature than other gases to react with ionized oxygen species at the interface.

3.3.3 Mechanism of a ZnO/Au Schottky diode gas sensor

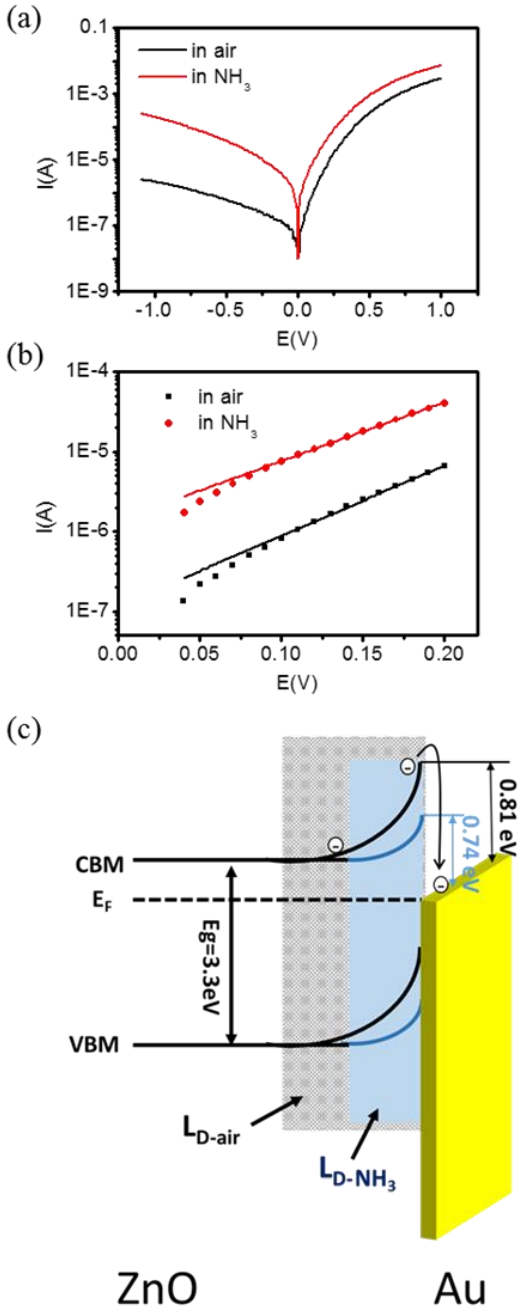

Figure 3.11 Semilogarithmic presentation of the I-V curves of a ZnO/Au Schottky diode at room temperature in air and 40 ppm ammonia gas (a) from -1 to +1 V, (b) for forward voltages, (c) energy band configuration of a ZnO/Au Schottky diode gas sensor with a forward voltage of 0.5 V in air and in ammonia.

To understand the mechanism of the ZnO/Au Schottky diode acting as an ammonia gas sensor at room temperature, the electrical properties were studied by measuring the *I-V* characteristics in air and 40 ppm ammonia gas, respectively. The Schottky diode displayed rectification ratio of 1400 in air and 36 in ammonia gas at ± 1 V at room temperature as shown in Figure 3.11 Semilogarithmic presentation of the I-V curves of a ZnO/Au Schottky diode at room temperature in air and 40 ppm ammonia gas (a) from -1 to +1 V, (b) for forward voltages, (c) energy band configuration of a ZnO/Au Schottky diode gas sensor with a forward voltage of 0.5 V in air and in ammonia(a).

The value of n, I_0 and Φ_b were determined according to the thermionic theory and are listed in Table 3.1.

Table 3.1 Summary of a ZnO/Au Schottky diode at room temperature in air and in ammonia.

	in air	**in 40 ppm ammonia**
Φ_b (V)	0.81	0.74
I_0 (μA)	0.12	1.4
n	20.3	17

The barrier height at zero-bias of the ZnO/Au Schottky diode was smaller in ammonia gas than in air. With a forward bias of 0.5 V, the released electrons from the redox reactions were easily transferred across the smaller barrier height resulting in a decreased resistance when ammonia gas molecules were introduced (Figure 3.10(c)). The width of depletion layer in air ($L_{D\text{-}air}$) was greater than that in ammonia gas ($L_{D\text{-}NH_3}$). The reverse saturated currents were also in agreement with the barrier heights, as a higher current was recorded in ammonia gas. Therefore, by determining the barrier heights and reverse saturated currents of the diode sensors, the detection of ammonia

gas at room temperature is based on the difference of barrier height in different atmospheres.

Another possible mechanism is either the chemical or electronic sensitisation as described in section 1.3.2.2 by gold particles on the surface of ZnO. Ramgir et al. have reported a room temperature gas sensor of gold nanoparticles dispersed on ZnO nanorods that can detect H_2S due to catalytic and electronic sensitisation effects [215]. The gold nanoparticles as shown in the Figure 3.2(a) could act as a chemical promotor to decrease the reactive energy of ammonia gas molecule and oxygen at the ZnO surface, which would give good responsivity and selectivity to ammonia gas at room temperature.

3.4 Summary

ZnO/Au Schottky diode gas sensors were produced using a simple method by depositing a 100 nm gold on ZnO nanorods. TEM and SEM images confirmed that the gold not only formed as a film on the top but also nanoparticles in the centre of the nanorods. A rectification ratio of 5500 at ± 1.5 V was determined by *I-V* characteristics. Gas sensing tests showed that at room temperature, the ZnO/Au Schottky diode had responsivity of 27.3% towards 20 ppm ammonia gas and a promising selectivity compared to some most common gases such as acetone, carbon monoxide, and ethanol. A stability test over a long period of the ZnO/Au Schottky diode showed it to be suitable for use in a gas sensor for the detection of ammonia gas at room temperature. The mechanism of ammonia detection at low temperature was determined by the difference in barrier height of the ZnO/Au Schottky diode in different atmospheres. The gold nanoparticles on the ZnO nanorod surface also may act as a chemical catalyst to enhance the responsivity and selectivity. The successful demonstration of the

Schottky diode made with ZnO nanorods and gold gives an alternative and simple way to decrease the operating temperature, making it possible to be integrated with portable wireless devices.

4 Light addressable potentiometric sensor using ZnO nanorods as sensing substrate in bioanalytical applications

4.1 Introduction

As introduced in section 1.4, LAPS belong to sensor family of potentiometric sensors capable of measuring charged species. LAPS is a photocurrent imaging technique that can also be used to visualise the reaction of biological analytes above the chip.

In this chapter, ZnO nanorods were used for LAPS measurements without the presence of an insulator. Given that ZnO has high electron mobility, high thermal conductivity, direct wide band gap, large exciton energy, ease of synthesis and low cost, it has been shown to be a promising semiconductor material for a wide range of applications, including energy harvesting systems [18], [95], [265], chemical and biological sensors [4], [174]–[176], [288], and photocatalysts [289], [290]. Nanostructured ZnO, for example nanorods, is currently attracting significant attention given that it increases the active surface sites, improves charge generation efficiency, and reduces the cost as well as simplifies the process. The n-type conductivity caused by oxygen vacancies in ZnO makes it possible to excite charge carriers with light with photon energy less than its bandgap of 3.3 eV [107], [291]. In this work, ZnO nanorods without an insulator layer are excited to generate AC photocurrents with a 405 nm diode laser that is a commonly used light source in LAPS. The morphology, optical properties and crystal structure of ZnO nanorods synthesized by one of the simplest and cheapest methods of aqueous synthesis were investigated. Photocurrent response, pH sensitivity, 2-D photocurrent images, the effect of the ZnO morphology on the lateral resolution and a

disposable biosensor using ZnO nanorods were examined with a LAPS setup that is shown in Figure 4.1.

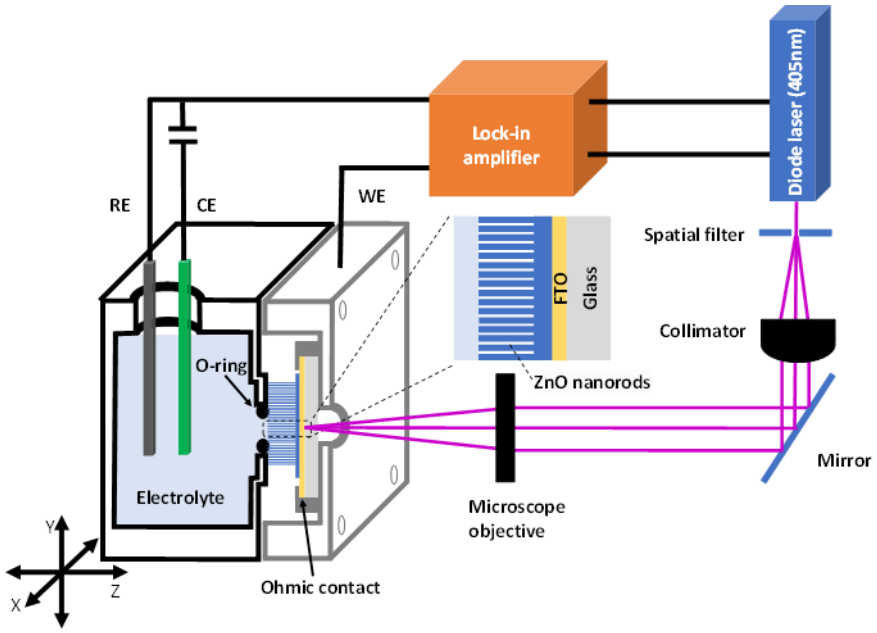

Figure 4.1 LAPS setup consisting of a diode laser, an electrochemical cell, a positioning system that can move the electrochemical cell with respect to the laser beam and a lock-in amplifier.

4.2 Experimental section

4.2.1 ZnO synthesis and characterization

ZnO nanorods were synthesized on FTO-coated glass using a solution method described in Chapter 2. The ZnO film was produced in a 100 mM equivalent molar HMT and zinc nitrate solution. In both cases, the jar was placed into a pre-heated oven (Memmert, Co. KG) for 24 h at 90 ºC. Afterward, the substrate was washed with distilled water and dried with nitrogen. The ZnO nanorods and the ZnO film were annealed in a box furnace (Lenton, UK) at 350 ºC in air for 1 h. For CVD ZnO produced by Jianwei Li from UCL, the laboratory aerosol assisted chemical vapour

deposition (AACVD) set-up is illustrated in elsewhere [292]. The AACVD precursor was prepared by dissolving 0.4 g zinc acetate dihydrate in 25 mL methanol. The substrates were placed on a graphite block in the reactor and preheated to 450 ºC. The as-prepared precursor solutions were transferred to a Drechsel bottle, and then ultrasonic humidifier with operating frequency of 1.6 MHz generated an aerosol mist. The mist was continuously passed through the reaction chamber with nitrogen carrier gas at 1.5 L/min until exhausted. The carrier gas was kept flowing until the temperature of the reactor chamber dropped below 80 ºC. The total deposition time was 45 ± 5 min. The surface and cross-sectional morphology of ZnO nanorods and film were examined using a SEM (FEI Inspect F). Absorption spectra of ZnO were measured by UV-Vis spectrometer (Perkin Elmer, Lamda 950). High resolution XPS was carried out by Thermo Scientific K-Alpha^{+}. XPS data were analyzed by CasaXPS^{TM} software with a calibrated C 1s peak of 284.8 eV.

4.2.2 Linear sweep voltammetry

An Autolab PGSTA30/FRA2 (Windsor Scientific Ltd., UK) was used to carry out linear sweep voltammetry (LSV, scan rate was 5 mV/s) in 0.2 M Na_2SO_4; a platinum electrode and a Ag/AgCl electrode were used as counter and reference electrodes, respectively. A diode laser (λ = 405 nm, max 500 mW) was used as the light source. The illumination was chopped in 10 s intervals.

4.2.3 LAPS and SPIM measurement

The LAPS setup is shown in Figure 4.1 [225]. The electrochemical cell was mounted on an M-VP-25XL XYZ positioning system (50 nm motion sensitivity, Newport, UK) to adjust the sample position for 2-D XY scans and focusing in the Z direction. An electronically modulated, focused diode laser LD1539 (Laser 2000, λ =405 nm, max

50 mW, focused spot diameter ≈ 1 μm) was used as the light source for LAPS measurements. AC photocurrents were measured with an EG&G 7260 lock-in amplifier. A platinum electrode and an Ag/AgCl electrode acted as counter and reference electrodes, respectively. The electrolyte was 10 mM pH 7.4 phosphate-buffered saline (PBS) solution. PMMA (Aldrich, average M.W. 120000) was dissolved to form a 11 wt% solution in methoxybenzene (Sigma-Aldrich, 99%). A drop of PMMA solution was deposited on the ZnO nanorods and dried without assistance at room temperature. The average and standard deviation of maximum photocurrent in three different ZnO were obtained by randomly selected 20 points from the photocurrent image.

4.2.4 Enzymatic degradation of a thin polymer film

The synthesis and purification of the polymer, poly(ester amide), was described by Sumner et al. [293] α-Chymotrypsin, type II, from bovine pancreas with activity of 40 units/mg was supplied by Sigma-Aldrich. A 1 μL drop of solution of 200 mg/mL poly(ester amide) in chloroform was deposited on the surface of ZnO and dried overnight without assistance. A 100 mM α-chymotrypsin solution in a pH 7.3 buffer was kept at -20 ºC in prior to use. During the degradation, LAPS photocurrent images in a range of 3000 μm with a step size of 30 μm were taken every 2 h at 1.5 V with a focused laser modulated at 10 Hz. The area of the polymer was calculated using ImageJ, version 1.51k.

4.3 Results and discussion

4.3.1 Characterization of ZnO nanorods

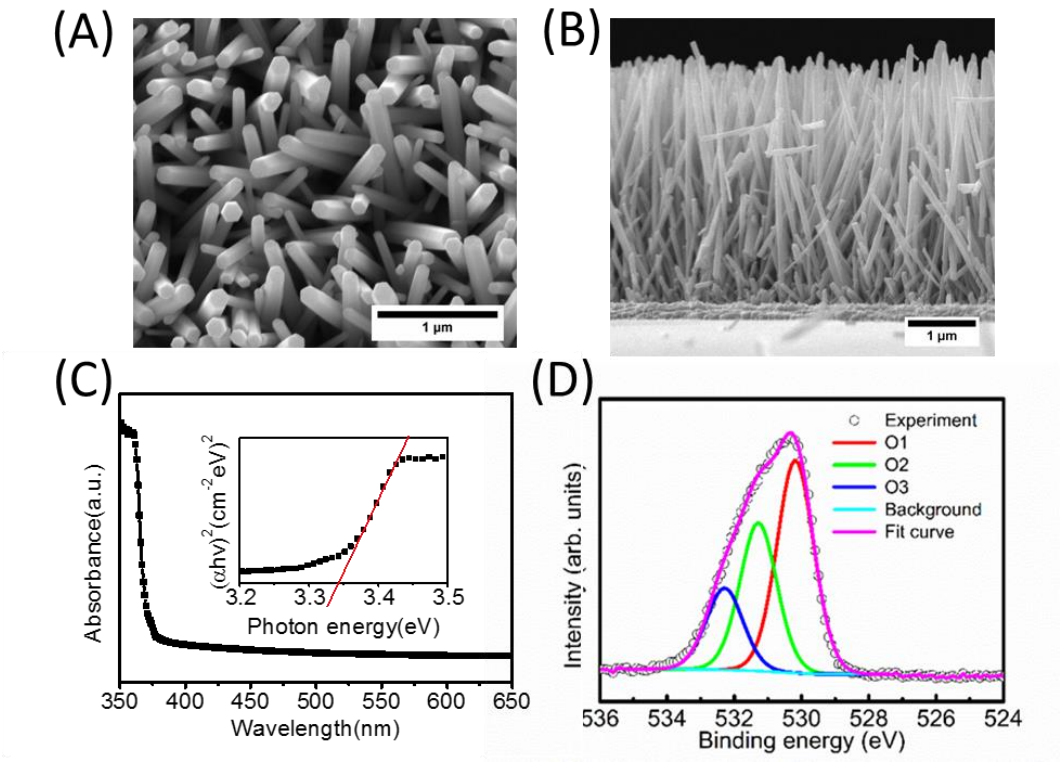

Figure 4.2 SEM images of ZnO nanorods (A) top view, (B) cross section; (C) UV-Vis spectrum and inset Tauc-plot, (D) High-resolution O 1s XPS spectrum of ZnO nanorods.

An array of ZnO nanorods formed uniform and well-oriented hexagonal shapes with 4.03 ± 0.025 µm length and 78.4 ± 2.7 nm diameter (Figure 4.2(A) and (B)) resulting in an aspect ratio of 51, which is described in Chapter 2. Optical properties of ZnO nanorods were investigated by UV-Vis absorption spectroscopy (Figure 2(C)). The inset Tauc-plot shows a direct band gap of 3.34 eV. The absorption coefficient of the ZnO nanorods at a wavelength of 405 nm was determined to be 288 cm^{-1}, i.e. the laser light used for photocurrent excitation illuminates the entire depth of the film. Defects caused by oxygen vacancies in the oxygen deficient regions were confirmed with an

O 1s peak at 531.3 eV in XPS. Figure 4.2(D) shows a high-resolution O 1s XPS spectrum of ZnO nanorods, where O1 (530.2 eV), O2 (531.3 eV), and O3 (532.3 eV) are identified as O^{2-} in the crystal lattice, O^{-} or O^{2-} in oxygen deficient regions caused by oxygen vacancies, and adsorbed oxygen on the surface. The atom percentage of O1, O2, and O3 are 48.07%, 33.50%, and 18.43%, respectively [294].

4.3.2 Linear sweep voltammetry at ZnO nanorods

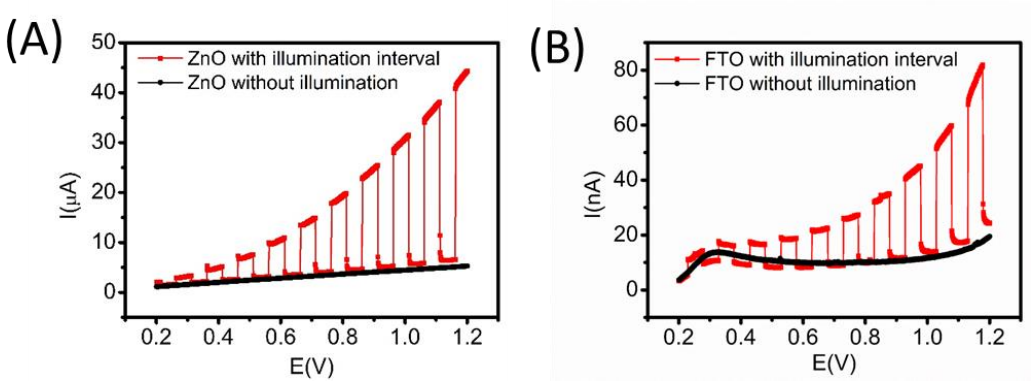

Figure 4.3 Linear sweep voltammetry of ZnO nanorods on (A) FTO coated glass, (B) bare FTO with chopped illumination. Bare FTO shows a photocurrent at nA level that is negligible when compared to ZnO nanorods.

ZnO nanorods on FTO-coated glass substrates displayed significant photocurrents in linear sweep voltammetry (LSV) with chopped 405 nm diode laser illumination at anodic potentials ≥ +0.2 V vs. Ag/AgCl (Figure 4.3(A)). The photo-induced anodic current under illumination increased with the applied bias, while the change of the dark current was negligible. To make certain that the photocurrent originated from the ZnO nanorods, LSV was carried out under the same conditions on a bare FTO-coated glass substrate (Figure 4.3(B)). The photocurrent in FTO was at nA level, which was 10^3 times smaller than the photocurrent in ZnO and can be neglected.

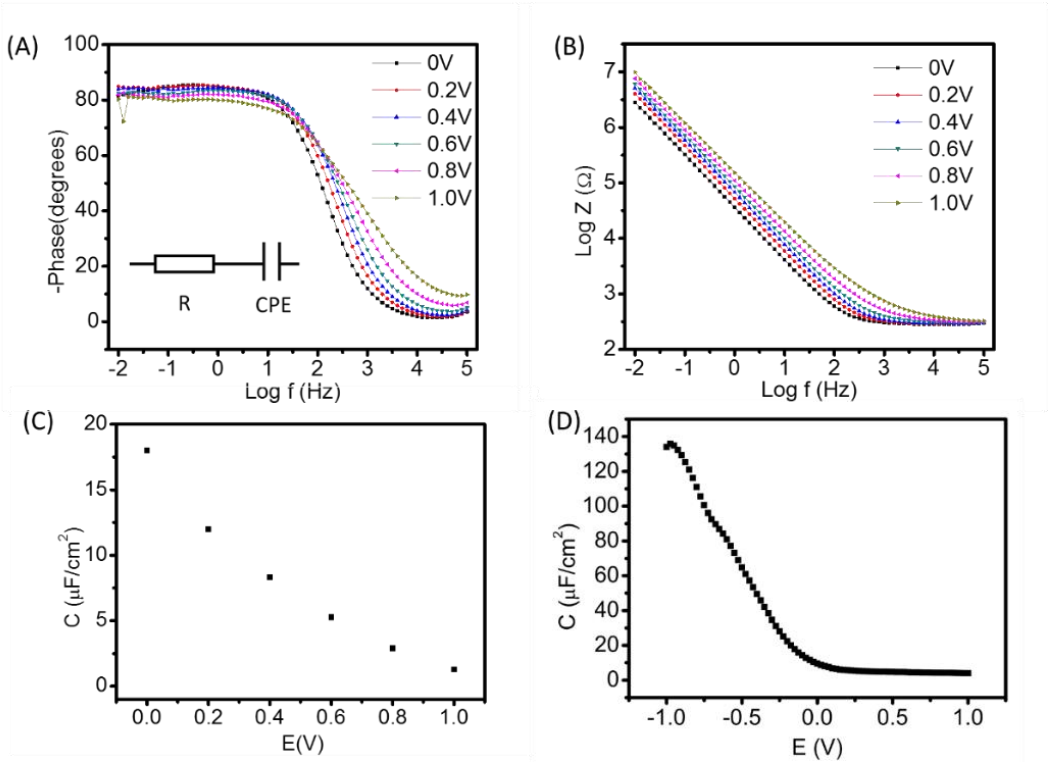

Figure 4.4 (A) - (B) Bode plots of ZnO nanorods in 10 mM pH 7.4 PBS buffer at zero bias, the equivalent circuit inset comprises a serial combination of the solution resistance (R) and a constant phase element (CPE), which represents the serial combination of depletion layer capacitance and double layer capacitance (18 μF/cm² for a circular surface area with 3 mm in diameter), (C) applied voltage dependency of capacitance, (D) capacitance derived from Mott-Schottky measurements over a greater voltage range.

An impedance spectrum of the ZnO nanorods in phosphate-buffered saline (PBS) was measured in the dark (Figure 4.4(A) and (B)). A capacitance of 18 μF/cm^2 in ZnO was obtained at zero bias, which was identified as the serial combination of the capacitances of the depletion layer and the electrical double layer. The capacitance decreased with increasing applied bias, as shown in Figure 4.4(C), which indicated that the depletion layer (C = 1.28 μF/cm^2 at 1 V) was dominant at high anodic voltages. Figure 4.4(D) displays the capacitance dependence over applied bias; the capacitance of ZnO nanorods decreases with increasing applied bias indicating that the depletion layer capacitance is dominant at high voltages.

4.3.3 LAPS and SPIM measurements

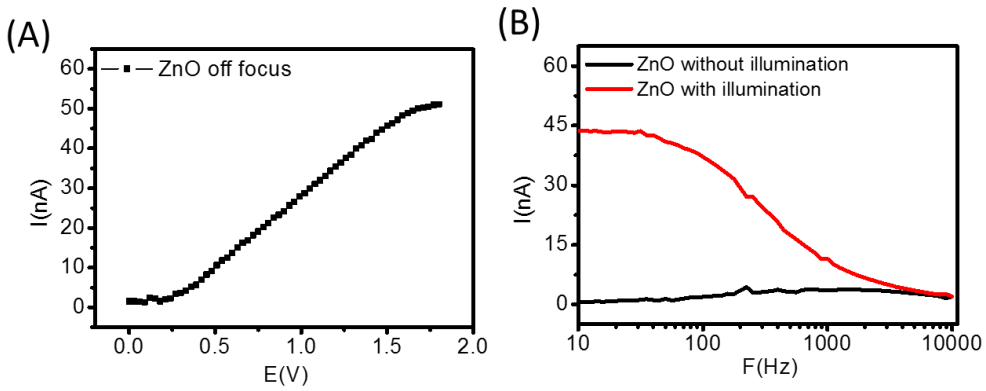

Figure 4.5 LAPS I-V curves of ZnO nanorods in pH 7.4 PBS buffer at 10 Hz with an unfocused laser beam (diameter of the light spot off focus 1.3 mm), (B) the frequency dependence of AC photocurrent and background AC current in the dark.

AC photocurrent-voltage (*I-V*) characteristics of ZnO nanorods (Figure 4.5(A)) were measured with an unfocused laser modulated at 10 Hz in pH 7.4 PBS using the LAPS setup shown in Figure 4.1. The photocurrent of ZnO nanorods increased with the applied bias and approached a plateau of 50 nA at 1.8 V. At higher voltages, the AC photocurrent could not be measured due to a large DC background current. Figure 4.5(B) shows the effect of the modulation frequency on the photocurrent at 1.5 V; both photocurrent and dark current were measured from 10 Hz to 10 kHz. The photocurrent significantly decreased at frequencies greater than 100 Hz due to the low mobility of minority charge carriers in ZnO, while the dark current, which is indicative of the noise level of the experimental setup, remained relatively constant. Consequently, the signal-to-noise ratio decreased with increasing frequency, and the photocurrent became unmeasurable at about 10 kHz. To ensure good sensitivity of local photocurrent measurements, a modulation frequency of 10 Hz and an applied bias of 1.5 V were selected for all LAPS measurements. The effect of the light intensity on

the photocurrent was also studied (Figure 4.6). At 1.5 V, the photocurrent increased with increasing light intensity. The photocurrent was 390 nA at maximum laser power. In this work, 10% of the maximum laser power (0.05 mW with an average power density of 3.8 mW/cm^2) was selected for LAPS measurements.

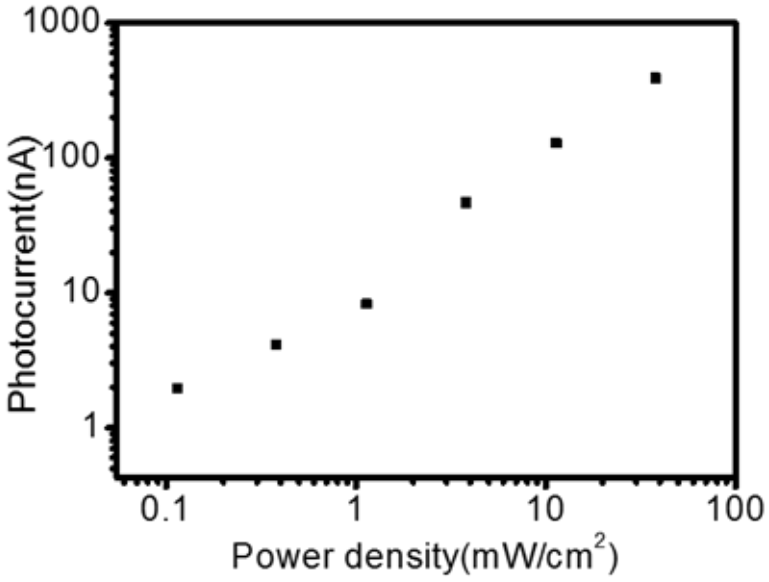

Figure 4.6 Light intensity dependency of the photocurrent. The photocurrent generated by ZnO increased with laser power. At 1.5 V, the photocurrent is 390 nA when the laser power reaches its maximum. In this study, 10% of the maximum power 3.8 mW/cm^2 (I_{photo} = 46. nA) was selected for LAPS measurements.

A photocurrent image can be measured by LAPS with a focused laser beam. To find the focus, the distance between sample and microscope objective on the Z axis was scanned in a 400 μm range while measuring the photocurrent (Figure 4.7(A)). In focus, the photocurrent reached a minimum as the electrode area for the photo-anodic process seen in the LSV measurements in Figure 4.3(A) was effectively reduced. Enhanced recombination of charge carriers and saturation of the photocurrent because of a low density of states with light energy close to the band edge are likely to have contributed

to the decrease of the photocurrent in focus as the power density is inversely proportional to the square of the laser spot diameter. The focused laser beam size was approximately 1 μm. The *I-V* curve in focus (Figure 4.7(B)) was shown to have a similar trend but a lower photocurrent compared to the one off focus (Figure 4.5(A)).

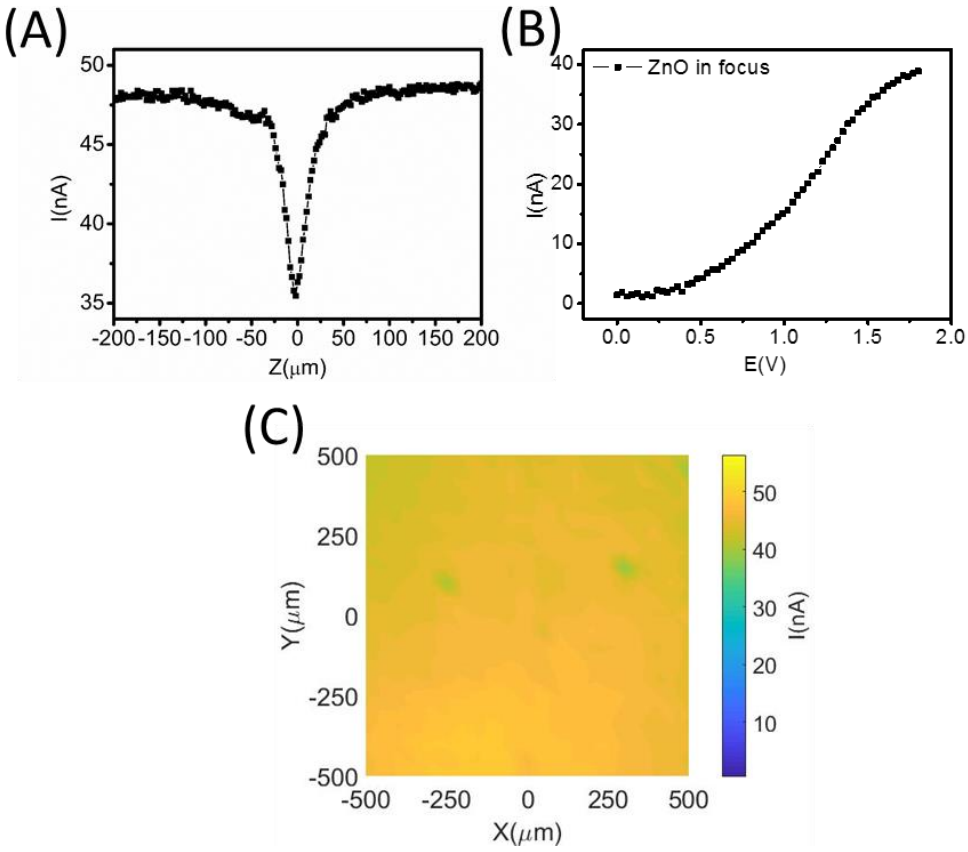

Figure 4.7 AC photocurrent measurements at ZnO nanorods at 10 Hz modulation frequency at 1.5 V: (A) Z-axis line scan of photocurrent around the focus, (B) LAPS I-V curve in focus, (C) photocurrent area scan.

An AC photocurrent image of a selected area of ZnO nanorods recorded by LAPS (Figure 4.7(C)) demonstrated a uniform photocurrent of 45.7 ± 0.1 nA with a focused laser beam at 10 Hz and an applied bias of 1.5 V. The background photocurrent image of bare FTO-coated glass was measured under the same conditions as shown in Figure 4.8, which shows a photocurrent of less than 0.3 nA, which was negligible.

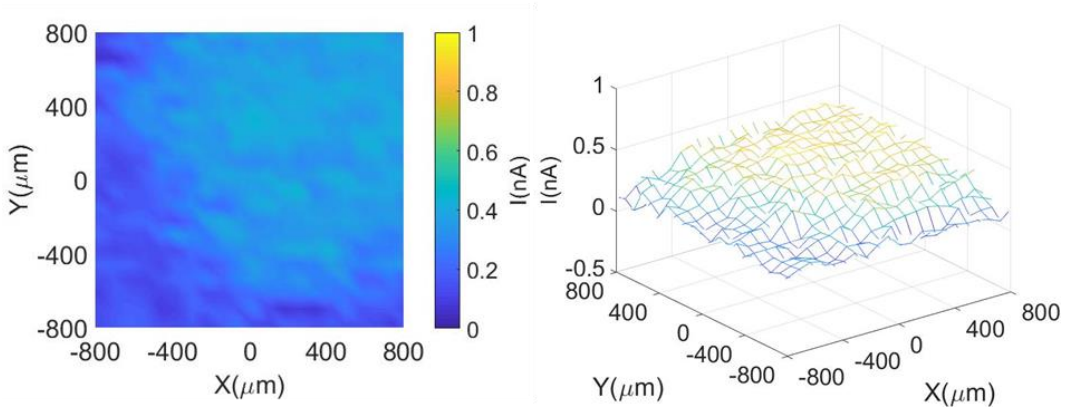

Figure 4.8 Photocurrent imaging of bare FTO by LAPS. The photocurrent of bare FTO (< 0.3 nA) is significantly lower than that of ZnO nanorods on FTO coated glass (45.7 ± 0.1 nA).

4.3.4 The effect of ZnO morphology on the device performance for LAPS imaging

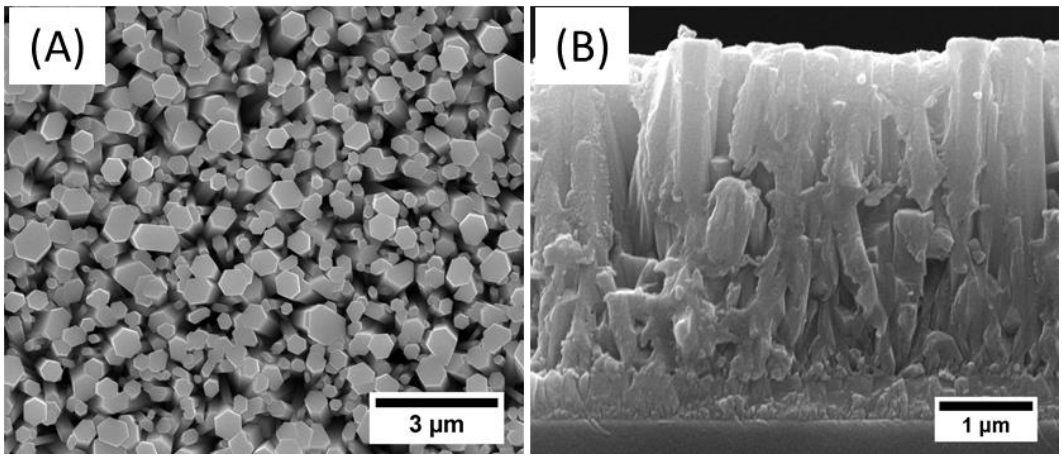

Figure 4.9 SEM images of the ZnO film (A) top view and (B) cross-section.

The device performance of ZnO for LAPS imaging was investigated using two different morphologies, ZnO nanorods (see Figure 4.2(A) and (B)) and a ZnO film with the same thickness grown at a higher concentration of the same precursor (Figure 4.9). In the film, ZnO formed columns with much larger diameters in a range of 0.3 to 0.9 μm, which were mostly fused together in a film-like structure as shown in the

cross-sectional view (Figure 4.9(B)) with some gaps still visible in the top view (Figure 4.9(A)).

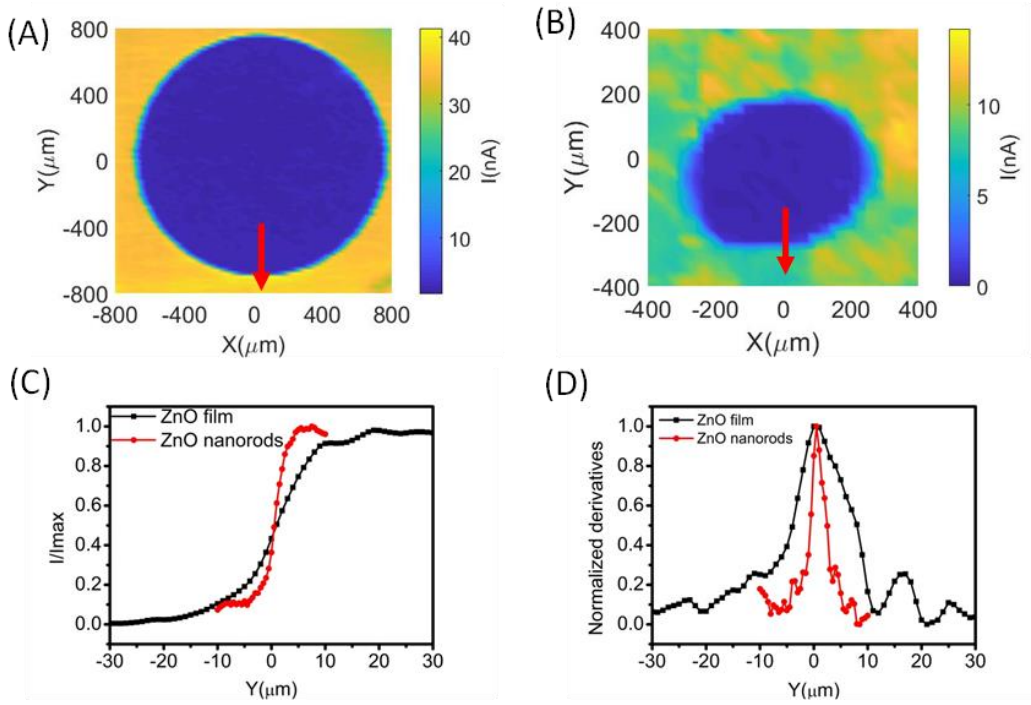

Figure 4.10 Photocurrent images of a PMMA dot on ZnO (A) nanorods and (B) film, in which the red arrows indicate the line scan direction; (C) Y-axis photocurrent line scans across the edge of the PMMA dots; (D) the first derivative of panel (C).

Figure 4.10(A) and (B) show photocurrent images with a PMMA dot on the surface of the ZnO for the nanorods and the film. The photocurrent measured on the uncoated areas of the ZnO was approximately five times larger on the nanorods (45.7 ± 0.1 nA) than on the film (9.2 ± 0.2 nA). This can be explained with the significantly larger specific surface area of the nanorods compared to that of the film and represents a considerable advantage of nanorods in this type of measurement. The area covered with PMMA shows a significantly lower photocurrent than the uncovered area for both ZnO morphologies. The photocurrent contrast was ascribed to the high impedance of the PMMA dot on the surface. To measure the lateral resolution,

photocurrent line scans with 500 nm step width across the edge of the PMMA dots were performed (Figure 4.10(C)). The lateral resolution calculated from the full width at half-maximum (FWHM) of the first derivative of the line scans (Figure 4.10 (D)) was 3.0 μm for the ZnO nanorods and 12 μm for the ZnO film. The diffusion length of minority charge carriers in bulk n-type ZnO typically assumes values of 130-440 nm [236], i.e. the lateral diffusion of charge carriers cannot be responsible for the difference in resolution between nanorods and film. As the features in the film are larger than the wavelength of light used for imaging, it is likely that light scattering is causing a significant degradation of the resolution. In contrast, the ZnO nanorods have diameters significantly smaller than the wavelength of light making light scattering effects negligible, thereby resulting in better lateral resolution. With a lateral resolution of 3.0 μm, this abundant metal oxide has great potential to be applied in biological imaging.

4.3.5 Sensor applications of ZnO nanorods

To assess the feasibility of using ZnO nanorods as a substrate for LAPS in practical applications, pH sensitivity was tested, and the possibility of using the new substrate in a biosensor format was investigated. Figure 4.11 displays the pH sensitivity of ZnO nanorods in a range of phosphate buffer solutions (pH 5-9) with 0.1 M KCl using an unfocused laser to illuminate a sample area of 1.3 mm in diameter. The *I-V* curve shifted towards higher potentials with decreasing pH, which is typical for an n-type semiconductor [227]. As there is no insulator present on the ZnO nanorods, the pH sensitivity could originate from the surface potential as in classical LAPS, but could also be affected by the anodic process (see Figure 4.3(A)), which can be ascribed to the oxidation of OH^-, and would, therefore, not be expected to follow the Nernst

equation. At a consta nt photocurrent of 40 nA, ZnO was observed to have an average sensitivity of 53 mV/pH by linear fitting with R-square of 0.96 (inset Figure 4.11). This shows ZnO to be a promising sensing material for a pH imaging sensor as well as the potential for other biochemical characterization with LAPS.

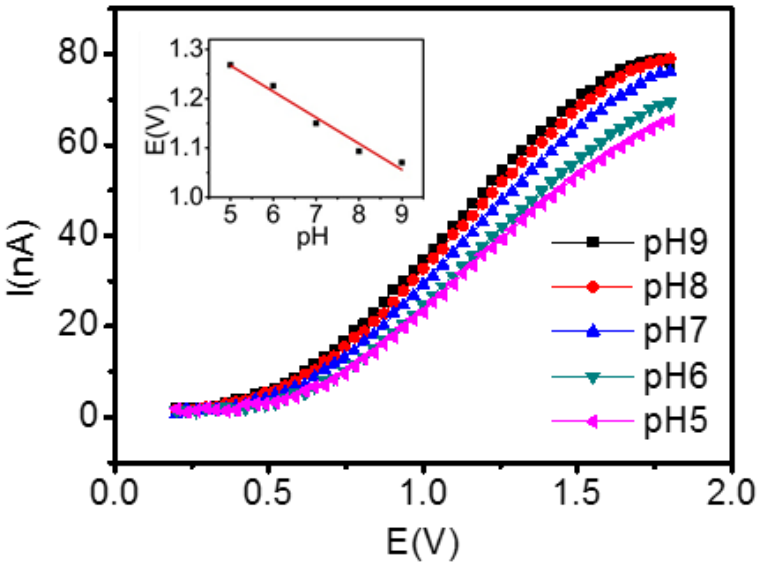

Figure 4.11 LAPS I-V curves of ZnO nanorods in different pH solutions, inset is the pH sensitivity.

Previous research has developed biosensors for the detection of enzyme activities based on the degradation of thin polymer films. Degradation of the polymer films has been monitored by using techniques such as surface plasmon resonance (SPR) [293], [295], quartz crystal microbalance (QCM) [296], [297], impedance measurements and SPIM [219], [296], [298]–[300]. In this work, a poly(ester amide) for the detection of α-chymotrypsin was deposited onto the ZnO nanorods by drop-coating 1 µL of poly(ester amide) (200 mg/ml in chloroform). The polymer dot on the ZnO nanorods substrate is clearly visible in the photocurrent image in Figure 4.12(A) and the corresponding phase image in Figure 4.12(B). As the phase between photocurrent and light intensity proved to be more stable than the photocurrent, the polymer degradation

was monitored by recording phase images (Figure 4.12(C)-(F)). The area of the film decreased with time; approximately 60% of the polymer had been degraded after 2 h, and the polymer completely disappeared after 6 h.

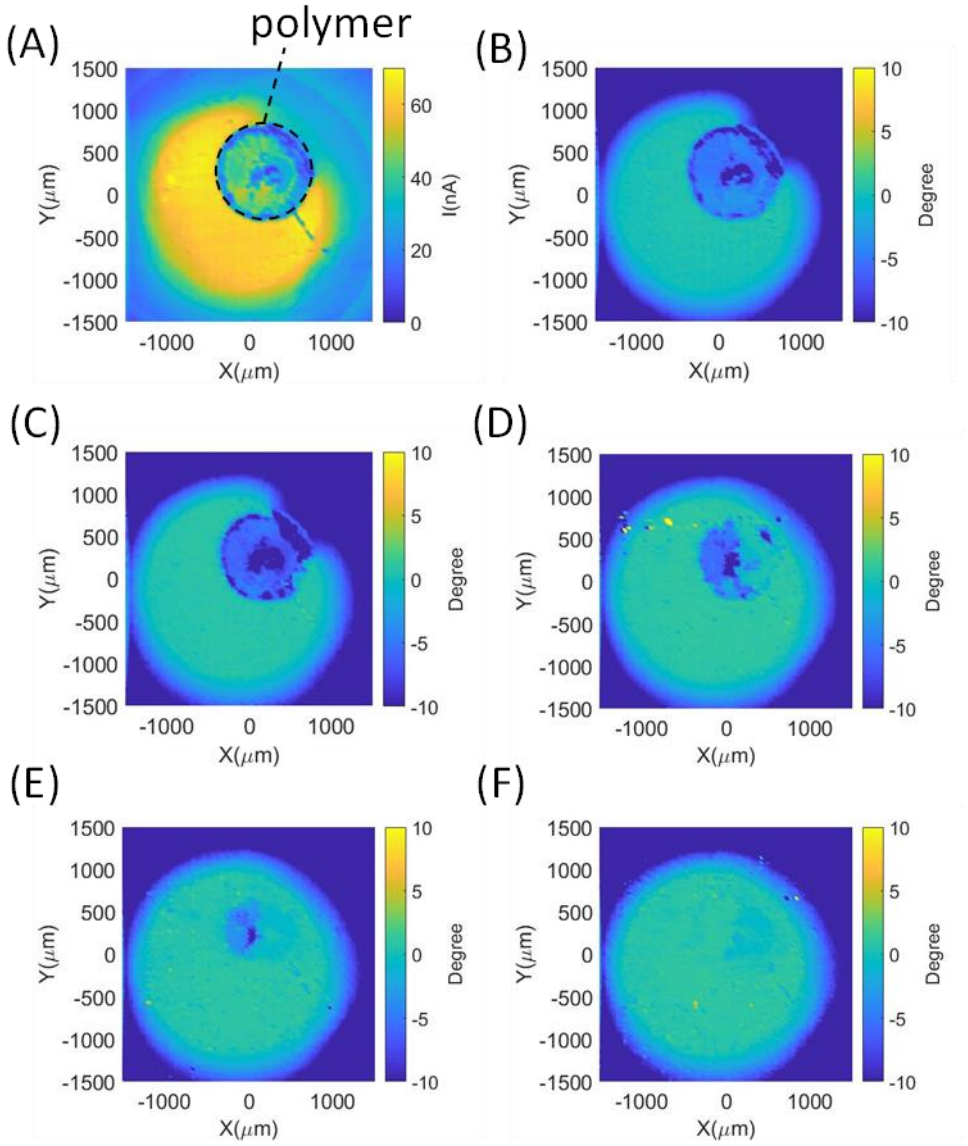

Figure 4.12 (A) Photocurrent image and (B) phase image of poly(ester amide) on ZnO nanorods in pH 7.3 buffer. Phase images taken at (C) 0 h, (D) 2 h, (E) 4 h and (F) 6 h after adding 100 μM α-chymotrypsin into pH 7.3 buffer solution.

The area of the polymer dot in the phase images was calculated using ImageJ and plotted versus time (Figure 4.13). With the assumption that the polymer was uniform on the ZnO nanorods, the average degradation rate of the poly(ester amide) was

estimated to be 29 µg/h in the presence of 100 µM α-chymotrypsin. This demonstrates the suitability of LAPS imaging using ZnO nanorods for the interrogation of biosensor arrays and for real-time imaging of biological processes. The low cost of ZnO and an easily scalable solution deposition technique make this a promising substrate for disposable biosensors.

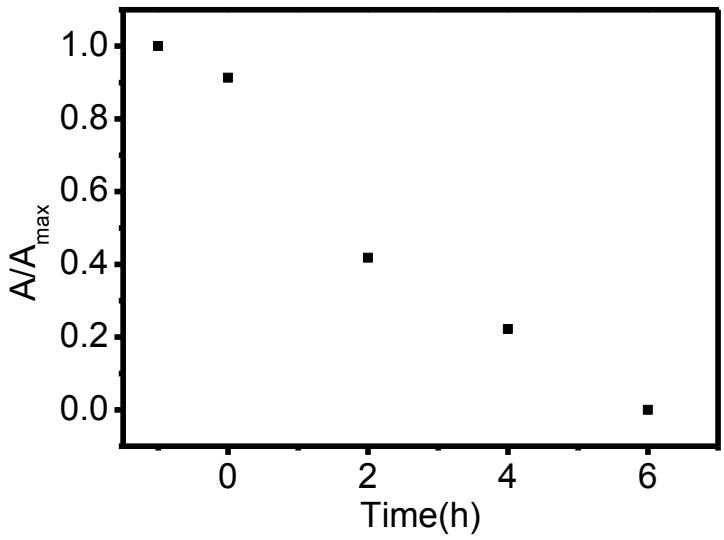

Figure 4.13 Area of poly(ester amide) degradation by 100 µM α-chymotrypsin. The enzyme was added at t=0.

4.3.6 CVD ZnO film in LAPS

Given the successful use of ZnO nanorods in LAPS, the use of 1D nanostructures has been widely broadened. However, the drawback of ZnO nanorods is the rough surface that is unsuitable for cell cultures [301], which limits its use in bioimaging application such as the investigation of metabolic and signalling events in living cells. Therefore, ZnO with a flat surface is essential to supply a proper environment for living cells. A ZnO film produced by CVD method was investigated, here it is labelled as 'CVD-ZnO'.

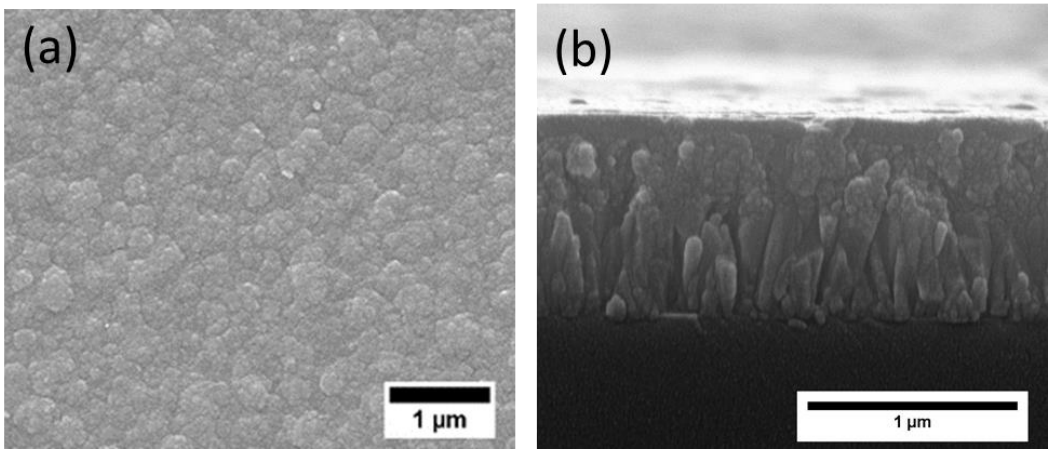

Figure 4.14 Top-view SEM image of CVD-ZnO, top-view (a), cross-sectional view (b).

Figure 4.14 shows the morphology of CVD-ZnO; it was a compact film and the surface was more compact than the film made by solution method as shown in Figure 4.9(A). The thickness of the CVD-ZnO film was 1 µm (Figure 4.14(b)), and it can be controlled easily by changing the deposition time. A photocurrent image with a PMMA dot on CVD-ZnO is displayed in Figure 4.15(A); the photocurrent in the area without PMMA was smaller in the CVD-ZnO film than in the nanorods. This is ascribed to the significantly larger surface area of the nanorods than the film, which generates more free carriers. Table 4.1 summaries the maximum photocurrent and spatial resolution of ZnO in different morphologies.

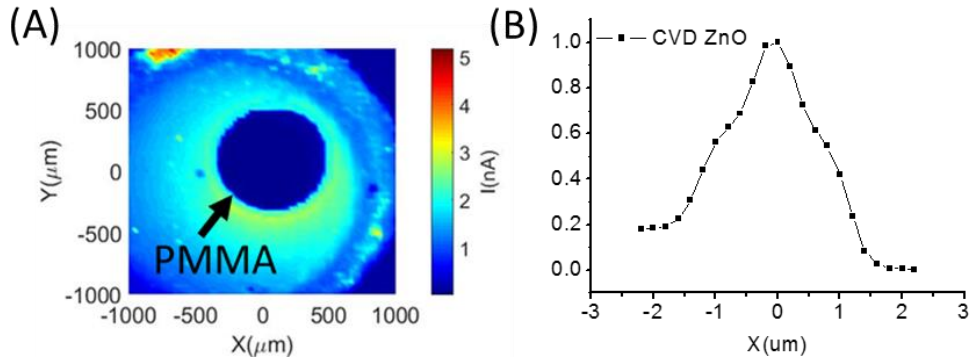

Figure 4.15 (A) Photocurrent image of a PMMA dot on CVD ZnO, (B) the first derivative of photocurrent line scan across the edge of the PMMA dot.

However, the spatial resolution calculated from the FWHM of the peaks in Figure 4.15 (B) and Figure 4.10(D) did not show the same trend as the photocurrents, as the resolution of CVD-ZnO was approximately 6 times better than that of the film. As described in section 4.3.4, light scattering effects had adversely affected the resolution obtained with the film, while light scattering was negligible for the CVD-ZnO film.

Table 4.1 Maximum photocurrent and spatial resolution of ZnO in different morphologies.

	ZnO nanorods	**ZnO film**	**CVD-ZnO**
Maximum photocurrent (nA)	45.7 ± 0.1	9.2 ± 0.2	2.8 ± 0.2
Spatial resolution (μm)	3.0	11.9	2.0

4.4 Summary

ZnO nanorods synthesized using a simple aqueous solution method on FTO-coated glass were found to be uniform and well-oriented in the c-axis with a high aspect ratio of 51. The nanostructured semiconductor was shown to be suitable for photocurrent imaging with LAPS without the need for an insulator. Photocurrent images of a PMMA dot deposited on ZnO nanorods, ZnO films and CVD-ZnO showed that the

1D substrate is suitable for LAPS photocurrent images. ZnO nanorods have the advantage of higher photocurrents and better resolution than a film of the same thickness. Resolution of 2.0 μm of CVD-ZnO was achieved due to negligible light scattering effects. ZnO nanorods displayed a pH sensitivity of 53 mV/pH in a pH range from 5-9 and were shown to be suitable for use in a biosensor format aimed at the detection of enzymes by monitoring the degradation a polymer film. The sensor showed sufficient stability for monitoring the polymer degradation over 6 h. The large photocurrents paired with good lateral resolution and pH sensitivity make ZnO nanorods a promising sensor substrate for biosensing and bioimaging applications. The successful demonstration of the suitability of nanostructured semiconductors without an insulator as substrates for LAPS greatly expands the range semiconductor materials that can be used in this imaging technique, making it more attractive for general use.

5 Conclusions and future work

5.1 Conclusions

In this thesis, chemical and biological sensors were successfully applied to ammonia gas detection and LAPS based on ZnO nanorods.

The work started from the synthesis and characterization of ZnO nanorods. A new method – a single step synthesis of ZnO nanorods with high aspect ratio (51) – was introduced. In contrast to the traditional method by refreshing the precursor solution after a certain time, the as-achieved nanorods using a single step showed no significant difference in electric and optical properties. It was found that the annealing atmosphere affacted the electron concentration and oxygen vacancy content in ZnO. The carrier concentration of the ZnO nanorods and the rectification ratio in ZnO/PEDOT:PSS diodes increased with the decreasing oxygen partial pressure during annealing. The first part of this thesis clearly demonstrated that high aspect ratio ZnO nanorods can be produced in an easy way with low cost, and that nitrogen annealing of ZnO nanorods offers an alternative way to improve the diode performance of this system.

To decrease the operating temperatures of current metal oxide semiconductor gas sensors, a ZnO/Au Schottky diode was produced using a simple method by depositing a gold layer on the as-achieved ZnO nanorods. The gold was shown to form a film on the top and nanoparticles in the centre of the nanorods. At room temperature, the ZnO/Au Schottky diode had responsivity of 27.3% towards 20 ppm ammonia gas and a promising selectivity compared to common gases such as acetone, carbon monoxide, and ethanol. The room temperature response of the ZnO/Au Schottky diode to ammonia was shown to be stable over 40 days. The successful demonstration of

Schottky diodes made with ZnO nanorods and gold gives an alternative and simple way to decrease the operating temperature of MOS gas sensors, and the reduced power consumption makes it possible to be integrated with battery-powered wireless devices.

1D nanostructured semiconducting oxide – ZnO was successfully used for the first time in photocurrent imaging with LAPS without the need of an insulator. ZnO nanorods were shown to be suitable for use in bioanalytical application such as a biosensor format aimed at the detection of enzymes by monitoring the degradation a polymer film. Semiconductor morphology was found to have an effect on the spatial resolution of LAPS. Resolution measured on the same thickness of ZnO was four times larger in a film (12.0 μm) than in nanorods (3.0 μm), which this is likely due to the light scattering effect with a 405 nm diode laser. The large photocurrents (45.7 ± 0.1 nA) paired with good lateral resolution and pH sensitivity (53 mV/pH) make ZnO nanorods a promising sensor substrate for biosensing and imaging applications. The successful demonstration of the suitability of nanostructured semiconductors without an insulator as substrates for LAPS greatly expands the range semiconductor materials that can be used in this imaging technique, making it more attractive for general use.

Overall, ZnO nanorods with the advantage of easy synthesis and low cost was proved to be a promising semiconductor in the application of gas sensors and LAPS.

5.2 Future work

There remains a lot of work to do to continue this project. Suggestions can be made in the following aspects.

ZnO nanorods synthesis

In this project, ZnO in the form of nanorods was produced, it is of interest to synthesize different ZnO morphologies using low cost method such as solution phase synthesis. Although some conditions have been studied to achieve high aspect ratio, the effect of those conditions on the crystal structure, defects level or impurity concentration would be helpful to understand the formation of ZnO. To tailor ZnO according to specific demands in size and structure is also essential to meet the fast-growing requirements in nanomaterials based devices.

Gas sensors

The ZnO/Au Schottky diode gas sensor described in this project has great space for improvement. Miniaturizing the device would be the first choice because large size device would have more defects and more recombination sites. To increase the gas exchange on the ZnO nanorod surface would increase the sensitivity and also response and recovery time, a porous gold electrode would be an option. The porous gold layer is easy to produce with the assistant of polystyrene beads that can be removed by a simple thermal treatment. Apart from the suggestions to improve the sensing properties, there remain some fundamental studies:

- The effect of humidity on the sensitivity to ammonia gas at room temperature
- Gas sensing behaviour at ammonia concentration lower than 1 ppm
- The function of gold nanoparticles on selectivity to ammonia gas, by comparing the sensing properties of ZnO based Schottky diodes without gold nanoparticles involved

LAPS

Although ZnO nanorods show large photocurrent, the stability of the ZnO nanorods under illumination of a focused light with a bias is a problem. The photodegradation of ZnO nanorods will be a limitation for it to be used as a real time imaging substrate in LAPS. To solve this problem, the first thing is to understand the mechanism of the photodegradation of ZnO. The reduction of surface state in ZnO under illumination with a bias could be one of the reasons. Surface modification can be used to passivate the chemical reduction on ZnO surface.

6 References

[1] Y. Fu, Y. Nie, Y. Zhao, P. Wang, L. Xing, Y. Zhang, and X. Xue, "Detecting Liquefied Petroleum Gas (LPG) at Room Temperature Using $ZnSnO_3$/ZnO Nanowire Piezo-Nanogenerator as Self-Powered Gas Sensor," *ACS Appl. Mater. Interfaces*, **2015**, 7, 10482.

[2] I. Jiménez, J. Arbiol, G. Dezanneau, A. Cornet, and J. R. Morante, "Crystalline structure, defects and gas sensor response to NO_2 and H_2S of tungsten trioxide nanopowders," in *Sensors and Actuators, B: Chemical*, **2003,** 93, 475.

[3] S. Park, S. Kim, G.-J. Sun, and C. Lee, "Synthesis, Structure, and Ethanol Gas Sensing Properties of In_2O_3 Nanorods Decorated with Bi_2O_3 Nanoparticles," *ACS Appl. Mater. Interfaces*, **2015**, 7, 8138.

[4] S. K. Arya, S. Saha, J. E. Ramirez-Vick, V. Gupta, S. Bhansali, and S. P. Singh, "Recent advances in ZnO nanostructures and thin films for biosensor applications: Review," *Anal. Chim. Acta*, **2012**, 737, 1.

[5] C. X. Xu, C. Yang, B. X. Gu, and S. J. Fang, "Nanostructured ZnO for biosensing applications," *Chinese Sci. Bull.*, **2013**, 58, 2563.

[6] N. Yamazoe, G. Sakai, and K. Shimanoe, "Oxide semiconductor gas sensors," *Catal. Surv. from Asia*, **2003**, 7, 63.

[7] J. C. Owicki, L. J. Bousse, D. G. Hafeman, G. L. Kirk, J. D. Olson, H. G. Wada, and J. W. Parce, "The Light-Addressable Potentiometric Sensor: Principles and Biological Applications," *Annu. Rev. Biophys. Biomol. Struct.*, **1994**, 23, 87.

[8] T. Yoshinobu, K. Miyamoto, C. F. Werner, A. Poghossian, T. Wagner, and M. J. Schöning, "Light-Addressable Potentiometric Sensors for Quantitative Spatial Imaging of Chemical Species," *Annu. Rev. Anal. Chem.*, **2017**, 10, 225.

[9] F. Wu, I. Campos, D.-W. Zhang, and S. Krause, "Biological imaging using light-addressable potentiometric sensors and scanning photo-induced impedance microscopy," *Proc. R. Soc. A Math. Phys. Eng. Sci.*, **2017**, 473, 1.

[10] L. Schmidt-Mende and J. L. MacManus-Driscoll, "ZnO – nanostructures, defects, and devices," *Mater. Today*, **2007**, 10, 40.

[11] Z. L. Wang, "Nanostructures of zinc oxide," *Mater. Today*, **2004**, 7, 26.

[12] Z. L. Wang, "Zinc oxide nanostructures: growth, properties and applications," *J. Phys. Condens. Matter*, **2004**, 16, R829.

[13] J. Briscoe and S. Dunn, "Piezoelectric nanogenerators – a review of nanostructured piezoelectric energy harvesters," *Nano Energy*, **2015**, 14, 15.

[14] B. Kumar and S.-W. Kim, "Energy harvesting based on semiconducting piezoelectric ZnO nanostructures," *Nano Energy*, **2012**, 1, 342.

[15] J. Briscoe, N. Jalali, P. Woolliams, M. Stewart, P. M. Weaver, M. Cain, and S. Dunn, "Measurement techniques for piezoelectric nanogenerators," *Energy Environ. Sci.*, **2013**, 6, 3035.

[16] Wang, Zhong Lin and J. Song, "Piezoelectric Nanogenerators Based on Zinc Oxide Nanowire Arrays," *Science (80-.).*, **2006**, 312, 242.

[17] X. Y. Kong and Z. L. Wang, "Spontaneous Polarization-Induced Nanohelixes, Nanosprings, and Nanorings of Piezoelectric Nanobelts," *Nano Lett.*, **2003**, 3, 1625.

[18] S. M. Hatch, J. Briscoe, and S. Dunn, "A Self-Powered ZnO-Nanorod/CuSCN UV Photodetector Exhibiting Rapid Response," *Adv. Mater.*, **2013**, 25, 867.

[19] S. K. Shaikh, V. V Ganbavle, S. I. Inamdar, and K. Y. Rajpure, "Multifunctional zinc oxide thin films for high-performance UV photodetectors and nitrogen dioxide gas sensors," *RSC Adv.*, **2016**, 6, 25641.

[20] R. Khokhra, B. Bharti, H.-N. Lee, and R. Kumar, "Visible and UV photo-detection in ZnO nanostructured thin films via simple tuning of solution method," *Sci. Rep.*, **2017**, 7, 15032.

[21] Y. Jin, J. Wang, B. Sun, J. C. Blakesley, and N. C. Greenham, "Solution-Processed Ultraviolet Photodetectors Based on Colloidal ZnO Nanoparticles," *Nano Lett.*, **2008**, 8, 1649.

[22] M. L. Lee, P.-F. Chi, and J. K. Sheu, "Photodetectors formed by an indium tin oxide/zinc oxide/p-type gallium nitride heterojunction with high ultraviolet-to-visible rejection ratio," *Appl. Phys. Lett.*, **2009**, 94, 013512.

[23] A. Tsukazaki, A. Ohtomo, T. Onuma, M. Ohtani, T. Makino, M. Sumiya, K. Ohtani, S. F. Chichibu, S. Fuke, Y. Segawa, H. Ohno, H. Koinuma, and M. Kawasaki, "Repeated temperature modulation epitaxy for p-type doping and light-emitting diode based on ZnO," *Nat. Mater.*, **2004**, 4, 42.

[24] J. H. Lim, C. K. Kong, K. K. Kim, I. K. Park, D. K. Hwang, and S. J. Park, "UV electroluminescence emission from ZnO light-emitting diodes grown by high-temperature radiofrequency sputtering," *Adv. Mater.*, **2006**, 18, 2720.

[25] D. K. Hwang, M. S. Oh, J. H. Lim, Y. S. Choi, and S. J. Park, "ZnO-based light-emitting metal-insulator-semiconductor diodes," *Appl. Phys. Lett.*, **2007**, 91.

[26] Y. Yang, X. W. Sun, B. K. Tay, G. F. You, S. T. Tan, and K. L. Teo, "A p-n homojunction ZnO nanorod light-emitting diode formed by As ion implantation," *Appl. Phys. Lett.*, **2008**, 93.

[27] O. Lupan, T. Pauporté, and B. Viana, "Low-voltage UV-electroluminescence from ZnO-Nanowire array/p-CaN light-emitting diodes," *Adv. Mater.*, **2010**, 22, 3298.

[28] H. Sun, Q. Zhang, J. Zhang, T. Deng, and J. Wu, "Electroluminescence from ZnO nanowires with a p-ZnO film/n-ZnO nanowire homojunction," *Appl. Phys. B Lasers Opt.*, **2008**, 90, 543.

[29] Y. T. Kim, J. Park, S. Kim, D. W. Park, and J. Choi, "Fabrication of hierarchical ZnO nanostructures for dye-sensitized solar cells," *Electrochim. Acta*, **2012**, 78, 417.

[30] Q. Zhang, C. S. Dandeneau, X. Zhou, and G. Cao, "ZnO Nanostructures for Dye-Sensitized Solar Cells," *Adv. Mater.*, **2009**, 21, 4087.

[31] L. Loh, J. Briscoe, and S. Dunn, "Bismuth Ferrite Enhanced ZnO Solid State Dye-sensitised Solar Cell," in *Procedia Engineering*, **2016**, 139, 15.

[32] J. Briscoe, D. E. Gallardo, S. Hatch, V. Lesnyak, N. Gaponik, and S. Dunn, "Enhanced quantum dot deposition on ZnO nanorods for photovoltaics through

layer-by-layer processing," *J. Mater. Chem.*, **2011**, 21, 2517.

[33] D. Bi, G. Boschloo, S. Schwarzmüller, L. Yang, E. M. J. Johansson, and A. Hagfeldt, "Efficient and stable $CH_3NH_3PbI_3$-sensitized ZnO nanorod array solid-state solar cells," *Nanoscale*, **2013**, 5, 11686.

[34] D. S. Cells, A. K. Chandiran, M. Abdi-jalebi, M. K. Nazeeruddin, and M. Gra, "Analysis of Electron Transfer Properties of ZnO and TiO_2 Photoanodes for Dye-Sensitized Solar Cells," *ACS Nano*, **2014**.

[35] R. Velmurugan and M. Swaminathan, "An efficient nanostructured ZnO for dye sensitized degradation of Reactive Red 120 dye under solar light," *Sol. Energy Mater. Sol. Cells*, **2011**, 95, 942.

[36] R. Zhang, J. Pan, E. P. Briggs, M. Thrash, and L. L. Kerr, "Studies on the adsorption of RuN_3 dye on sheet-like nanostructured porous ZnO films," *Sol. Energy Mater. Sol. Cells*, **2008**, 92, 425.

[37] Q. F. Zhang, C. S. Dandeneau, X. Y. Zhou, and G. Z. Cao, "ZnO Nanostructures for Dye-Sensitized Solar Cells," *Adv. Mater.*, **2009**, 21, 4087.

[38] S. Pace, A. Resmini, I. G. Tredici, A. Soffientini, X. Li, S. Dunn, J. Briscoe, and U. Anselmi-Tamburini, "Optimization of 3D ZnO brush-like nanorods for dye-sensitized solar cells," *RSC Adv.*, **2018**, 8, 9775.

[39] A. H. Zahmani and A. Sandhu, "Hybrid AlGaN/GaN-ZnO-Nanowire Gas Sensors," *J. Nanosci. Nanotechnol.*, **2011**, 11, 3938.

[40] M. W. Ahn, K. S. Park, J. H. Heo, D. W. Kim, K. J. Choi, and J. G. Park, "On-chip fabrication of ZnO-nanowire gas sensor with high gas sensitivity," *Sensors Actuators, B Chem.*, **2009**, 138, 168.

[41] M. W. Ahn, K. S. Park, J. H. Heo, J. G. Park, D. W. Kim, K. J. Choi, J. H. Lee, and S. H. Hong, "Gas sensing properties of defect-controlled ZnO-nanowire gas sensor," *Appl. Phys. Lett.*, **2008**, 93.

[42] A. Mirzaei, S. Park, H. Kheel, G. J. Sun, S. Lee, and C. Lee, "ZnO-capped nanorod gas sensors," *Ceram. Int.*, **2016**, 42, 6187.

[43] V. Galstyan, E. Comini, C. Baratto, G. Faglia, and G. Sberveglieri, "Nanostructured ZnO chemical gas sensors," *Ceram. Int.*, **2015**, 41, 14239.

[44] L. H. Zhao, R. Zhang, J. Zhang, and S. Q. Sun, "Synthesis and characterization of biocompatible ZnO nanoparticles," *CrystEngComm*, **2012**, 14, 945.

[45] R. Hong, T. Pan, J. Qian, and H. Li, "Synthesis and surface modification of ZnO nanoparticles," *Chem. Eng. J.*, **2006**, 119, 71.

[46] H. Kumar and R. Rani, "Structural and Optical Characterization of ZnO Nanoparticles Synthesized by Microemulsion Route," *Int. Lett. Chem. Phys. Astron.*, **2013**, 19, 26.

[47] D. Lin and B. Xing, "Root uptake and phytotoxicity of ZnO nanoparticles," *Environ. Sci. Technol.*, **2008**, 42, 5580.

[48] J. Song and S. Lim, "Effect of Seed Layer on the Growth of ZnO Nanorods," *J. Phys. Chem. C*, **2007**, 111, 596.

[49] E. Sönmez and K. Meral, "Enhancement of photoluminescence lifetime of ZnO nanorods making use of Thiourea," *J. Nanomater.*, **2012**, 2012.

[50] M. Law, L. E. Greene, J. C. Johnson, Saykally.Richard, and P. Yang, "Nanowires dye-sensitized solar cells," *Nat. Mater.*, **2005**, 4, 455.

[51] D. J. Gargas, H. Gao, H. Wang, and P. Yang, "Supporting Information High Quantum Efficiency of Band-Edge Emission from ZnO Nanowires," *Nano Lett.*, **2011**, 11, 3792.

[52] L. E. Greene, B. D. Yuhas, M. Law, D. O. Zitoun, and P. Yang, "Solution-grown zinc oxide nanowires.," *Inorg. Chem.*, **2006**, 45, 7535.

[53] H. J. Xiang, J. Yang, J. G. Hou, and Q. Zhu, "Piezoelectricity in ZnO nanowires: A first-principles study," *Appl. Phys. Lett.*, **2006**, 89, 223111.

[54] S. Y. Bae, H. W. Seo, and J. Park, "Vertically Aligned Sulfur-Doped ZnO Nanowires Synthesized via Chemical Vapor Deposition," *J. Phys. Chem. B*, **2004**, 108, 5206.

[55] J. Suehiro, N. Nakagawa, S. I. Hidaka, M. Ueda, K. Imasaka, M. Higashihata, T. Okada, and M. Hara, "Dielectrophoretic fabrication and characterization of a ZnO nanowire-based UV photosensor," *Nanotechnology*, **2006**, 17, 2567.

[56] J. Miao and B. Liu, "Semiconductor Nanowires," *Semicond. Nanowires*, **2015**, 3.

[57] Y. X. Chen and S. W. Guo, "Twinning-induced ZnO bicrystalline nanobelts," *Mater. Lett.*, **2007**, 61, 5275.

[58] R. Q. Song, A. W. Xu, B. Deng, Q. Li, and G. Y. Chen, "From layered basic zinc acetate nanobelts to hierarchical zinc oxide nanostructures and porous zinc oxide nanobelts," *Adv. Funct. Mater.*, **2007**, 17, 296.

[59] R. Yousefi and B. Kamaluddin, "Effect of S- and Sn-doping to the optical properties of ZnO nanobelts," *Appl. Surf. Sci.*, **2009**, 255, 9376.

[60] J. Il Hong, J. Choi, S. S. Jang, J. Gu, Y. Chang, G. Wortman, R. L. Snyder, and Z. L. Wang, "Magnetism in dopant-free ZnO nanoplates," *Nano Lett.*, **2012**, 12, 576.

[61] J. Zhang, X. Liu, S. Wu, B. Cao, and S. Zheng, "One-pot synthesis of Au-supported ZnO nanoplates with enhanced gas sensor performance," *Sensors Actuators, B Chem.*, **2012**, 169, 61.

[62] Y. Chen, L. Wang, W. Wang, and M. Cao, "Synthesis of Se-doped ZnO nanoplates with enhanced photoelectrochemical and photocatalytic properties," *Mater. Chem. Phys.*, **2017**, 199, 416.

[63] H. Wang, G. Li, L. Jia, G. Wang, and C. Tang, "Controllable preferential-etching synthesis and photocatalytic activity of porous ZnO nanotubes," *J. Phys. Chem. C*, **2008**, 112, 11738.

[64] J. Q. Hu, Q. Li, X. M. Meng, C. S. Lee, and S. T. Lee, "Thermal reduction route to the fabrication of coaxial Zn/ZnO nanocables and ZnO nanotubes," *Chem. Mater.*, **2003**, 15, 305.

[65] Y. J. Xing, Z. H. Xi, Z. Q. Xue, X. D. Zhang, J. H. Song, R. M. Wang, J. Xu, Y. Song, S. L. Zhang, and D. P. Yu, "Optical properties of the ZnO nanotubes synthesized via vapor phase growth," *Appl. Phys. Lett.*, **2003**, 83, 1689.

[66] D. Barreca, D. Bekermann, E. Comini, A. Devi, R. A. Fischer, A. Gasparotto,

C. MacCato, C. Sada, G. Sberveglieri, and E. Tondello, “Urchin-like ZnO nanorod arrays for gas sensing applications,” *CrystEngComm*, **2010**, 12.

[67] P. Yang, H. Yan, S. Mao, R. Russo, J. Johnson, R. Saykally, N. Morris, J. Pham, R. He, and H.-J. Choi, “Controlled Growth of ZnO Nanowires and Their Optical Properties,” *Adv. Funct. Mater.*, **2002**, 12, 323.

[68] B. Xiang, P. Wang, X. Zhang, S. A. Dayeh, D. P. R. Aplin, C. Soci, D. Yu, and D. Wang, “Rational Synthesis of p-Type Zinc Oxide Nanowire Arrays Using Simple Chemical Vapor Deposition,” *Nano Lett.*, **2007**, 7, 323.

[69] P. X. Gao, Y. Ding, and Z. L. Wang, “Crystallographic Orientation-Aligned ZnO Nanorods Grown by a Tin Catalyst,” *Nano Lett.*, **2003**, 3, 1315.

[70] J.-J. Wu and S.-C. Liu, “Catalyst-Free Growth and Characterization of ZnO Nanorods,” *J. Phys. Chem. B*, **2002**, 106, 9546.

[71] Wang, Song, P. Li, J. H. Ryou, R. D. Dupuis, C. J. Summers, and Z. L. Wang, “Growth of Uniformly Aligned ZnO Nanowire Heterojunction Arrays on GaN, AlN, and $Al_{0.5}Ga_{0.5}N$ Substrates,” *J. Am. Chem. Soc.*, **2005**, 127, 7920.

[72] X. Wang, C. J. Summers, and Z. L. Wang, “Large-Scale Hexagonal-Patterned Growth of Aligned ZnO Nanorods for Nano-optoelectronics and Nanosensor Arrays,” *Nano Lett.*, **2004**, 4, 423.

[73] R. S. Wagner and W. C. Ellis, “VAPOR-LIQUID-SOLID MECHANISM OF SINGLE CRYSTAL GROWTH,” *Appl. Phys. Lett.*, **1964**, 4, 89.

[74] X. Meng, B. Lin, B. Gu, J. Zhu, and Z. Fu, “A simple growth route towards ZnO thin films and nanorods,” *Solid State Commun.*, **2005**, 135, 411.

[75] J.-L. Zhao, X.-M. Li, J.-M. Bian, W.-D. Yu, and C.-Y. Zhang, “Comparison of structural and photoluminescence properties of ZnO thin films grown by pulsed laser deposition and ultrasonic spray pyrolysis,” *Thin Solid Films*, **2006**, 515, 1763.

[76] S. Christoulakis, M. Suchea, M. Katharakis, N. Katsarakis, E. Koudoumas, and G. Kiriakidis, “ZnO nanostructured transparent thin films by PLD,” *Rev. Adv. Mater. Sci.*, **2005**, 10, 331.

[77] H. Youl Bae, “Electrical and reducing gas sensing properties of ZnO and ZnO–CuO thin films fabricated by spin coating method,” *Sensors Actuators B Chem.*, **1999**, 55, 47.

[78] N. Jalali, P. Woolliams, M. Stewart, P. M. Weaver, M. G. Cain, S. Dunn, and J. Briscoe, “Improved performance of p-n junction-based ZnO nanogenerators through CuSCN-passivation of ZnO nanorods,” *J. Mater. Chem. A*, **2014**, 2, 10945.

[79] Y. Zhao, C. Li, M. Chen, X. Yu, Y. Chang, A. Chen, H. Zhu, and Z. Tang, “Growth of aligned ZnO nanowires via modified atmospheric pressure chemical vapor deposition,” *Phys. Lett. A*, **2016**, 380, 3993.

[80] S. Chen, R. M. Wilson, and R. Binions, “Synthesis of highly surface-textured ZnO thin films by aerosol assisted chemical vapour deposition,” *J. Mater. Chem. A*, **2015**, 3, 5794.

[81] S. Chen, N. Noor, I. P. Parkin, and R. Binions, “Temperature and thickness-dependent growth behaviour and opto-electronic properties of Ga-doped ZnO

films prepared by aerosol-assisted chemical vapour deposition," *J. Mater. Chem. A*, **2014**, 2, 17174.

[82] S. Chen, M. E. A. Warwick, and R. Binions, "Effects of film thickness and thermal treatment on the structural and opto-electronic properties of Ga-doped ZnO films deposited by sol-gel method," *Sol. Energy Mater. Sol. Cells*, **2015**, 137, 202.

[83] Y. Yang, C. Wang, H. Li, and Q. Lin, "Ultrahydrophobicity of ZnO modified CVD diamond films," *Appl. Surf. Sci.*, **2013**, 270, 260.

[84] A.-J. Cheng, Y. Tzeng, Y. Zhou, M. Park, T. Wu, C. Shannon, D. Wang, and W. Lee, "Thermal chemical vapor deposition growth of zinc oxide nanostructures for dye-sensitized solar cell fabrication," *Appl. Phys. Lett.*, **2008**, 92, 092113.

[85] S. Lautenschlaeger, S. Eisermann, B. K. Meyer, G. Callison, M. R. Wagner, and A. Hoffmann, "Nitrogen incorporation in homoepitaxial ZnO CVD epilayers," *Phys. status solidi - Rapid Res. Lett.*, **2009**, 3, 16.

[86] D.-S. Kang, H. S. Lee, S. K. Han, V. Srivastava, E. S. Babu, S.-K. Hong, M.-J. Kim, J.-H. Song, J.-H. Song, H. Kim, and D. Kim, "Growth and optical properties of ZnO nanorods prepared through hydrothermal growth followed by chemical vapor deposition," *J. Alloys Compd.*, **2011**, 509.

[87] Y. Zhao, C. Li, M. Chen, X. Yu, Y. Chang, A. Chen, H. Zhu, and Z. Tang, "Growth of aligned ZnO nanowires via modified atmospheric pressure chemical vapor deposition," *Phys. Lett. Sect. A Gen. At. Solid State Phys.*, **2016**, 380, 3993.

[88] H. Hayashi and Y. Hakuta, "Hydrothermal Synthesis of Metal Oxide Nanoparticles in Supercritical Water," *Materials (Basel).*, **2010**, 3, 3794.

[89] H. Hayashi and K. Torii, "Hydrothermal synthesis of titania photocatalyst under subcritical and supercritical water conditions," *J. Mater. Chem.*, **2002**, 12, 3671.

[90] H. Hayashi, Y. Hakuta, and Y. Kurata, "Hydrothermal synthesis of potassium niobate photocatalysts under subcritical and supercritical water conditions," *J. Mater. Chem.*, **2004**, 14, 2046.

[91] M. A. Vergés, A. Mifsud, and C. J. Serna, "Formation of rod-like zinc oxide microcrystals in homogeneous solutions," *J. Chem. Soc., Faraday Trans.*, **1990**, 86, 959.

[92] L. Vayssieres, "Growth of arrayed nanorods and nanowires of ZnO from aqueous solutions," *Adv. Mater.*, **2003**, 15, 464.

[93] J. A. Anta, E. Guillén, and R. Tena-Zaera, "ZnO-Based Dye-Sensitized Solar Cells," *J. Phys. Chem. C*, **2012**, 116, 11413.

[94] L. Vayssieres, K. Keis, A. Hagfeldt, and S.-E. Lindquist, "Three-Dimensional Array of Highly Oriented Crystalline ZnO Microtubes," *Chem. Mater.*, **2001**, 13, 4395.

[95] S. Shoaee, J. Briscoe, J. R. Durrant, and S. Dunn, "Acoustic Enhancement of Polymer/ZnO Nanorod Photovoltaic Device Performance," *Adv. Mater.*, **2014**, 26, 263.

[96] J. Briscoe, M. Stewart, M. Vopson, M. Cain, P. M. Weaver, and S. Dunn,

"Nanostructured p-n junctions for kinetic-to-electrical energy conversion," *Adv. Energy Mater.*, **2012**, 2, 1261.

[97] Y. Tak and K. Yong, "Controlled Growth of Well-Aligned ZnO Nanorod Array Using a Novel Solution Method," *J. Phys. Chem. B*, **2005**, 109, 19263.

[98] S. Xu, C. Lao, B. Weintraub, and Z. L. Wang, "Density-controlled growth of aligned ZnO nanowire arrays by seedles chemical approach on smooth surfaces," *J. Mater. Res.*, **2008**, 23, 2072.

[99] Y. Tak and K. Yong, "Controlled growth of well-aligned ZnO nanorod array using a novel solution method," *J. Phys. Chem. B*, **2005**, 109, 19263.

[100] Y. Zhang, M. K. Ram, E. K. Stefanakos, and D. Y. Goswami, "Synthesis, characterization, and applications of ZnO nanowires," *J. Nanomater.*, **2012**, 2012.

[101] G. Neri, A. Bonavita, G. Micali, G. Rizzo, S. Galvagno, M. Niederberger, and N. Pinna, "A highly sensitive oxygen sensor operating at room temperature based on platinum-doped In_2O_3 nanocrystals," *Chem. Commun.*, **2005**, 6032.

[102] A. Janotti and C. G. Van de Walle, "Native point defects in ZnO," *Phys. Rev. B*, **2007**, 76, 165202.

[103] Z. Wang, J. Xue, D. Han, and F. Gu, "Controllable defect redistribution of ZnO nanopyramids with exposed {1011} facets for enhanced gas sensing performance," *ACS Appl. Mater. Interfaces*, **2015**, 7, 308.

[104] A. Zainelabdin, S. Zaman, G. Amin, O. Nur, and M. Willander, "Deposition of well-aligned ZnO nanorods at 50 °C on metal, semiconducting polymer, and copper oxides substrates and their structural and optical properties," *Cryst. Growth Des.*, **2010**, 10, 3250.

[105] Y. Dong, F. Tuomisto, B. G. Svensson, A. Y. Kuznetsov, and L. J. Brillson, "Vacancy defect and defect cluster energetics in ion-implanted ZnO," *Phys. Rev. B - Condens. Matter Mater. Phys.*, **2010**, 81.

[106] A. Janotti and C. G. Van De Walle, "Oxygen vacancies in ZnO," *Appl. Phys. Lett.*, **2005**, 87, 1.

[107] A. Janotti and C. G. Van de Walle, "Fundamentals of zinc oxide as a semiconductor," *Reports Prog. Phys.*, **2009**, 72, 126501.

[108] M. D. McCluskey and S. J. Jokela, "Defects in ZnO," *J. Appl. Phys.*, **2009**, 106, 071101.

[109] S. E. Harrison, "Conductivity and Hall effect of ZnO at low temperatures," *Phys. Rev.*, **1954**, 93, 52.

[110] A. R. Hutson, "Hall effect studies of doped zinc Oxide single crystals," *Phys. Rev.*, **1957**, 108, 222.

[111] G. Palmer, "Electron paramagnetic resonance," *Methods Enzymol.*, **1967**, 10, 594.

[112] M. Che and E. Giamello, "Electron Paramagnetic Resonance," *Stud. Surf. Sci. Catal.*, **1990**, 57.

[113] C. Calle, R. a. Eichel, C. Finazzo, J. Forrer, J. Granwehr, I. Gromov, W. Groth, J. Harmer, M. Kälin, W. Lammler, L. Liesum, Z. Mádi, S. Stoll, S. Van

Doorslaer, and a. Schweiger, “Electron Paramagnetic Resonance Spectroscopy,” *Chim. Int. J. Chem.*, **2001**, 55, 763.

[114] C. Y. Zhu, C. C. Ling, G. Brauer, W. Anwand, and W. Skorupa, “Deep-level defects study of arsenic-implanted ZnO single crystal,” *Microelectronics J.*, **2009**, 40, 286.

[115] L. Vines, J. Wong-Leung, C. Jagadish, V. Quemener, E. V. Monakhov, and B. G. Svensson, “Acceptor-like deep level defects in ion-implanted ZnO,” *Appl. Phys. Lett.*, **2012**, 100.

[116] W. W. Lam, L. S. Yip, J. E. Greenspan, and I. Shih, “Deep level transient spectroscopy on ZnO/CdS/CuGaxIn1-xSe_2photovoltaic cells,” *Sol. Energy Mater. Sol. Cells*, **1998**, 50, 57.

[117] N. O. Korsunska, L. V. Borkovska, B. M. Bulakh, L. Y. Khomenkova, V. I. Kushnirenko, and I. V. Markevich, “The influence of defect drift in external electric field on green luminescence of ZnO single crystals,” in *Journal of Luminescence*, **2003**, 102–103, 733.

[118] L. N. Dem’yanets, L. E. Li, and T. G. Uvarova, “Hydrothermal synthesis and cathodoluminescence of ZnO crystalline powders and coatings,” *J. Cryst. Growth*, **2006**, 287, 23.

[119] K. Inoue, K. Fukuda, M. Fuji, S. Hashimoto, T. Hayakawa, S. Honda, M. Shoyama, and Y. Torii, “Fabrication and cathode luminescence of partially MgO-substituted ZnO powders,” *J. Ceram. Soc. Japan*, **2006**, 114.

[120] W. Anwand, G. Brauer, T. E. Cowan, D. Grambole, W. Skorupa, J. Čižek, J. Kuriplach, I. Procházka, W. Egger, and P. Sperr, “Structural characterization of H plasma-doped ZnO single crystals by positron annihilation spectroscopies,” *Phys. Status Solidi Appl. Mater. Sci.*, **2010**, 207, 2415.

[121] S. K. Sharma, P. K. Pujari, K. Sudarshan, D. Dutta, M. Mahapatra, S. V. Godbole, O. D. Jayakumar, and A. K. Tyagi, “Positron annihilation studies in ZnO nanoparticles,” *Solid State Commun.*, **2009**, 149, 550.

[122] Z. Y. Zhang, “Strain engineering for ZnO nanowires: First-principle calculations,” *Phys. Lett. Sect. A Gen. At. Solid State Phys.*, **2014**, 378, 1174.

[123] L. Shen, R. Q. Wu, H. Pan, G. W. Peng, M. Yang, Z. D. Sha, and Y. P. Feng, “Mechanism of ferromagnetism in nitrogen-doped ZnO: First-principle calculations,” *Phys. Rev. B - Condens. Matter Mater. Phys.*, **2008**, 78.

[124] T. Kamiya, K. Tajima, K. Nomura, H. Yanagi, and H. Hosono, “Interface electronic structures of zinc oxide and metals: First-principle study,” in *Physica Status Solidi (A) Applications and Materials Science*, **2008**, 205, 1929.

[125] H. G. Yu, “An optimal density functional theory method for GaN and ZnO,” *Chem. Phys. Lett.*, **2011**, 512, 231.

[126] B. Wang, S. Nagase, J. Zhao, and G. Wang, “The stability and electronic structure of single-walled ZnO nanotubes by density functional theory,” *Nanotechnology*, **2007**, 18.

[127] B. Wen and R. Melnik, “Relative stability of nanosized wurtzite and graphitic ZnO from density functional theory,” *Chem. Phys. Lett.*, **2008**, 466, 84.

[128] G. F. Fine, L. M. Cavanagh, A. Afonja, and R. Binions, “Metal Oxide Semi-

Conductor Gas Sensors in Environmental Monitoring," *Sensors*, **2010**, 10, 5469.

[129] Z. Yunusa, M. N. Hamidon, A. Kaiser, and Z. Awang, "Gas sensors: A review," *Sensors and Transducers*, **2014**, 168, 61.

[130] K. Arshak, E. Moore, G. M. Lyons, J. Harris, and S. Clifford, "A review of gas sensors employed in electronic nose applications," *Sensor Review*, 24. 181, 2004.

[131] B. Geng, C. Fang, F. Zhan, and N. Yu, "Gas Sensors," *Sens. Rev.*, **2008**, 14, 1337.

[132] M. Buehler and M. Ryan, "Gas sensor test chip," *Microelectron. Test Struct. 1996. ICMTS 1996. Proceedings. 1996 IEEE Int. Conf.*, **1996**, 9, 105.

[133] S. G. Sensors, "Solid state gas sensors," *Meas. Sci. Technol.*, **1997**, 8, 223.

[134] R. Kocache, "Gas Sensors," *Sens. Rev.*, **1994**, 14, 8.

[135] P. K. Clifford and D. T. Tuma, "Characteristics of semiconductor gas sensors I. Steady state gas response," *Sensors and Actuators*, **1982**, 3, 233.

[136] S. N. Malchenko, Y. N. Lychkovsky, and M. V. Baykov, "In2O3-based gas sensors," *Sensors Actuators B. Chem.*, **1993**, 13, 159.

[137] S. Park, S. Kim, G.-J. Sun, and C. Lee, "Synthesis, Structure, and Ethanol Gas Sensing Properties of In_2O_3 Nanorods Decorated with Bi_2O_3 Nanoparticles," *ACS Appl. Mater. Interfaces*, **2015**, 7, 8138.

[138] S. J. Kim, I. S. Hwang, Y. C. Kang, and J. H. Lee, "Design of selective gas sensors using additive-loaded In_2O_3 hollow spheres prepared by combinatorial hydrothermal reactions," *Sensors*, **2011**, 11, 10603.

[139] X. Chi, C. Liu, L. Liu, S. Li, H. Li, X. Zhang, X. Bo, and H. Shan, "Enhanced formaldehyde-sensing properties of mixed Fe_2O_3–In_2O_3 nanotubes," *Mater. Sci. Semicond. Process.*, **2014**, 18, 160.

[140] S. Park, S. Kim, G.-J. Sun, and C. Lee, "Synthesis, Structure, and Ethanol Gas Sensing Properties of In_2O_3 Nanorods Decorated with Bi_2O_3 Nanoparticles," *ACS Appl. Mater. Interfaces*, **2015**, 7, 8138.

[141] J. Wang, Z. Xie, Y. Si, X. Liu, X. Zhou, J. Yang, P. Hu, N. Han, J. Yang, and Y. Chen, "Ag-Modified In_2O_3 Nanoparticles for Highly Sensitive and Selective Ethanol Alarming," *Sensors*, **2017**, 17, 2220.

[142] S. J. Kim, I. S. Hwang, C. W. Na, I. D. Kim, Y. C. Kang, and J. H. Lee, "Ultrasensitive and selective C_2H_5OH sensors using Rh-loaded In_2O_3 hollow spheres," *J. Mater. Chem.*, **2011**, 21, 18560.

[143] C. Y. Lin, Y. Y. Fang, C. W. Lin, J. J. Tunney, and K. C. Ho, "Fabrication of NOx gas sensors using In_2O_3-ZnO composite films," *Sensors Actuators, B Chem.*, **2010**, 146, 28.

[144] Y. Matsuura and K. Takahata, "Stabilization of SnO_2 sintered gas sensors," *Sensors Actuators B. Chem.*, **1991**, 5, 205.

[145] N. Bârsan and R. Ionescu, "SnO_2-based gas sensors as chromatographic detectors," *Sensors Actuators B. Chem.*, **1994**, 19, 470.

[146] T. Wagner, C.-D. Kohl, M. Fröba, and M. Tiemann, "Gas sensing properties of

ordered mesoporous SnO_2," *Sensors*, **2006**, 6, 318.

[147] N. Bărsan, R. Ionescu, and A. Vancu, "Calibration curve for SnO_2-based gas sensors," *Sensors Actuators B. Chem.*, **1994**, 19, 466.

[148] V. Kumar, S. Sen, K. P. Muthe, N. K. Gaur, S. K. Gupta, and J. V. Yakhmi, "Copper doped SnO_2 nanowires as highly sensitive H_2S gas sensor," *Sensors Actuators B Chem.*, **2009**, 138, 587.

[149] H. Löw, G. Sulz, M. Lacher, G. Kühner, G. Uptmoor, H. Reiter, and K. Steiner, "Thin-film In-doped V-catalysed SnO_2 gas sensors," *Sensors Actuators B Chem.*, **1992**, 9, 215.

[150] Y. Liu, E. Koep, and M. Liu, "A Highly Sensitive and Fast-Responding SnO_2 Sensor Fabricated by Combustion Chemical Vapor Deposition," *Chem. Mater.*, **2005**, 17, 3997.

[151] L. Y. Yuan, T. Hyodo, Y. Shimizu, and M. Egashira, "Preparation of Mesoporous and Meso-macroporous SnO_2 Powders and Application to H_2 Gas Sensors," *Sensors Mater.*, **2009**, 21, 241.

[152] Y. I. Lee, K. J. Lee, D. H. Lee, Y. K. Jeong, H. S. Lee, and Y. H. Choa, "Preparation and gas sensitivity of SnO_2 nanopowder homogenously doped with Pt nanoparticles," *Curr. Appl. Phys.*, **2009**, 9, S79.

[153] T. Wagner, C.-D. Kohl, M. Fröba, M. Tiemann, G. S. Properties, and O. M. Sno, "Gas Sensing Properties of Ordered Mesoporous SnO_2," *Sensors*, **2006**, 6, 318.

[154] M. Ippommatsu, H. Sasaki, and H. Yanagida, "Sensing mechanism of SnO_2 gas sensors," *J. Mater. Sci.*, **1990**, 25, 259.

[155] S. Chaisitsak, "Nanocrystalline SnO_2: F thin films for liquid petroleum gas sensors," *Sensors*, **2011**, 11, 7127.

[156] H. Xia, Y. Wang, F. Kong, S. Wang, B. Zhu, X. Guo, J. Zhang, Y. Wang, S. Wu, M. Ivanovskaya, a Gurlo, P. Bogdanov, L. Chen, S. C. Tsang, J. Kukkola, J. Mäklin, N. Halonen, T. Kyllönen, G. Tóth, M. Szabó, A. Shchukarev, J. P. Mikkola, H. Jantunen, K. Kordás, W. Zhang, J. Dawody, M. Skoglundh, E. Fridell, E. Xue, K. Seshan, J. R. H. Ross, H. Tai, Y. Jiang, G. Xie, J. Yu, X. Chen, Z. Ying, H. T. Karkront, H. S. Rosenberg, R. B. Getman, W. F. Schneider, R. S. Physiological, G. K. Prasad, T. P. Radhakrishnan, D. S. Kumar, M. G. Krishna, and G. Laboratories, "Gas sensors based on anodic tungsten oxide," *Sensors Actuators, B Chem.*, **2008**, 11, 293.

[157] R. Ab Kadir, W. Zhang, Y. Wang, J. Z. Ou, W. Wlodarski, A. P. O'Mullane, G. Bryant, M. Taylor, and K. Kalantar-zadeh, "Anodized nanoporous WO_3 Schottky contact structures for hydrogen and ethanol sensing," *J. Mater. Chem. A*, **2015**, 3, 7994.

[158] A. Staerz, C. Berthold, T. Russ, S. Wicker, U. Weimar, and N. Barsan, "The oxidizing effect of humidity on WO_3 based sensors," *Sensors Actuators, B Chem.*, **2016**, 237, 54.

[159] A. A. Tomchenko, V. V. Khatko, and I. L. Emelianov, "WO_3 thick-film gas sensors," *Sensors Actuators B Chem.*, **1998**, 46, 8.

[160] D. Chen, L. Yin, L. Ge, B. Fan, R. Zhang, J. Sun, and G. Shao, "Low-

temperature and highly selective NO-sensing performance of WO_3 nanoplates decorated with silver nanoparticles," *Sensors Actuators, B Chem.*, **2013**, 185, 445.

[161] H. M. Lin, C. M. Hsu, H. Y. Yang, P. Y. Lee, and C. C. Yang, "Nanocrystalline WO_3-based H_2S sensors," *Sensors Actuators B. Chem.*, **1994**, 22, 63.

[162] X.-L. Li, T.-J. Lou, X.-M. Sun, and Y.-D. Li, "Highly Sensitive WO_3 Hollow-Sphere Gas Sensors," *Inorg. Chem.*, **2004**, 43, 5442.

[163] V. M. Arakelyan, M. S. Aleksanyan, R. V Hovhannisyan, G. E. Shahnazaryan, V. M. Aroutiounian, K. Hernadi, Z. Nemeth, and L. Forro, "Gas sensors made of multiwall carbon nanotubes modified by tin dioxide.," *J. Contemp. Phys. (Armenian Acad. Sci.*, **2013**, 48, 176.

[164] Y. Shen, T. Yamazaki, Z. Liu, D. Meng, T. Kikuta, and N. Nakatani, "Influence of effective surface area on gas sensing properties of WO_3 sputtered thin films," *Thin Solid Films*, **2009**, 517, 2069.

[165] H.-M. Lin, C.-H. Keng, and C.-Y. Tung, "Gas-sensing properties of nanocrystalline TiO_2," *Nanostructured Mater.*, **1997**, 9, 747.

[166] K. Zakrzewska, "Mixed oxides as gas sensors," in *Thin Solid Films*, 2001, 391, 229.

[167] X. Peng, Z. Wang, P. Huang, X. Chen, X. Fu, and W. Dai, "Comparative Study of Two Different TiO_2 Film Sensors on Response to H_2 under UV Light and Room Temperature," *Sensors*, **2016**, 16, 1249.

[168] O. Landau, A. Rothschild, and E. Zussman, "Electrospun nanostructured TiO_2 gas sensors," in *Proceedings of IEEE Sensors*, 2008, 863.

[169] O. Landau and A. Rothschild, "Fibrous TiO_2 gas sensors produced by electrospinning," *J. Electroceramics*, **2015**, 35, 148.

[170] Y. J. Choi, Z. Seeley, A. Bandyopadhyay, S. Bose, and S. A. Akbar, "Aluminum-doped TiO_2 nano-powders for gas sensors," *Sensors Actuators, B Chem.*, **2007**, 124, 111.

[171] H. Tang, K. Prasad, R. Sanjines, and F. Levy, "TiO_2 Anatase Thin-Films As Gas Sensors," *Sensors and Actuators B-Chemical*, 26. 71, 1995.

[172] K. S. Kim, W. H. Baek, J. M. Kim, T. S. Yoon, H. H. Lee, C. J. Kang, and Y. S. Kim, "A nanopore structured high performance toluene gas sensor made by nanoimprinting method," *Sensors*, **2010**, 10, 765.

[173] L. Zhu and W. Zeng, "Room-temperature gas sensing of ZnO-based gas sensor: A review," *Sensors Actuators A Phys.*, **2017**, 267, 242.

[174] M. W. G. Hoffmann, L. Mayrhofer Dr, O. Casals Dr, L. Caccamo, F. Hernez-Ramirez, G. Lilienkamp, W. Daum, M. Moseler, A. Waag, H. Shen, and J. D. Prades, "A highly selective and self-powered gas sensor via organic surface functionalization of p-Si/n-ZnO diodes," *Adv. Mater.*, **2014**, 26, 8017.

[175] Z. Wen, L. Zhu, Z. Zhang, and Z. Ye, "Fabrication of gas sensor based on mesoporous rhombus-shaped ZnO rod arrays," *Sensors Actuators, B Chem.*, **2015**, 208, 112.

[176] E. Modaresinezhad and S. Darbari, "Realization of a room-temperature/self-

powered humidity sensor, based on ZnO nanosheets," *Sensors Actuators B Chem.*, **2016**, 237, 358.

[177] P. W. (Peter W. Atkins, T. Overton, J. Rourke, M. Weller, and F. Armstrong, *Shriver & Atkins inorganic chemistry*, 4th editio. Oxford University Press, **2006**.

[178] Y. K. Chung, M. H. Kim, W. S. Um, H. S. Lee, J. K. Song, S. C. Choi, K. M. Yi, M. J. Lee, and K. W. Chung, "Gas sensing properties of WO3 thick film for NO2 gas dependent on process condition," *Sensors Actuators, B Chem.*, **1999**, 60, 49.

[179] J. Q. Wang and Z. A. Tang, "A CMOS-compatible temperature sensor based on the gaseous thermal conduction dependent on temperature," *Sensors Actuators, A Phys.*, **2012**, 176, 72.

[180] S. Vetter, S. Haffer, T. Wagner, and M. Tiemann, "Nanostructured Co_3O_4 as a CO gas sensor: Temperature-dependent behavior," *Sensors Actuators B Chem.*, **2015**, 206, 133.

[181] Y. Hiranaka, T. Abe, and H. Murata, "Gas-dependent response in the temperature transient of SnO_2 gas sensors," *Sensors Actuators B. Chem.*, **1992**, 9, 177.

[182] S. Park, M. Park, S. Kim, S.-G. Yi, M. Kim, J. Son, J. Cha, J. Hong, and K.-H. Yoo, "NO_2 gas sensor based on hydrogenated graphene," *Appl. Phys. Lett.*, **2017**, 111, 213102.

[183] S. Shukla and S. Seal, "Theoretical Model for Nanocrystallite Size Dependent Gas Sensitivity Enhancement in Nanocrystalline Tin Oxide Sensor," *Sens. Lett.*, **2004**, 2, 73.

[184] Y. Li, B. Zu, Y. Guo, K. Li, H. Zeng, and X. Dou, "Surface Superoxide Complex Defects-Boosted Ultrasensitive ppb-Level NO_2 Gas Sensors," *Small*, **2016**, 12, 1420.

[185] D. . Yoon and G. M. Choi, "Microstructure and Co gas sensing properties of porous ZnO producedby starch addition," *Sensors Actuators B*, **1997**, 45, 251.

[186] J. Tamaki, "High Sensitivity Semiconductor Gas Sensors," *Sens. Lett.*, **2005**, 3, 89.

[187] J. A. Dirksen, K. Duval, and T. A. Ring, "NiO thin-film formaldehyde gas sensor," *Sensors Actuators, B Chem.*, **2001**, 80, 106.

[188] M. Matsumiya, F. Qiu, W. Shin, N. Izu, N. Murayama, and S. Kanzaki, "Thin-film Li-doped NiO for thermoelectric hydrogen gas sensor," *Thin Solid Films*, **2002**, 419, 213.

[189] B. Alfeeli, G. Pickrell, and A. Wang, "Sub-nanoliter spectroscopic gas sensor," *Sensors*, **2006**, 6, 1308.

[190] R. Bogue, "Detecting gases with light: A review of optical gas sensor technologies," *Sens. Rev.*, **2015**, 35, 133.

[191] F. Tavoli and N. Alizadeh, "Optical ammonia gas sensor based on nanostructure dye-doped polypyrrole," *Sensors Actuators, B Chem.*, **2013**, 176, 761.

[192] C. Wagner, "The mechanism of the decomposition of nitrous oxide on zinc oxide as catalyst," *J. Chem. Phys.*, **1950**, 18, 69.

[193] J. Zhang, X. Liu, G. Neri, and N. Pinna, "Nanostructured Materials for Room-Temperature Gas Sensors," *Adv. Mater.*, **2016**, 28, 795.

[194] Y. Wang, Y. Wang, J. Cao, F. Kong, H. Xia, J. Zhang, B. Zhu, S. Wang, and S. Wu, "Low-temperature H_2S sensors based on Ag-doped α-Fe_2O_3 nanoparticles," *Sensors Actuators B Chem.*, **2008**, 131, 183.

[195] Y. Wang, X. Jiang, and Y. Xia, "A Solution-Phase, Precursor Route to Polycrystalline SnO_2 Nanowires That Can Be Used for Gas Sensing under Ambient Conditions," *J. Am. Chem. Soc.*, **2003**, 125, 16176.

[196] C. Jiang, G. Zhang, Y. Wu, L. Li, and K. Shi, "Facile synthesis of SnO_2 nanocrystalline tubes by electrospinning and their fast response and high sensitivity to NOx at room temperature," *CrystEngComm*, **2012**, 14, 2739.

[197] Y. M. Zhao and Y. Q. Zhu, "Room temperature ammonia sensing properties of $W_{18}O_{49}$ nanowires," *Sensors Actuators B Chem.*, **2009**, 137, 27.

[198] S. Vallejos, P. Umek, T. Stoycheva, F. Annanouch, E. Llobet, X. Correig, P. De Marco, C. Bittencourt, and C. Blackman, "Single-Step Deposition of Au- and Pt-Nanoparticle-Functionalized Tungsten Oxide Nanoneedles Synthesized Via Aerosol-Assisted CVD, and Used for Fabrication of Selective Gas Microsensor Arrays," *Adv. Funct. Mater.*, **2013**, 23, 1313.

[199] L. Xu, B. Dong, Y. Wang, X. Bai, Q. Liu, and H. Song, "Electrospinning preparation and room temperature gas sensing properties of porous In_2O_3 nanotubes and nanowires," *Sensors Actuators, B Chem.*, **2010**, 147, 531.

[200] H. Y. Lai and C. H. Chen, "Highly sensitive room-temperature CO gas sensors: Pt and Pd nanoparticle-decorated In_2O_3 flower-like nanobundles," *J. Mater. Chem.*, **2012**, 22, 13204.

[201] F. Gu, R. Nie, D. Han, and Z. Wang, "In_2O_3–graphene nanocomposite based gas sensor for selective detection of NO_2 at room temperature," *Sensors Actuators B Chem.*, **2015**, 219, 94.

[202] N. Du, H. Zhang, B. D. Chen, X. Y. Ma, Z. Liu, J. B. Wu, and D. R. Yang, "Porous Indium Oxide Nanotubes: Layer-by-Layer Assembly on Carbon-Nanotube Templates and Application for Room-Temperature NH_3 Gas Sensors," *Adv. Mater.*, **2007**, 19, 1641.

[203] P. Manjula, S. Arunkumar, and S. V Manorama, "Au/SnO2 an excellent material for room temperature carbon monoxide sensing," *Sensors Actuators B Chem.*, **2011**, 152, 168.

[204] J. Zhang, X. Liu, S. Wu, M. Xu, X. Guo, and S. Wang, "Au nanoparticle-decorated porous SnO_2 hollow spheres: a new model for a chemical sensor," *J. Mater. Chem.*, **2010**, 20, 6453.

[205] L. Chen and S. C. Tsang, "Ag doped WO_3-based powder sensor for the detection of NO gas in air," *Sensors Actuators B Chem.*, **2003**, 89, 68.

[206] D. Chen, L. Yin, L. Ge, B. Fan, R. Zhang, J. Sun, and G. Shao, "Low-temperature and highly selective NO-sensing performance of WO_3 nanoplates decorated with silver nanoparticles," *Sensors Actuators B Chem.*, **2013**, 185, 445.

[207] J. Fu, C. Zhao, J. Zhang, Y. Peng, and E. Xie, "Enhanced Gas Sensing

Performance of Electrospun Pt-Functionalized NiO Nanotubes with Chemical and Electronic Sensitization," *ACS Appl. Mater. Interfaces*, **2013**, 5, 7410.

[208] S. Shao, X. Qiu, D. He, R. Koehn, N. Guan, X. Lu, N. Bao, and C. A. Grimes, "Low temperature crystallization of transparent, highly ordered nanoporous SnO_2 thin films: application to room-temperature hydrogen sensing," *Nanoscale*, **2011**, 3, 4283.

[209] K. Wang, T. Zhao, G. Lian, Q. Yu, C. Luan, Q. Wang, and D. Cui, "Room temperature CO sensor fabricated from Pt-loaded SnO_2 porous nanosolid," *Sensors Actuators B Chem.*, **2013**, 184, 33.

[210] Z. Wang, Z. Li, T. Jiang, X. Xu, and C. Wang, "Ultrasensitive Hydrogen Sensor Based on Pd-Loaded SnO_2 Electrospun Nanofibers at Room Temperature," *ACS Appl. Mater. Interfaces*, **2013**, 5, 2013.

[211] B. Liu, D. Cai, Y. Liu, H. Li, C. Weng, G. Zeng, Q. Li, and T. Wang, "High-performance room-temperature hydrogen sensors based on combined effects of Pd decoration and Schottky barriers," *Nanoscale*, **2013**, 5, 2505.

[212] S.-W. Choi, A. Katoch, G.-J. Sun, and S. S. Kim, "Bimetallic Pd/Pt nanoparticle-functionalized SnO_2 nanowires for fast response and recovery to NO_2," *Sensors Actuators B Chem.*, **2013**, 181, 446.

[213] Y. Wang, B. Liu, D. Cai, H. Li, Y. Liu, D. Wang, L. Wang, Q. Li, and T. Wang, "Room-temperature hydrogen sensor based on grain-boundary controlled Pt decorated In_2O_3 nanocubes," *Sensors Actuators B Chem.*, **2014**, 201, 351.

[214] H.-Y. Lai and C.-H. Chen, "Highly sensitive room-temperature CO gas sensors: Pt and Pd nanoparticle-decorated In_2O_3 flower-like nanobundles," *J. Mater. Chem.*, **2012**, 22, 13204.

[215] N. S. Ramgir, P. K. Sharma, N. Datta, M. Kaur, A. K. Debnath, D. K. Aswal, and S. K. Gupta, "Room temperature H_2S sensor based on Au modified ZnO nanowires," *Sensors Actuators B Chem.*, **2013**, 186, 718.

[216] D. G. Hafeman, J. W. Parce, and H. M. Mcconnell, "Light-Addressable Potentiometric," *Science*, **1988**, 240, 1182.

[217] T. Yoshinobu, H. Iwasaki, Y. Ui, K. Furuichi, Y. Ermolenko, Y. Mourzina, T. Wagner, N. Näther, and M. J. Schöning, "The light-addressable potentiometric sensor for multi-ion sensing and imaging," *Methods*, **2005**, 37. 94.

[218] A. Das, A. Das, L. Be, C. Chao, S. Lai, R. Ming, L. Fu, C. Chu, Y. Heng, L. Lee, C. Ming, and J. Jeng, "GaN Thin Film Based Light Addressable Potentiometric Sensor for pH Sensing Application," *Appl. Phys. Express*, **2013**, 036601, 1.

[219] Y. Zhou, S. Jiang, S. Krause, and J.-N. Chazalviel, "Biosensor Arrays Based on the Degradation of Thin Polymer Films Interrogated by Scanning Photoinduced Impedance Microscopy," *Anal. Chem.*, **2007**, 79, 8974.

[220] S. Krause, W. Moritz, H. Talabani, M. Xu, A. Sabot, and G. Ensell, "Scanning Photo-Induced Impedance Microscopy—Resolution studies and polymer characterization," *Electrochim. Acta*, **2006**, 51, 1423.

[221] J. Wang, I. Campos, F. Wu, J. Zhu, G. B. Sukhorukov, M. Palma, M. Watkinson, and S. Krause, "The effect of gold nanoparticles on the impedance of

microcapsules visualized by scanning photo-induced impedance microscopy," *Electrochim. Acta*, **2016**, 208, 39.

[222] Y. Guo, K.-I. Miyamoto, T. Wagner, M. J. Schöning, and T. Yoshinobu, "Device simulation of the light-addressable potentiometric sensor for the investigation of the spatial resolution," *Sensors Actuators B. Chem.*, **2014**, 204, 659.

[223] T. Yoshinobu, K. Miyamoto, T. Wagner, and M. J. Schöning, "Recent developments of chemical imaging sensor systems based on the principle of the light-addressable potentiometric sensor," *Sensors Actuators B Chem.*, **2015**, 207, 926.

[224] J. Wang, F. Wu, M. Watkinson, J. Zhu, and S. Krause, "'click' Patterning of Self-Assembled Monolayers on Hydrogen-Terminated Silicon Surfaces and Their Characterization Using Light-Addressable Potentiometric Sensors," *Langmuir*, **2015**, 31, 9646.

[225] L. Chen, Y. Zhou, S. Jiang, J. Kunze, P. Schmuki, and S. Krause, "High resolution LAPS and SPIM," *Electrochem. commun.*, **2010**, 12, 758.

[226] W. Moritz, I. Gerhardt, D. Roden, M. Xu, and S. Krause, "Photocurrent measurements for laterally resolved interface characterization," *Fresenius J. Anal. Chem.*, **2000**, 367, 329.

[227] D.-W. Zhang, F. Wu, and S. Krause, "LAPS and SPIM Imaging Using ITO-Coated Glass as the Substrate Material," *Anal. Chem.*, **2017**, 89, 8129.

[228] D.-W. Zhang, N. Papaioannou, N. M. David, H. Luo, H. Gao, L. C. Tanase, T. Degousée, P. Samorì, A. Sapelkin, O. Fenwick, M.-M. Titirici, and S. Krause, "Photoelectrochemical response of carbon dots (CDs) derived from chitosan and their use in electrochemical imaging," *Mater. Horizons*, **2018**, 5, 423.

[229] C. M. Yang, T. W. Chiang, Y. T. Yeh, A. Das, Y. T. Lin, and T. C. Chen, "Sensing and pH-imaging properties of niobium oxide prepared by rapid thermal annealing for electrolyte-insulator-semiconductor structure and light-addressable potentiometric sensor," *Sensors Actuators, B Chem.*, **2015**, 207, 858.

[230] J. Suzurikawa, M. Nakao, Y. Jimbo, R. Kanzaki, and H. Takahashi, "A light addressable electrode with a TiO2 nanocrystalline film for localized electrical stimulation of cultured neurons," *Sensors Actuators, B Chem.*, **2014**, 192, 393.

[231] Q. Zhang, "Theoretical analysis and design of submicron-LAPS," *Sensors Actuators B Chem.*, **2005**, 105, 304.

[232] M. Saritas and H. D. McKell, "Comparison of minority-carrier diffusion length measurements in silicon by the photoconductive decay and surface photovoltage methods," *J. Appl. Phys.*, **1988**, 63, 4561.

[233] A. Etchebery, M. Etman, B. Fotouhi, J. Gautron, J.-L. Sculfort, and P. Lemasson, "Diffusion length of minority carrier in n -type semiconductors: A photoelectrochemical determination in aqueous solvents," *J. Appl. Phys.*, **1982**, 53, 8867.

[234] M. Nakao ', S. Inoue, T. Yoshinobu, and H. Iwasaki, "B High-resolution pH imaging sensor for microscopic observation of microorganisms," *ELSEVIER*

Sensors Actuators B, **1996**, 34, 234.

[235] Y. Ito, "High-spatial resolution LAPS," *Sensors Actuators B Chem.*, **1998**, 52, 107.

[236] A. Soudi, P. Dhakal, and Y. Gu, "Diameter dependence of the minority carrier diffusion length in individual ZnO nanowires," *Appl. Phys. Lett.*, **2010**, 96, 253115.

[237] K. T. Ramakrishna Reddy, P. A. Nwofe, and R. W. Miles, "Determination of the minority carrier diffusion length of SnS using electro-optical measurements," *Electron. Mater. Lett.*, **2013**, 9, 363.

[238] J. C. van den Heuvel, R. C. van Oort, and M. J. Geerts, "Diffusion length measurements of thin amorphous silicon layers," *Solid State Commun.*, **1989**, 69, 807.

[239] W. Moritz, T. Yoshinobu, F. Finger, S. Krause, M. Martin-Fernandez, and M. J. Schöning, "High resolution LAPS using amorphous silicon as the semiconductor material," *Sensors Actuators B Chem.*, **2004**, 103, 436.

[240] A. Soudi, P. Dhakal, and Y. Gu, "Diameter dependence of the minority carrier diffusion length in individual ZnO nanowires," *Appl. Phys. Lett.*, **2010**, 96, 253115.

[241] W. Yicong, W. Ping, Y. Xuesong, Z. Qingtao, L. Rong, Y. Weimin, and Z. Xiaoxiang, "A novel microphysiometer based on MLAPS for drugs screening," *Biosens. Bioelectron.*, **2001**, 16, 277.

[242] Y. Ermolenko, "The double K+/Ca2+ sensor based on laser scanned silicon transducer (LSST) for multi-component analysis," *Talanta*, **2003**, 59, 785.

[243] Y. E. Ermolenko, T. Yoshinobu, Y. G. Mourzina, Y. G. Vlasov, M. J. Schöning, and H. Iwasaki, "Laser-scanned silicon transducer (LSST) as a multisensor system," *Sensors Actuators B Chem.*, **2004**, 103, 457.

[244] A. Seki, K. Motoya, S. Watanabe, and I. Kubo, "Novel sensors for potassium, calcium and magnesium ions based on a silicon transducer as a light-addressable potentiometric sensor," *Anal. Chim. Acta*, **1999**, 382, 131.

[245] Y. Ermolenko, T. Yoshinobu, Y. Mourzina, S. Levichev, K. Furuichi, Y. Vlasov, M. J. Schöning, and H. Iwasaki, "Photocurable membranes for ion-selective light-addressable potentiometric sensor," *Sensors Actuators, B Chem.*, **2002**, 85, 79.

[246] J. C. Wang, Y. R. Ye, and Y. H. Lin, "Light-addressable potentiometric sensor with nitrogen-incorporated ceramic Sn_2O_3 membrane for chloride ions detection," *J. Am. Ceram. Soc.*, **2015**, 98, 443.

[247] Y. G. Mourzina, Y. E. Ermolenko, T. Yoshinobu, Y. Vlasov, H. Iwasaki, and M. J. Schöning, "Anion-selective light-addressable potentiometric sensors (LAPS) for the determination of nitrate and sulphate ions," *Sensors Actuators B Chem.*, **2003**, 91, 32.

[248] A. B. M. Ismail, K. Furuichi, T. Yoshinobu, and H. Iwasaki, "Light-addressable potentiometric fluoride (F−) sensor," *Sensors Actuators B Chem.*, **2002**, 86, 94.

[249] D.-W. Zhang, F. Wu, J. Wang, M. Watkinson, and S. Krause, "Image detection of yeast Saccharomyces cerevisiae by light-addressable potentiometric sensors

(LAPS)," *Electrochem. commun.*, **2016**, 72, 41.

[250] M. Adami, L. Piras, M. Lanzi, A. Fanigliulo, S. Vakula, and C. Nicoli, "Monitoring of enzymatic activity and quantitative measurements of substrates by means of a newly designed silicon-based potentiometric sensor," *Sensors Actuators B. Chem.*, **1994**, 18, 178.

[251] C. Ercole, M. Del Gallo, L. Mosiello, S. Baccella, and A. Lepidi, "Escherichia coli detection in vegetable food by a potentiometric biosensor," *Sensors Actuators, B Chem.*, **2003**, 91, 163.

[252] L. Bousse, G. Kirk, and G. Sigal, "Biosensors for detection of enzymes immobilized in microvolume reaction chambers," *Sensors Actuators B. Chem.*, **1990**, 1, 555.

[253] E. G. Kondrat'eva, T. A. Osipova, V. I. Sklyar, and A. N. Reshetilov, "Biosensors based on a light-addressable potentiometric sensor (LAPS) for analysis in both aquenous solutions and organic solvents," in *Applied Biochemistry and Biotechnology - Part A Enzyme Engineering and Biotechnology*, **2000**, 88, 335.

[254] I. G. Mourzina, T. Yoshinobu, Y. E. Ermolenko, Y. G. Vlasov, M. J. Schöning, and H. Iwasaki, "Immobilization of urease and cholinesterase on the surface of semiconductor transducer for the development of light-addressable potentiometric sensors," *Microchim. Acta*, **2004**, 144, 41.

[255] A. Seki, S.-I. Ikeda, I. Kubo, and I. Karube, "Biosensors based on light-addressable potentiometric sensors for urea, penicillin and glucose," *Anal. Chim. Acta*, **1998**, 373, 9.

[256] T. Yoshinobu, H. Ecken, A. Poghossian, A. Simonis, H. Iwasaki, H. Lüth, and M. J. Schöning, "Constant-current-mode LAPS (CLAPS) for the detection of penicillin," in *Electroanalysis*, **2001**, 13, 733.

[257] S. W. Jang, H. Yuan, D. E. Kim, K. J. Kim, B. H. Kang, N. S. Eum, and S. W. Kang, "High sensitivity sensing membranes of high addressable potentiometric sensor for Bio material detection," in *World Congress on Medical Physics and Biomedical Engineering **2006***, 2007, 1349.

[258] T. Yoshinobu, H. Ecken, A. Poghossian, H. Lüth, H. Iwasaki, and M. J. Schöning, "Alternative sensor materials for light-addressable potentiometric sensors," in *Sensors and Actuators, B: Chemical*, **2001**, 76, 388.

[259] R. S. José, R. M. Maki, F. V. Paulovich, C. F. Werner, A. Poghossian, M. C. F. De Oliveira, V. Zucolotto, O. N. Oliveira, and M. J. Schöning, "Use of information visualization methods eliminating cross talk in multiple sensing units investigated for a light-addressable potentiometric sensor," *Anal. Chem.*, **2010**, 82, 61.

[260] J. R. Siqueira, C. F. Werner, M. Bäcker, A. Poghossian, V. Zucolotto, O. N. Oliveira, and M. J. Schoñing, "Layer-by-layer assembly of carbon nanotubes incorporated in light-addressable potentiometric sensors," *J. Phys. Chem. C*, **2009**, 113, 14765.

[261] S. W. Jang, S. Y. Lee, J. H. Park, and J. H. Kim, "Light Addressable Potentiometric Sensor (LAPS) - Type Penicillin Sensor with Self-Assembled Monolayers and Its Image Detection," *Sensors Mater.*, **2006**, 18, 17.

[262] J. C. Fernando, K. R. Rogers, N. A. Anis, J. J. Valdes, R. G. Thompson, A. T. Eldefrawi, and M. E. Eldefrawi, "Rapid Detection of Anticholinesterase Insecticides by a Reusable Light Addressable Potentiometric Biosensor," *J. Agric. Food Chem.*, **1993**, 41, 511.

[263] K. R. Rogers, M. Eldefrawi, M. Foley, S. Alter, and P. Koga, "Light Addressable Potentiometric Biosensor For The Detection Of Anticholinesterases," *Anal. Lett.*, **1991**, 24, 191.

[264] J. Wang, X. Li, Y. Xia, S. Komarneni, H. Chen, J. Xu, L. Xiang, and D. Xie, "Hierarchical ZnO Nanosheet-Nanorod Architectures for Fabrication of Poly(3-hexylthiophene)/ZnO Hybrid NO 2 Sensor," *ACS Appl. Mater. Interfaces*, **2016**, 8, 8600.

[265] N. Jalali, P. Woolliams, M. Stewart, P. M. Weaver, M. G. Cain, S. Dunn, and J. Briscoe, "Improved performance of p–n junction-based ZnO nanogenerators through CuSCN-passivation of ZnO nanorods," *J. Mater. Chem. A*, **2014**, 2, 10945.

[266] S. M. Hatch, J. Briscoe, and S. Dunn, "Improved CuSCN-ZnO diode performance with spray deposited CuSCN," *Thin Solid Films*, **2013**, 531, 404.

[267] P. Lin, X. Yan, Z. Zhang, Y. Shen, Y. Zhao, Z. Bai, and Y. Zhang, "Self-Powered UV Photosensor Based on PEDOT:PSS/ZnO Micro/Nanowire with Strain-Modulated Photoresponse," *ACS Appl. Mater. Interfaces*, **2013**, 5, 3671.

[268] S. M. Hatch, J. Briscoe, A. Sapelkin, W. P. Gillin, J. B. Gilchrist, M. P. Ryan, S. Heutz, and S. Dunn, "Influence of anneal atmosphere on ZnO-nanorod photoluminescent and morphological properties with self-powered photodetector performance," *J. Appl. Phys.*, **2013**, 113, 204501.

[269] M. Law, L. E. Greene, J. C. Johnson, R. Saykally, and P. Yang, "Nanowire dye-sensitized solar cells," *Nat. Mater.*, **2005**, 4, 455.

[270] J. B. Coulter and D. P. Birnie, "Assessing Tauc Plot Slope Quantification: ZnO Thin Films as a Model System," *Phys. status solidi*, **2018**, 255, 1700393.

[271] L. E. Greene, M. Law, J. Goldberger, F. Kim, J. C. Johnson, Y. Zhang, R. J. Saykally, and P. Yang, "Low-temperature wafer-scale production of ZnO nanowire arrays," *Angew. Chemie - Int. Ed.*, **2003**, 42, 3031.

[272] S. M. Hatch, J. Briscoe, A. Sapelkin, W. P. Gillin, J. B. Gilchrist, M. P. Ryan, S. Heutz, and S. Dunn, "Influence of anneal atmosphere on ZnO-nanorod photoluminescent and morphological properties with self-powered photodetector performance," *J. Appl. Phys.*, **2013**, 113, 204501.

[273] J. Briscoe, N. Jalali, P. Woolliams, M. Stewart, P. M. Weaver, M. Cain, and S. Dunn, "Measurement techniques for piezoelectric nanogenerators," *Energy Environ. Sci.*, **2013**, 6, 3035.

[274] M. C. K. Sellers and E. G. Seebauer, "Measurement method for carrier concentration in TiO2via the Mott-Schottky approach," *Thin Solid Films*, **2011**, 519, 2103.

[275] A. Kolmakov, Y. Zhang, G. Cheng, and M. Moskovits, "Detection of CO and O2 using tin oxide nanowire sensors," *Adv. Mater.*, **2003**, 15, 997.

[276] S. Niu, Y. Hu, X. Wen, Y. Zhou, F. Zhang, L. Lin, S. Wang, and Z. L. Wang,

"Enhanced performance of flexible ZnO nanowire based room-temperature oxygen sensors by piezotronic effect," *Adv. Mater.*, **2013**, 25, 3701.

[277] N. Barsan, D. Koziej, and U. Weimar, "Metal oxide-based gas sensor research: How to?," *Sensors Actuators, B Chem.*, **2007**, 121, 18.

[278] N. D. Chinh, N. D. Quang, H. Lee, T. Thi Hien, N. M. Hieu, D. Kim, C. Kim, and D. Kim, "NO gas sensing kinetics at room temperature under UV light irradiation of In2O3 nanostructures," *Sci. Rep.*, **2016**, 6, 35066.

[279] M. Sturaro, E. Della Gaspera, N. Michieli, C. Cantalini, S. M. Emamjomeh, M. Guglielmi, and A. Martucci, "Degenerately Doped Metal Oxide Nanocrystals as Plasmonic and Chemoresistive Gas Sensors," *ACS Appl. Mater. Interfaces*, **2016**, 8, 30440.

[280] S. Park, S. An, Y. Mun, and C. Lee, "UV-Enhanced NO $_2$ Gas Sensing Properties of SnO $_2$ -Core/ZnO-Shell Nanowires at Room Temperature," *ACS Appl. Mater. Interfaces*, **2013**, 5, 4285.

[281] X. Xue, Y. Fu, Q. Wang, L. Xing, and Y. Zhang, "Outputting Olfactory Bionic Electric Impulse by PANI/PTFE/PANI Sandwich Nanostructures and their Application as Flexible, Smelling Electronic Skin," *Adv. Funct. Mater.*, **2016**, 26, 3128.

[282] Q. Wan, Q. H. Li, Y. J. Chen, T. H. Wang, X. L. He, J. P. Li, and C. L. Lin, "Fabrication and ethanol sensing characteristics of ZnO nanowire gas sensors," *Appl. Phys. Lett.*, **2004**, 84, 3654.

[283] E. Comini and G. Sberveglieri, "Metal oxide nanowires as chemical sensors," *Mater. Today*, **2010**, 13, 36.

[284] Z. Jing and J. Zhan, "Fabrication and gas-sensing properties of porous ZnO nanoplates," *Adv. Mater.*, **2008**, 20, 4547.

[285] S. M. Sze, and Kwok K. Ng," Physics of semicondcutor devices", Wiley, third edition, **2007**.

[286] F. Yakuphanoglu and E. Basaran, "Electrical and Optical Properties of an Organic Semiconductor Based on Polyaniline Prepared by Emulsion Polymerization and Fabrication of Ag / Polyaniline / n-Si Schottky Diode," *J. Phys. Chem. B*, **2006**, 110, 16908.

[287] K. Sarpatwari, O. O. Awadelkarim, M. W. Allen, S. M. Durbin, and S. E. Mohney, "Extracting the Richardson constant: IrOx/n-ZnO Schottky diodes," *Appl. Phys. Lett.*, **2009**, 94, 242110.

[288] C. X. Xu, C. Yang, B. X. Gu, and S. J. Fang, "Nanostructured ZnO for biosensing applications," *Chinese Sci. Bull.*, **2013**, 58, 2563.

[289] R. Georgekutty, M. K. Seery, and S. C. Pillai, "A highly efficient Ag-ZnO photocatalyst: Synthesis, properties, and mechanism," *J. Phys. Chem. C*, **2008**, 112, 13563.

[290] H. Qin, W. Li, Y. Xia, and T. He, "Photocatalytic activity of heterostructures based on ZnO and N-doped ZnO," *ACS Appl. Mater. Interfaces*, **2011**, 3, 3152.

[291] A. Janotti and C. G. Van De Walle, "Native point defects in ZnO," *Phys. Rev. B - Condens. Matter Mater. Phys.*, **2007**, 76.

[292] M. J. Powell and C. J. Carmalt, “Aerosols: A Sustainable Route to Functional Materials,” *Chem. - A Eur. J.*, **2017**, 23, 15543.

[293] C. Sumner, A. Sabot, K. Turner, and S. Krause, “A transducer based on enzyme-induced degradation of thin polymer films monitored by surface plasmon resonance,” *Anal. Chem.*, **2000**, 72, 5225.

[294] K. Kotsis and V. Staemmler, “Ab initio calculations of the O1s XPS spectra of ZnO and Zn oxo compounds,” *Phys. Chem. Chem. Phys.*, **2006**, 8, 1490.

[295] Y. Shinozaki, Y. Kikkawa, S. Sato, T. Fukuoka, T. Watanabe, S. Yoshida, T. Nakajima-Kambe, and H. K. Kitamoto, “Enzymatic degradation of polyester films by a cutinase-like enzyme from Pseudozyma antarctica: Surface plasmon resonance and atomic force microscopy study,” *Appl. Microbiol. Biotechnol.*, **2013**, 97, 8591.

[296] A. Sabot and S. Krause, “Simultaneous Quartz Crystal Microbalance Impedance and Electrochemical Impedance Measurements. Investigation into the Degradation of Thin Polymer Films,” *Anal. Chem.*, **2002**, 74, 3304.

[297] M. Suchy, M. B. Linder, T. Tammelin, J. M. Campbell, T. Vuorinen, and E. Kontturi, “Quantitative assessment of the enzymatic degradation of amorphous cellulose by using a quartz crystal microbalance with dissipation monitoring,” *Langmuir*, **2011**, 27, 8819.

[298] A. Biela, M. Watkinson, U. C. Meier, D. Baker, G. Giovannoni, C. R. Becer, and S. Krause, “Disposable MMP-9 sensor based on the degradation of peptide cross-linked hydrogel films using electrochemical impedance spectroscopy,” *Biosens. Bioelectron.*, **2015**, 68, 660.

[299] J. R. Siqueira, R. M. Maki, F. V Paulovich, C. F. Werner, A. Poghossian, M. C. F. de Oliveira, V. Zucolotto, O. N. Oliveira, and M. J. Schöning, “Use of Information Visualization Methods Eliminating Cross Talk in Multiple Sensing Units Investigated for a Light-Addressable Potentiometric Sensor,” *Anal. Chem.*, **2010**, 82, 61.

[300] M. Keusgen, M. Jünger, I. Krest, and M. J. Schöning, “Biosensoric detection of the cysteine sulphoxide alliin,” *Sensors Actuators B Chem.*, **2003**, 95, 297.

[301] J. Lee, B. S. Kang, B. Hicks, T. F. Chancellor Jr., B. H. Chu, H.-T. Wang, B. G. Keselowsky, F. Ren, and T. P. Lele, “The control of cell adhesion and viability by zinc oxide nanorods,” *Biomaterials*, **2008**, 29, 3743.